UNIVERSITY OF CALIFORNIA, SAN DIEGO

Changes in the Hemodynamic Stresses Occurring During the Enlargement of Abdominal Aortic Aneurysms

A dissertation submitted in partial satisfaction of the requirements for the degree Doctor of Philosophy in Engineering Sciences (Mechanical Engineering)

by

Anne-Virginie Salsac

Committee in charge:

Professor Juan C. Lasheras, Chair
Professor Jean-Marc Chomaz, co-Chair
Professor Dominique Barthès Biesel
Professor Dave Benson
Professor Yuan-Cheng Fung
Professor Paul Linden
Doctor Steven Sparks

2005

The dissertation of Anne-Virginie Salsac is approved, and it is acceptable in quality and form for publication on microfilm:

_____

_____

_____

_____

_____

_____
Co-chair

_____
Chair

University of California, San Diego

2005

Table of Contents

LIST OF SYMBOLS

A	Activation field
a	Inner local radius
a_0	Inner radius of the parent vessel ($a_0 = d/2$)
d	Inner diameter of the parent vessel
D	Maximum inner diameter of the aneurysm
e	Eccentricity of the aneurysm bulge
f	Frequency of the flow waveform
F	Non-dimensionalized variable of α_n
G_n	Pressure Fourier coefficient
h	Distance of the blood cell to the wall
i	Complex number or grid position in the x-direction
j	Grid position in the y-direction
J_n	Bessel function of the first kind of order n
l	Maximum length traveled by the vortex ring inside the aneurysm
L	Aneurysm length
n	Order of the mode in the Fourier decomposition
$\vec{n}$	Normal unit vector
p	Pressure
P	New pressure such that $P^* = \varepsilon\, p^*$.
R	Non-dimensionalized local radius in aneurysm
Q	Flow rate
r	Space variable in the radial direction
Re	Reynolds number
St	Strouhal number

St_{syst}	Strouhal number calculated with the systolic time t_{syst}
t	Time variable
$\vec{t}$	Tangential unit vector
T	Period of the flow waveform
t_0	Time of release of a blood cell at the entrance of an aneurysm
t_1	Time a blood cell exits the aneurysm
U	Characteristic velocity
u	x-component of the velocity vector
u_r	r-component of the velocity vector
U_r	New radial velocity such that $u_r^* = \varepsilon U_r^*$
v	y-component of the velocity vector
x	Space variable in the perpendicular direction to the flow
y	Space variable in the direction of the flow
Y	New space variable in the y-direction such that $Y^* = \varepsilon y^*$

Greek symbols

α	Womersley number
α_n	Womersley number based on the n^{th} Fourier model
β	Asymmetry parameter
Δx	distance traveled by the cell in the x-direction between 2 time steps
Δy	distance traveled by the cell in the y-direction between 2 time steps
ε	Small parameter $\varepsilon = \Lambda / a_0$
Λ	Characteristic length along which the local radius a changes
μ	Dynamic viscosity
ν	Kinematic viscosity

ρ	Density
σ	Rate of deformation tensor for a Newtonian fluid
Σ	Relaxation time-scale of the shear stresses on cells
τ	Local total stress
$\tau_{1,2,3}$	3 eigenvalues of the rate of deformation tensor σ
$\tau_{mean,H}$	Mean total stress measured in the healthy parent vessel
ω	Pulsation of the flow
ω_z	z-component of the vorticity vector

Conventions

X^*	Non-dimensionalized form of X
X_p	Peak value of X
$\overline{X}$	Time-average of X
$\langle X \rangle$	Space-average of X
∇	Gradient

Frequently used acronyms

AAA	Abdominal aortic aneurysm
CAF	Cell activation factor
EC	Endothelial cells
GWSS	Gradient of wall shear stresses
ILT	Intraluminal thrombus
LDL	Low density lipoprotein
MRI	Magnetic resonance imaging

NWRT	Near wall residence time
OSI	Oscillatory shear index
PIV	Particle image velocimetry
WSS	Wall shear stresses
WSS_{mean}	Time-average of the wall shear stresses
WSS_{mag}	Magnitude of the wall shear stresses

LIST OF FIGURES

ACKNOWLEDGEMENTS

Chapter 3 is, in part, a reprint of the material as it appears in “Evolution of the wall shear stresses during the progressive enlargement of symmetric abdominal aortic aneurysms,” Salsac A. V., Sparks S. R., Chomaz J. M. & Lasheras J. C. submitted for publication in Journal of Fluid Mechanics. Chapter 4 contains material of the paper “Effects of the loss of symmetry on the wall shear stresses in abdominal aortic aneurysms,” Salsac A. V., Sparks S. R., Chomaz J. M. & Lasheras J. C., submitted for publication in the Journal of Fluid Mechanics. Chapter 5 is, in part, a reprint of the paper “Physiological relevance of the changes in hemodynamics for circulating blood cells in abdominal aortic aneurysms,” as it has been submitted for publication in Journal of Biomechanics. The dissertation author was the primary researcher and author in each of these publications and the co-authors listed in these publications directed and supervised the research.

When it comes to acknowledging all the people that counted for me over the years of my Ph.D., so many names come to my mind. I would have loved to leave a personal note to all of you, but I fear it would be too long. So, to keep it short (maybe too short...), I would like to express my gratitude and warmly thank

- Juan, for having given me the opportunity to conduct a Ph.D. and guided me so well along the way, while giving me a lot of autonomy. Thank you for introducing me to the field of Biomechanics and for opening my eyes to all the problems that can still be solved. Thank you also for letting me work in partnership with France.

- Jean-Marc, for having agreed to come onboard of this adventure that has been the joint Ph.D. between UCSD and the Ecole Polytechnique. Thank you for all the discussions we had and for all your help.

- Steve, for explaining me some of the secrets of the human body and for helping me conduct the experiments in joy and good humor.

And to all of you, my dearest friends, thank you for having made my Ph.D the most enriching time of my life.

Finally, I would like to dedicate this dissertation to my parents and to my sister, Marie-Delphine, to whom I owe everything...

VITA

February 19, 1977	Born, Strasbourg, France
2000	Diplôme d'Ingénieurs (Engineering Degree). Ecole Nationale Supérieure d'Hydraulique et de Mécanique de Grenoble (ENSHMG), Institut National Polytechnique de Grenoble (INPG), Grenoble, France
2001–2005	Research and Teaching Assistant. Department of Mechanical and Aerospace Engineering, University of California, San Diego
2001	Master of Science. University of California, San Diego
2002–2005	Joint-Ph.D. with the Laboratory of Hydrodynamics, Ecole Polytechnique, France.
2005	Ph.D. University of California, San Diego
2005	Lecturer, Laboratory class in Materials / Fracture Mechanics, Department of Mechanical and Aerospace Engineering, University of California, San Diego

HONORS AND AWARDS

2000–2001	Irwin and Joan Jacobs Fellowship. Jacobs School of Engineering. University of California, San Diego.
2002	Outstanding Teaching Assistant Award. Department of Mechanical and Aerospace Engineering, University of California, San Diego.
2002–2005	Ph.D. Fellowship. Centre National de la Recherche Scientifique (CNRS), France.
2004	Outstanding Teaching Assistant Award. Department of Mechanical and Aerospace Engineering, University of California, San Diego.
2005	Dissertation Fellowship. Department of Mechanical and Aerospace Engineering, University of California, San Diego.

PUBLICATIONS

Reviewed papers:

Salsac A. V., Sparks S. R. & Lasheras J. C. “Hemodynamic changes occurring during the progressive enlargement of abdominal aortic aneurysms.” *Ann. Vasc. Surg.* **18**, 14–21 (2004).

Salsac A. V., Sparks S. R., Chomaz J. M. & Lasheras J. C. “Evolution of the wall shear stresses during the progressive enlargement of symmetric abdominal aortic aneurysms.” *J. Fluid Mech.* (submitted) (2004).

Salsac A. V., Sparks S. R., Chomaz J. M. & Lasheras J. C. “Effects of the loss of symmetry on the wall shear stresses in abdominal aortic aneurysms.” *J. Fluid Mech.* (submitted) (2005).

Salsac A. V., Sparks S. R., Chomaz J. M. & Lasheras J. C. “Physiological relevance of the changes in hemodynamics for circulating blood cells in abdominal aortic aneurysms.” *J. Biomech.* (submitted) (2005).

Book chapter:

Salsac A.-V., Sparks S. R. & Lasheras J. C. “Changes in pressure and wall tension occurring during the enlargement of abdominal aortic aneurysms.” *Simplicity, Rigor and Relevance in Fluid Mechanics* (ed. Higuera F. J., Jiménez J. & Vega J. M.). CINME Barcelona (2004).

FIELDS OF STUDY

Major Field: Fluid Mechanics / Engineering

Studies in Fluid Mechanics

Professors Keiko Nomura, Kalyanasundaram Seshadri, Constantine Pozrikidis, Sutanu Sarkar, Larri Armi, Paul Linden, Stefan Llewellyn-Smith and Juan C. Lasheras

Studies in Biomechanics

Professors Andrew McCulloch, Geert W. Schmid-Schoenbein, Paul C. Johnson and Juan C. Lasheras. Doctor Steven R. Sparks

Studies in Environmental Fluid Dynamics

Professors Colm Caulfield and Jim Rottman

Studies in Compressible flows, Physics of Gases and Combustion

Professor Forman Williams

Studies in Numerical Methods

Professors Thomas Bewley and Constantine Pozrikidis

Studies in Methods in Applied Mechanics

Professors Stefan Llewellyn-Smith and Glenn Ierley

ABSTRACT OF THE DISSERTATION

Changes in the Hemodynamic Stresses Occurring During
the Enlargement of Abdominal Aortic Aneurysms

by

Anne-Virginie Salsac
Doctor of Philosophy in Engineering Sciences (Mechanical Engineering)
University of California, San Diego, 2005
Professor Juan C. Lasheras, Chair
Professor Jean-Marc Chomaz, co-Chair

This research seeks to improve the understanding of the mechanisms accounting for the growth of abdominal aortic aneurysms (AAA), by quantifying the role that mechanical stimuli play in the disease processes. In recent years, the development of vascular diseases has been associated with the formation of disturbed patterns of wall shear stresses (WSS) and gradients of wall shear stresses (GWSS). They have been shown to affect the wall structural integrity, primarily via the changes induced on the morphology and functions of the endothelial cells (EC) and circulating blood cells.

Particle Image Velocimetry measurements of the pulsatile blood flow have been performed in aneurysm models, while changing systematically their geometric parameters. The parametric study shows that the flow separates from the wall even at early stages of the disease (dilatation $\leq$ 50%). A large vortex ring forms in symmetric aneurysms, followed by internal shear layers. Two regions with distinct patterns of WSS have been identified: a region of flow detachment, with low oscillatory WSS, and a

downstream region of flow reattachment, where large negative WSS and sustained GWSS are produced as a result of the impact of the vortex ring.

The loss of symmetry in the models engenders a helical flow pattern due to the non-symmetric vortex shedding. The dominant vortex, whose strength increases with the asymmetry parameter, is shed from the most bulged wall (anterior). It results in the formation of a large recirculating region, where ECs are subjected to quasi-steady reversed WSS of low magnitude, while the posterior wall is exposed to quasi-healthy WSS. GWSS are generated at the necks and around the point of impact of the vortex.

Lagrangian tracking of blood cells inside the different models of aneurysms shows a dramatic increase in the cell residence time as the aneurysm grows. While recirculating, cells experience high shear stresses close to the walls and inside the shear layers, which may lead to cell activation. The vortical structure of the flow also convects the cells towards the wall, increasing the probability for cell deposition and ipso facto for the formation of an intraluminal thrombus.

RESUME DE LA THESE

Evolution des Contraintes Hémodynamiques lors de
la Croissance des Anévrismes Aortiques Abdominaux

par

Anne-Virginie Salsac
Doctor of Philosophy in Engineering Sciences (Mechanical Engineering)
University of California, San Diego, 2005
Professeur Juan C. Lasheras, Directeur de thèse
Professeur Jean-Marc Chomaz, co-Directeur de thèse

Cette étude a pour but d'améliorer la compréhension des mécanismes responsables de la croissance des anévrismes aortiques abdominaux (AAA) et plus particulièrement de quantifier les effets des stimuli mécaniques sur la maladie. Des études récentes ont associé la plupart des maladies cardiovasculaires à des changements des contraintes pariétales et de leurs gradients. Toute modification des contraintes hémodynamiques influe l'intégrité structurelle de la paroi, à cause des changements induits sur la morphologie et les fonctions des cellules endothéliales et des cellules sanguines en circulation.

Des mesures PIV (Particle Image Velocimetry) de l'écoulement pulsé ont été réalisées dans des modèles d'anévrismes, dont les paramètres géométriques ont été changés systématiquement. Les résultats de l'étude paramétrique montrent que l'écoulement décolle de la paroi même aux stades très précoces de la maladie (dilatation $\geq$ 30%). Un large anneau de vorticité est formé dans les modèles symétriques

d’anévrismes, suivi de couches de mélange. Deux régions distinctes peuvent être identifiées : une zone de décollement caractérisée par de faibles contraintes oscillantes, et une région distale de réattachement, où de larges contraintes pariétales négatives et des gradients entretenus apparaissent en réponse à l’impact de l’anneau tourbillonnaire sur la paroi.

La perte de symétrie des modèles engendre un écoulement hélicoïdal. Le tourbillon qui domine l’écoulement se détache de la paroi à la courbure maximale (paroi antérieure). Il conduit à la formation d’une zone de recirculation, où les cellules endothéliales sont soumises à des contraintes pariétales négatives et quasi-permanentes avec de très faibles amplitudes, alors que la paroi postérieure est exposée à des contraintes proches de celles d’une aorte saine. Des gradients de contraintes sont générés aux cous de l’anévrisme, ainsi qu’au point d’impact du tourbillon.

Un suivi Lagrangien de cellules sanguines à l’intérieur des différents modèles d’anévrisme montre que l’élargissement de l’anévrisme conduit à une augmentation du temps de résidence des cellules. Lors de leur recirculation, les cellules sont périodiquement soumises à de larges contraintes près de la paroi et dans les couches de mélange, ce qui peut conduire à l’activation des cellules. La structure tourbillonnaire de l’écoulement convecte les cellules vers la paroi, ce qui augmente la probabilité de dépôt des cellules sur la paroi et par conséquent de formation d’un thrombus endoluminal.

Chapter 1

General introduction

An aneurysm is a permanent abnormal bulging of a vessel. Although aneurysms can occur in any type of blood vessels, the great majority of them form in arteries, in only a few restricted localizations. Aneurysms commonly develop along the circle of Willis in the brain and in the abdominal and thoracic portions of the aorta. Intracranial aneurysms tend to be saccular in shape or “berry-like”, whereas abdominal (Figure 1.1) and thoracic ones are typically fusiform, many thoracic aneurysms being dissecting[1]. Such a difference in shape indicates that the pathogenesis is likely to be different for each type of aneurysms.

An abdominal aortic aneurysm (AAA) is a spindle-shaped dilatation of the infrarenal abdominal aorta that lies between the renal bifurcation and the iliac branches (Figure 1.2). About one fifth of large abdominal aneurysms are not limited to just the aorta, but have extended to one or both of the common iliac arteries (Armon *et al.* 1998). A localized aortic dilatation is clinically considered an aneurysm, when its maximal diameter is greater than 1.5 times the healthy diameter (Johnston *et al.* 1991).

[1] A dissecting aneurysm occurs when blood gets through a lengthwise tear between layers off the wall of an artery.

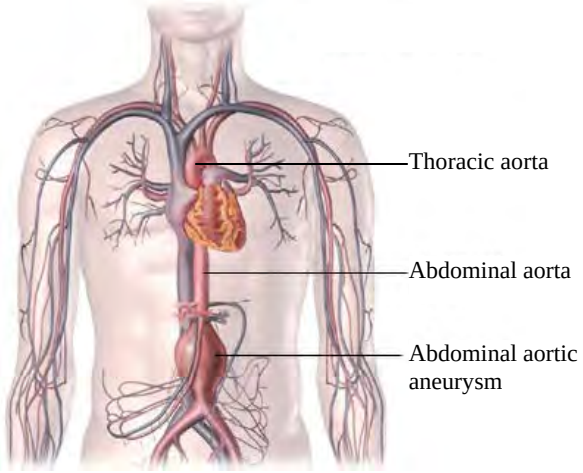

Figure 1.1: Abdominal aortic aneurysm

Aneurysms tend to grow asymptomatically, which explains why AAAs are rarely detected at early stages. Three out of four AAAs show no symptoms at the time they are diagnosed (Szilagyi 1982; Pokrovskii 2003). In some instances, large aneurysms may put pressure on vertebral bodies, causing lumbar pain (Sterpetti *et al.* 1988). The presence of a blood clot inside the AAA, also called endoluminal thrombus, may lead to emboli, when fractions of it break off and become lodged downstream in a smaller vessel. Otherwise, physicians must rely on non-invasive imaging techniques such as ultrasound, computed tomography (CT), or magnetic resonance imaging (MRI) to accurately determine the presence and extent of the aneurysmal disease (Figure 1.3).

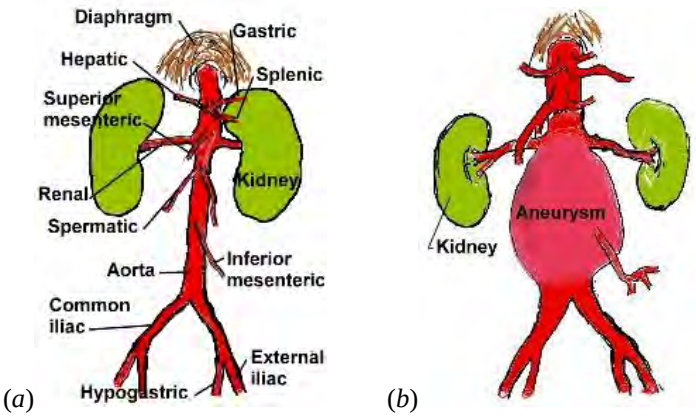

Figure 1.2: (*a*) Anatomy of the abdominal trunk, (*b*) Abdominal aortic aneurysm

Similarly to other vascular diseases, the rate of incidence of AAAs has increased over the last decades, which partly reflects the rise in the population life expectancy, but probably also the improvements made in diagnostic tools (Reilly & Tilson 1989; Best, Price & Fowkes 2003). It is estimated that 2-3% of the population over age 50 have an occult abdominal aortic aneurysm (Collin & Radcliffe 1988; Bonamigo & Siqueira 2003) and 200,000 new aneurysms are diagnosed each year in the United States. The incidence in males increases after age 55 with a peak in the seventh decade. In females, the incidence begins to rise at a later age (greater than age 70) with a continuous increase until the time of death (Bengtsson *et al.* 1996). The current male to female ratio for death from AAA has been reported to be as high as 11:1 between ages 60 an 64, and narrows to 3:1 between ages 85 and 90 (Collin & Radcliffe 1988).

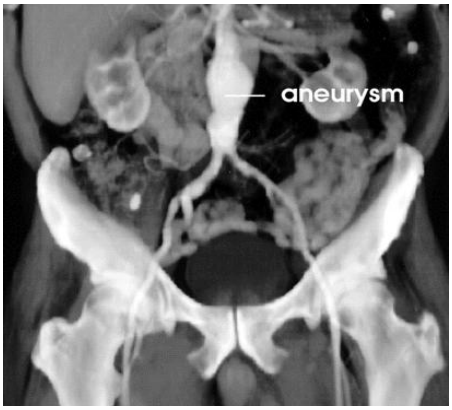

Figure 1.3: Spiral computed tomography (CT) with 3-D reconstruction showing an abdominal aneurysm originating below the renal arteries

Once formed, an aneurysm typically continues to enlarge progressively and at some point may rupture causing life-threatening bleeding. The overall mortality rate for ruptured AAA is 60-80%, which drops to 30-65% if the patient reaches a hospital alive (Ingoldby *et al.* 1986; Samy, Whyte & MacBain 1994; Basnyat *et al.* 1999; Singh *et al.* 2001). AAAs are responsible for 15,000 deaths annually in the United States, representing the 13th leading cause of death in the country (Reilly & Tilson 1989). But

misdiagnosed ruptured aneurysms are probably responsible for many additional cases of sudden death in older persons.

No accurate technique exists to date to either predict the aneurysmal expansion rate or its critical size or shape at the point of rupture. Treatment of AAA is decided on the basis of several factors, including size, expansion rates, natural history data and operative morbidity and mortality rates (Stringfellow, Lawrence & Stringfellow 1987; Hughes & Fontenelle 2000). It is widely recognized that increase in size leads to a higher risk of rupture (Law, Morris & Wald 1994; Englund *et al.* 1998). The average annual rupture rate of an aneurysm measuring < 4 cm is 0%, 1% when 4.5 cm, 11% when 5.5 cm and 26% when 6.5 cm (Green 2002). Although the likelihood for a small size aneurysm to rupture is very small, Darling (1970) proved that it can happen. Treatment is currently recommended for AAAs exceeding 5 cm in maximal diameter (Taylor & Porter 1985; Prisant & Mondy 2004) or having an enlargement rate greater than 0.5 cm in six months (Treska & Certik 1999), leaving the management of small AAAs (< 5 cm diameter) in an area of continuing controversy.

A. Changes in the wall composition involved in the formation, enlargement and rupture of AAAs

Except the capillaries, which are only one cell thick, all the vessel walls are composed of 3 layers (or “tunica”), the adventitia, the media and the intima (Figure 1.4). The thickness and proportion of components of each layer vary depending on the function of the vessel, arteries having thicker, more muscular and elastic walls than veins. In the case of arteries, (*i*) the adventitia, the outermost layer, is largely composed of ground matter, collagen bundles, some elastin fibers, autonomic nerves and small blood vessels (or “vasa vasorum”) that irrigate the adventitia. In the thoracic aorta, small branches of the vasa vasorum extend into the tunica media, but in the abdominal aorta,

the media only relies on diffusion processes to receive oxygen and nutrients from the lumen. (*ii*) The media is composed primarily of waves of smooth muscle cells (SMC) intermixed with elastin sheets, embedded in an extra-cellular matrix. It accounts for most of the strength and elasticity of the arterial wall and for the dynamic-recoil property of the wall. During systole, the elastic walls stretch to accommodate the volume of blood ejected from the heart, then recoil acting as a second subsidiary pump. (*iii*) The intima is composed of a lining mono-cell layer of multifunctional vascular endothelial cells (EC) that sits on a basal lamina and a very thin layer of connective tissue.

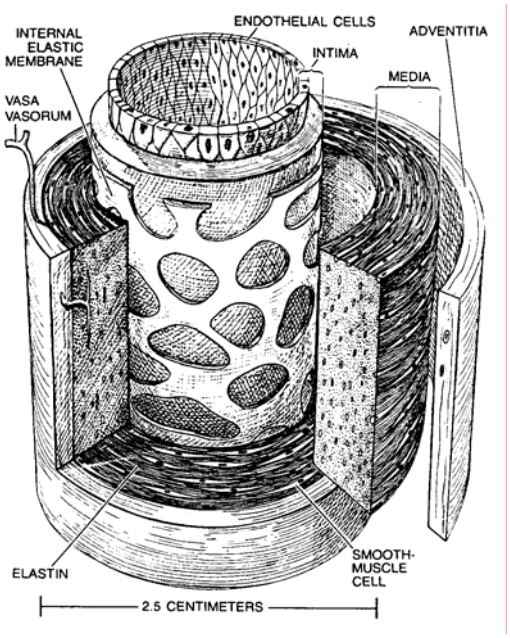

Figure 1.4: Wall composition of an arterial wall (Johansen 1982)

Smooth muscle cells and endothelial cells are the main cellular components of the arterial wall. The SMC play an important role in the development and maintenance of the arterial wall structure. They are the main source of collagen, elastin and other extra-cellular matrix components, such as proteoglycans, whose function includes regulation of cell adhesion, migration and proliferation. Endothelial cells at the interface between the blood flow and the wall act as a permeable barrier blocking the passage to large

molecules. They also detect and signal vascular injury and regulate the structure and function of the smooth muscle cells by producing vasoactive substances (NO, prostacyclin, etc.). The actuation of the contractile tone of the muscle cells is achieved by EC sensing the mechanical forces (pressure and shear stresses) acting on them, a process known as “mechanotransduction”.

Several factors may account for the much higher incidence of aneurysms in the abdominal aorta than in the thoracic segment (Best, Price & Fowkes 2003). The abdominal aorta is characterized by a smaller number of elastic lamellae in the medial layer than the thoracic aorta and therefore has a higher elastic modulus (Dobrin 1989; Nichols 1998 pp. 91-92). The pressure pulse is modified as it progresses along the aorta, as a result of the tapering of the aorta, stiffening of the aortic wall and presence of bifurcating branches, which leads to reflections of the pressure wave. Although the mean pressure decreases gradually, the pressure at peak systole largely increases as well as the temporal pressure gradient (McDonald 1974; Pedley 1979; MacSweeney 1993). The typically stiffer walls and higher systolic pressure of the infrarenal aorta may play a role in the pathogenesis of AAAs. Disruption of the elastin sheets has been thought to be the first step in the aneurysm formation. Aneurysm formation has been shown to occur after the sole induction of elastin failure in the tunicae media and adventitia (White & Mazzacco 1996).

AAAs develop primarily in older people and in an elastic artery that has undergone structural changes. With aging, a generalized process of increasing arterial stiffness results from the progressive replacement of elastin by collagen in the walls of large arteries (O’Rourke 1990). Arterial-related stiffening further leads to an increase in arterial pressure (Izzo & Shykoff 2001). Over time, the iliac bifurcation evolves in shape (Sun *et al.* 1994) and the lumen cross-section area of the common iliac arteries tends to decrease substantially (Hardy-Stashin, Meyer & Kauffman 1980; Greenwald, Carter &

Berry 1990). Besides, the iliac arteries are prone to atherosclerosis (Shah, Scarton & Tsapogas 1978; Pedersen, Yoganathan & Lefebvre 1992), which further decreases the size of the iliac lumen. This results in a higher systolic pressure in the infrarenal aorta, increasing the potential for AAA formation. These mechanisms could explain the relationship found by Matsushita *et al.* (2000) between aortic calcification and atherosclerotic disease in patients with AAAs.

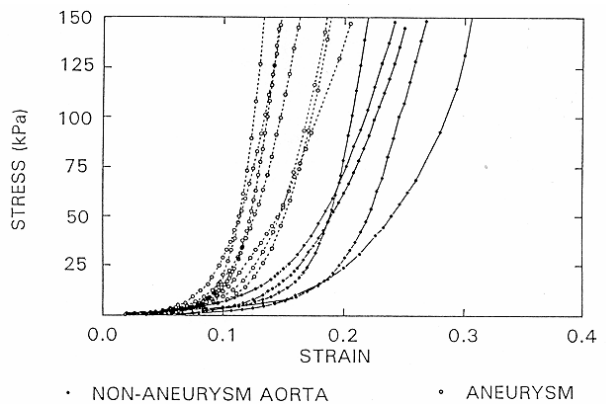

Figure 1.5: Elastic diagram of normal (dark circle) and aneurysmal (open circle) aortic walls. Shift of the curves corresponding to aneurysmal walls (He & Roach 1994).

Once the AAA is formed, it is characterized by profound changes in the aortic wall composition. Elastase activity and also collegenase later on in the disease process are increased within the aneurysm wall (Busuttil, Abou-Zamzam & Machkeder 1980; Busuttil *et al.* 1982; Carmo *et al.* 2002). The elastin-collagen ratio increases, further increasing the wall stiffness (Sumner, Hokanson & Strandness 1970; MacSweeney *et al.* 1992; He & Roach 1994; Thubrikar *et al.* 2001) – see Figure 1.5. The marked stiffness leads to little oscillatory deformations of the walls. The lack of stimulation on the smooth muscle cells results in a reduction in the synthesis of connective tissues in the media or even in the possible apoptosis of the cells (López-Candales *et al.* 1997; Thompson, Lias & Curci 1997; Liao *et al.* 2000). The depletion in matrix proteins is partially compensated by synthesis mechanisms that take place in the adventitia (Ghorpade &

Baxter 1996). The inflammatory response, indissociable of AAAs, is believed to play a key role in the structural degeneration of the elastic media. Inflammatory leukocytes infiltration into the wall and secrete proteolytic enzymes and effector molecules that destroy the matrix and affect its synthesis (Ghorpade & Baxter 1996).

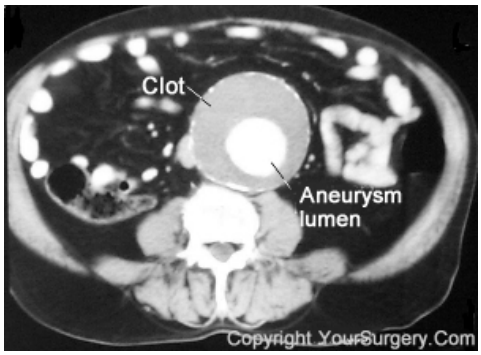

Figure 1.6: CT scan through an 8.5-cm AAA. The thrombus has filled most of the cavity, leaving a lumen with a diameter close to the size in a healthy vessel. (YourSurgery.com)

The endoluminal thrombus that lines the lumen of later-stage aneurysms may also play an important role in the enlargement of AAAs, although it is still undetermined (Figure 1.6). A mural thrombus develops in 75% of the aneurysms with a maximum diameter greater than 4.5 cm (Harter *et al.* 1982). The solid fibrin structure, in which platelets, blood cells, proteins and debris are imbedded, obstructs part of the lumen, restoring in most cases the original lumen diameter. Although no consensus has been reached on the ability of the thrombus to transmit pressure to the wall, all the studies agree that the thrombus reduces the wall stress by its ability to sustain tensile loads, adding structural support to the wall (Mower, Quinones & Gambhir 1997; Inzoli *et al.* 1993; Di Martino *et al.* 1998; Schurink *et al.* 2000; Mower & Quinones 2001; Thubrikar *et al.* 2003; Chaudhuri *et al.* 2004). Wang *et al.* (2001) have derived a two-parameter, large-strain, hyperelastic constitutive model, based on their uniaxial tensile testings. They have shown that the thrombus is made of three layers: the luminal layer, arranged in thick fibrin bundles, has the highest stiffness and strength. These fibers are respectively

partially and completely degenerated in the medial and abluminal layers. The thrombus is likely to act as a barrier to oxygen and nutrient diffusion to the intima and media layers (Vorp *et al.* 1998; Vorp *et al.* 2001), making the aneurysm wall prone to ischemia. Kazi *et al.* (2003) showed that the thrombus causes a marked reduction in wall thickness and more frequent signs of inflammation in the wall. Leukocytes that accumulate in the thrombus generate inflammatory enzymes (proteases) that further affect the wall structural integrity (Satta, Laara & Juvonen 1996; Adolf *et al.* 1997; Gacko & Głowiński 1998; Fontaine *et al.* 2002; Wang *et al.* 2002).

B. Pathogenesis of the abdominal aortic aneurysms

Although the pathogenesis of AAAs is thought to be multi-factorial and predominantly degenerative, the exact mechanisms responsible for the etiology of AAAs are not established. Several risk factors have, however, been shown to play a role in the formation of the disease. Some of the risk factors, such as age and gender (Singh *et al.* 2001; Bengtsson, Sonesson & Bergqvist 1996) or family history (Noorgard, Rais & Angquist 1984; Reilly & Tilson 1989; Salo *et al.* 1999) can be considered inevitable. We already discussed that AAAs are associated with aging processes and specificities to the male gender. The observed family occurrence of AAAs makes plausible the existence of a genetic link involved with the degeneration of the aortic wall and the development of AAAs, but no genetic factor has yet been discovered. Two rare hereditary disorders are known to promote the formation of aneurysms: Marfan's and Ehlers-Danlos' Syndromes (Wilmink *et al.* 2000). Marfan's Syndrome causes an abnormal breakdown of the elastic fibers in the aortic wall. Ehlers-Danlos syndrome is the name given to a group of inherited disorders that involve a genetic defect in collagen and connective tissue structure and synthesis. But these diseases tend to be rather associated with thoracic aneurysms than with AAAs.

Similarly to other cardiovascular diseases such as atherosclerosis, other predisposing risk factors are high blood pressure (Treska & Certik 1999; Pokrovskii *et al.* 2003), smoking (UK trial 2000) and high cholesterol (Singh *et al.* 2001). Hypertension affects all parts of the cardiovascular system. Local cells, such as endothelial cells and smooth muscle cells that sense the level of the hemodynamic forces (pressure and shear stresses) and transduce the signals into vasomotor responses are directly affected by the increase in blood pressure. Hypertension has been shown to distend the aorta (Paivansalo *et al.* 2000) and thicken the tunica media (Limas, Westrum & Limas 1980). As discussed in the previous section, the infrarenal aorta may be even more sensitive to hypertension than other vessels due to its higher inherent stiffness and the presence of the aortic bifurcation downstream of it. Cigarette smoking has been found to be the most important risk factor for the development (Reilly & Tilson 1986), expansion (MacSweeney *et al.* 1994) and rupture (UK trial 2000) of AAAs, aneurysms being 8 times more frequent in smokers than nonsmokers (Auerbach & Garfinkel 1980). Stefanadis *et al.* (1997 & 1998) showed that tobacco smoke leads to an active stiffening of the vessel due to its effect on the endothelial cells and sympathetic nerves resulting in an elevated muscular tone.

AAAs have long been thought to be secondary to atherosclerotic degeneration of the abdominal aorta. However, this view has been challenged over the past 2 decades (Johansen 1982). Atherosclerosis neither explains the high levels of elastase, collagenase and antiproteases nor the extent of the inflammatory processes, hallmarks of AAAs. It is now believed that atherosclerosis may promote aneurysm formation but does not have a causal effect (Lee *et al.* 1997), since only 25% of AAA patients present atherosclerosis (Zarins & Glagov 1982). Among other effects, atherosclerosis may weaken the infrarenal wall itself by reducing the medial thickness and the number of elastin sheets (Zarins, Xu & Glagov *et al.* 2001) and change the pressure waveform when affecting the iliac arteries (see previous section).

C. Influence of the hemodynamic forces on the pathology of AAAs

In recent years, understanding the etiology and progression of AAAs has become a multidisciplinary effort. The research on atherosclerosis has shown that the formation of regions of the vasculature presenting a complex morphology (such as bends, bifurcation, branches as well as sudden expansions and partial occlusions) and complex flow are the most important factors in the pathogenesis of the disease (Fox & Hugh 1966; Ku *et al.* 1985; Yoshida *et al.* 1987; Glagov *et al.* 1988; Lei, Kleinsteuer & Truskey 1995; Pedersen *et al.* 1997; Malek, Alper & Izumo 1999). Numerous investigations have reported the atherogenic effects of altered shear stresses on the vessel walls. This study is therefore based upon the postulate that changes in the hemodynamic forces play a crucial role in the formation and enlargement of AAAs, initiating biochemical events in the arterial wall that may account for the development of the vascular disease. Endothelial cells, smooth muscle cells and circulating cells (*e.g.* platelets) have all been proven to react to hemodynamic forces. Changes in the mechanical forces acting on the cells have the potential to modify their metabolism and function, which can in turn induce profound modifications of the wall composition and integrity.

1. Endothelial cells

ECs have been found to be highly responsive to wall shear stresses (WSS) (Davies *et al.* 1984). Shear stress, rather than pressure or wall tension is the mechanical stimulus that plays the major role (Traub & Berk 1998)[2]. Perturbations from the baseline stress conditions alter the mechanisms of mechanotransduction, changing the cell shape (Helmlinger *et al.* 1991), regulatory functions (Dewey *et al.* 1981; Noris *et al.* 1995) and

[2] It is essential to know that ECs primarily react to shear stresses rather than pressure variations, since the order of magnitude of the pressure variations ($\Delta p \sim 1/2\rho U^2 \sim 10^2$ N/m^2) is much greater than that of the shear stresses (WSS ~ 1 N/m^2).

gene expression of the ECs (Topper *et al.* 1996; Fisher *et al.* 2001; García-Cardeña[1] *et al.* 2001; Blackman, García-Cardeña & Gimbrone 2002; Tzima *et al.* 2002; Warabi *et al.* 2004). It has been shown that ECs not only sense WSS but can also differentiate among different types of stimuli (Helmlinger, Berk & Nerem 1995, García-Cardeña[2] *et al.* 2001). Almost all the studies, mentioned in this paragraph, have been conducted in vitro on endothelial cells cultured alone on a substrate. Therefore, these studies did not take into account the interaction with other types of cells.

In regions of low and oscillating stresses, loss and desquamation of endothelial cells have been observed (Walpola, Gotlieb & Langille 1993). The cells become randomly oriented in all directions, when they align parallel to the main flow direction in a healthy vessel (Levesque & Nerem 1985) (Figure 1.7). Their more rounded shape increases the inter-cellular space and ipso facto, the permeability of the membrane (Helmlinger *et al.* 1991). The absence or drastic reduction in WSS upregulate all the pathophysiologically relevant gene expressions of the endothelial cells. Low and oscillating shear stresses and static flow conditions have been shown to induce the endothelial gene expression of adhesion molecules (Chappell *et al.* 1998; Chiu *et al.* 2003), which, in turn, increases the leukocyte extravasation into the inflamed tissues. They increase the gene expression for platelet-derived growth factor (PDGF) (Kraiss *et al.* 1996), which acts as an important mitogen (*i.e.* induces mitosis) for smooth muscle cells leading to their proliferation and migration (Heldin & Westermark 1999). They also attenuate the EC gene expression of endothelial nitric oxide synthase (eNOS) (Chiu *et al.* 2003). One of the culprits in the pathogenesis of endothelial dysfunctions is the imbalance generated by low shear stress conditions between nitric oxide, a vasodilator, and angiotensin II, a vasoconstrictor. Indeed, nitric oxide is a growth inhibitor and is anti-inflammatory and anti-thrombotic, while angiotensin II is a growth promoter and is pro-inflammatory (Emerson *et al.* 1999).

High shear stresses, on the contrary, increase the nitric oxide release, which tends to lead to a structural expansion of the vessel (Ben Driss *et al.* 1997). This phenomenon may be viewed as an attempt to restore the WSS back to their healthy level (Kamiya & Togawa 1980; Zarins *et al.* 1987). In the regions of transition to turbulence, the turnover of the endothelial cells increases drastically (Davies *et al.* 1986), which does not occur in regions of laminar oscillating flow, although they are both characterized by multi-directional fluctuating patterns of shear stresses. The mechanisms initiating endothelial turnover in turbulent flow conditions remain therefore unexplained.

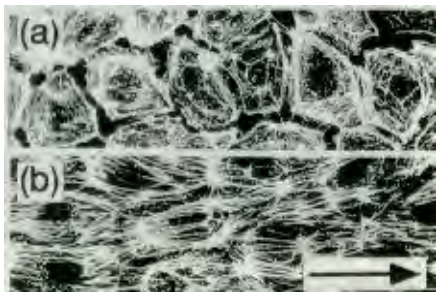

Figure 1.7: Morphology of endothelial cells (*a*) before and (*b*) after applying shear stress (M. Sato)

ECs are also sensitive to the spatial (Davies, Mundel & Barbee 1995) and temporal (Blackman, Thibault & Barbee 2000) gradients of wall shear stresses. High spatial gradient regions increase the division rate of the cells, which tend to migrate away from these regions by predominantly moving further downstream (DePaola *et al.* 1992). Cell loss is increased around the zone of high WSS gradients, which suggests that a cell proliferation-migration-loss cycle takes place in the vicinity of high gradient regions (Tardy *et al.* 1996). The endothelial cells expression has been shown to be modulated both by the magnitude of the spatial (Nagel *et al.* 1999) and temporal (Bao, Lu & Frangos 1999; Zhao *et al.* 2002) gradients of WSS. The latter also accelerate the remodeling (elongation/alignment) of the endothelial cells (Hsiai *et al.* 2002).

2. Smooth muscle cells

Mechanical stimuli, such as strain and fluid shear stress, influence the function of the smooth muscle cells. Mechanical strain influences the SMC functions, regulating the synthesis of extra-cellular matrix components (Lee *et al.* 2001). WSS modify the cell morphology and organization of the cytoskeleton (Sterpetti[1] *et al.* 1992; Cucina *et al.* 1996). Contrary to the endothelial cells that align with the applied WSS, vascular smooth muscle cells arrange in the direction perpendicular to them (Lee *et al.* 2002; Chiu *et al.* 2004). The existence of a physical link between ECs and SMCs has been demonstrated by Spagnoli *et al.* (1982), so it is plausible that the ECs and SMCs react symbiotically to shear stresses.

In the case of endothelial injury and denudation, SMCs are directly exposed to blood flow. Wang & Tarbell (1995) showed that, in a healthy patient, SMCs may also experience some level of WSS as a result of the transmural flow. Although the interstitial flow is very small, the WSS induced can be of the order of 0.1 to 0.3 N/m^2, which is still lower than the WSS experienced by the ECs. WSS modify the gene expression of the SMC (Papadaki[1] *et al.* 1998) and stimulate the release of platelet-derived growth factor (Sterpetti[2] *et al.* 1992), basic fibroblast growth factor (Rhoads, Eskin & McIntire 2000) and nitric oxide (Papadaki[2] *et al.* 1998; Gosgnach *et al.* 2000).

3. Circulating cells

Hemodynamic forces also have an important effect on the functions of platelets and leukocytes (neutrophils, monocytes and lymphocytes), which are the primary cells involved in the mechanism of thrombosis. Thrombosis is mainly triggered in the case of vascular injury, when the subendothelial or medial layers of blood vessels are in direct contact with the blood, exposing collagen (extrinsic pathway of blood coagulation). But it has long been known that the process of thrombosis depends on blood flow conditions

and convective mass transfer. High shear stresses, very low shear stresses (such as in areas of flow recirculation or stagnation) and large gradients of shear stresses affect the rate and localization of platelet activation/accumulation (Dintenfass 1964; Grabowski 1995). Activation refers to changes in the platelet functions triggered by chemical (thrombin, collagen, etc.) or mechanical stimuli (shear stresses). Upon activation, blood platelets undergo dramatic morphological and biochemical changes, resulting in shape change (extrusion of pseudopods), aggregation and granule secretion.

Most of the investigations on thrombus formation have concentrated on the effects of the lumen obstruction (stenosis) by an atherosclerotic plaque on platelet adhesion and aggregation (Mailhac *et al.* 1994; Tsao *et al.* 1995; Wootton *et al.* 2001; Einav & Bluestein 2004; Bluestein *et al.* 2004, etc). Hence, the vast majority of flow studies on endothelial cells comprise (very) high shear stress conditions. High shear alone has been shown to directly induce platelet activation and aggregation in the case of vessels with intact endothelial cells (Moake *et al.* 1986; O'Brien 1990; Kroll *et al.* 1996; Andrews *et al.* 2001; Shankaran, Alexandridis & Neelamegham 2003). These shear-induced platelet activation and aggregation involve plasma von Willebrand factor (vWF) as the ligand binding platelets to platelets (intrinsic pathway of blood clotting). Chemical stimuli, such as adenosine diphosphate (ADP) (Ikeda *et al.* 1991) and Ca^{2+} (Chow *et al.* 1992) are necessary for shear-activation to occur and they can modulate the effects of the mechanical forces. Shear stress-activation and aggregation are a function of both the shear stress magnitude and the duration that platelets are subjected to the shear stresses (Hellums & Hardwick 1981; Kunov, Steinman & Ethier 1996; Jesty *et al.* 2003). Zhang *et al.* (2003) have shown that platelets are aggregated in response to a 10 N/m^2 stress applied for periods about 10-20 s but minimally activated and rapid disaggregation follows the pulse of high shear (see also Wurzinger *et al.* 1985). Pulses longer than 20 s are required for irreversible aggregation. This suggests that, in vivo, high shear alone

may not be sufficient to induce platelet activation (Goldsmith 1974) or aggregation, even though shear-induced platelet aggregation has been found to be greater in response to pulsatile than steady stimulation (Sutera *et al.* 1988).

Platelets aggregate, however, after a high stress pulse (2.5 s), when exposed to low shear stresses immediately after (Zhang *et al.* 2002). In vivo, aggregation is therefore possible when platelets are entrained into recirculation regions with low secondary flows after high shear stress stimulation (Purvis & Giorgio 1991). Stagnation point flows are, for example, ideal candidates to promote platelet adhesion and subsequent aggregation even upon intact endothelial monolayers (Reininger, Korndorfer & Wurzinger 1998; Lee, Chiu & Jen 1999; David, Thomas & Walker 2001). The convection patterns promote aggregation by bringing platelets in contact with the endothelial surface (Karino & Goldsmith 1984). In the low shear regions, platelet aggregation is mediated by fibrinogen (Ikeda *et al.* 1993). Slow recirculation or stagnation regions induce long residence times and promote cell-cell collisions (Huang & Hellum 1993; Stroud, Berger & Saloner 2000). Platelet may recirculate in the separated region long enough to become activated and form small aggregates. Recirculating regions may also contain higher platelet-activating substances, promoting thrombus formation (Folie & McIntire 1989).

Platelet activation in regions of acute vascular injury is also regulated by the hemodynamic flow rate. The range of shear stress over which platelet adhesion and subsequent aggregation are observed is approximately 0.1 to 20 N/m^2 (Kroll *et al.* 1996). In low flow conditions, upregulated platelet activity results from increased exposure time to subendothelium collagen (Bassiouny *et al.* 1998). At high shear stresses (> 3 N/m^2), vWF acts as the ligand in the platelet thrombus production (Baumgartner, Turitto & Weiss 1980; Baumgartner, Tschopp & Meyer 1980).

Furthermore, recent evidence shows that circulating leukocytes respond not only to humoral inflammatory mediators but also to fluid shear stress (Rosenson-Schloss, Vitolo

& Moghe 1999; Eriksson *et al.* 2000; Marschel & Schmid-Schoenbein 2002). Shear stresses may activate leukocytes by increasing the actin polymerization and aggregation rate (Okuyama *et al.* 1996; Hernandez *et al.* 2001). Circulating leukocytes activate in regions of quasi flow stasis, projecting pseudopodia and increasing the probability of adherence to the vessel wall (Lawrence *et al.* 1997; Moazzam *et al.* 1997). But Moazzam *et al.* (1997) proved that, upon restoration of flow, the shear stresses induce the retraction of the pseudopodia. In response to inflammatory stimuli (e.g. activated endothelial cells (EC)), leukocytes roll along the endothelium and firmly attach before migrating into the vessel wall. The activation of platelets has been shown to greatly affect the interaction between leukocytes and EC. Platelet activation enhances the expression of some adhesion molecules and the gene expression in leukocytes and endothelial cells (Forlow, McEver & Nollert 2000; Fukuda *et al.* 2000; Nomura *et al.* 2001).

D. Hemodynamics in abdominal aortic aneurysms

Owing to their effect on the endothelial cells, smooth muscle cells and circulating cells, the patterns of shear stresses in AAAs appear to be one of the most physiologically relevant parameters to characterize in order to improve the current understanding of the pathogenesis of the disease.

Due to the complexity of measuring the flow inside an aneurysm, there has been no successful attempt at measuring the internal or wall shear stresses *in vivo* inside an abdominal aortic aneurysm. None of the current radiological imaging techniques (MRI, ultrasound, etc.) has a high enough spatial resolution to provide a reliable measurement of the velocity field, let alone of the shear stresses.

Consequently, over the last decade, a fairly large number of studies have been conducted using *in vitro* models to investigate the hemodynamics in AAAs. These studies have been performed in both symmetric and non-symmetric idealized-shape models of

AAA. Many of the studies involve steady flows (Schrader *et al.* 1992; Budwig *et al.* 1993; Peattie *et al.* 1994; Asbury *et al.* 1995; Bluestein *et al.* 1996; Peattie *et al.* 1996; etc.), which is not relevant to the problem at hand, since the flow is highly pulsatile in the aorta. Others (Yu 1999; Yu 2000; Yu & Zhao 2000) measured the velocity field in AAAs for unsteady flows, but used a sinusoidal waveform instead of a physiologically correct waveform, which strongly affects the characteristics of the flow. Finally, Taylor & Yamaguchi (1994) reproduced the flow waveform measured in the ascending aorta of the dog, which differs from the human aortic waveform.

Fukushima, Matsuzawa & Homma (1989) were the first to investigate the pulsatile nature of the flow, reproducing the physiologically correct velocity waveform. They studied experimentally the influence of the geometry of the bulge in three axisymmetric models of AAA, in the range of mean Reynolds numbers $289 \leq \langle \overline{Re} \rangle \leq 748$ and Womersley numbers $4.07 \leq \alpha \leq 10.6$. They showed that the flow remained attached to the walls during the acceleration (systole), but detached at the onset of the deceleration (beginning of diastole), generating a large primary vortex, followed by a weaker secondary vortex, and a recirculation zone dominated by very low velocities. Although this study showed qualitatively the most significant hemodynamic changes occurring as a result of the bulging, it did not provide any measurement of the most physiologically relevant parameters, i.e. the internal and wall shear stresses. As far as the WSS are concerned, a numerical simulation of the idealized laminar flow inside the AAA was realized and showed that, with the exception of the distal area, where the WSS peaked to a value of 1.5 Pa, the aneurysm wall was characterized by low WSS.

A similar qualitative study was conducted by Egelhoff *et al.* (1999) in four symmetric and one non-symmetric models of AAAs, but they did not perform measurements of the WSS either. Measuring the WSS experimentally is challenging, since it requires a precise measurement of the velocity at points very close to the wall, in order to assess the

velocity gradient at the wall. Yip & Yu (2001, 2002) published one set of Laser Doppler Anemometry measurements of WSS. However, they could not measure the spatial distribution of WSS, which is believed to be one of the most important factors leading to physiological changes.

A few groups performed numerical studies of the velocity field and WSS in AAAs. However, most numerical studies have concentrated on the calculation of the wall stresses and have not modeled the flow inside the aneurysm (Raghavan & Vorp 2000; Raghavan *et al.* 2001; Stringfellow, Lawrence & Stringfellow 1987; Thubrikar, al-Soudi & Robicsek 2001, etc.). Di Martino *et al.* (2001) have been the first one to conduct a fluid-structure interaction study. Numerical calculations have difficulty in predicting correctly the flow separation as well as the transition to turbulence, which are the two important characteristics of the aneurysmal flow. Some studies studied non-realistic flow waveform (reproduced non-realistic geometries, such as Viswanath, Rodkiewicz & Zajac (1997) who modeled extremely large AAAs (6 cm $\leq D \leq$ 14 cm) or Finol & Amon (2001), Finol & Amon[1] (2002) and Finol & Amon[2] (2002) who modeled a double aneurysm, made out of two consecutive expansions. Finol et al. (2003), however, completed a three-dimensional numerical simulation of the flow in a few AAA models increasing the asymmetry parameter. Although they showed the formation of detached regions and vortices in one of the non-symmetric models, they did not show their effect on the patterns of WSS, limiting their discussion to the peak systole, when the flow is still fully attached to the walls.

E. Objectives of the study

The above studies, both experimental and numerical, provide a good qualitative description of the flow in an AAA. However, no comprehensive quantitative study of the

evolution of the flow field as the AAA enlarges has been reported and, more importantly, there has been no accurate measurement of the changes in the mechanical stimuli on the endothelial cells and circulating blood cells during the growth of the aneurysm. The aim of this study is therefore to conduct precise measurements of the spatial and temporal changes in the wall shear stresses and internal shear stresses, which are respectively acting on the endothelial and circulating cells. The objective is to quantify their evolution during the progressive enlargement of AAAs.

In the following, we will discuss the results of a parametric study, in which the flow characteristics were studied inside the aneurysm, while varying systematically the geometric parameters of the models. Quantitative measurements of the velocity field inside the AAA models are obtained using Particle Image Velocimetry (PIV), while reproducing a physiologically correct pulsatile flow waveform. The hemodynamic stresses are calculated both internally and at the walls from the measured velocity field.

F. Structure of the dissertation

Chapter 2 presents the experimental setup and method for the in-vitro hemodynamic study. Measurements of the spatial and temporal changes of the wall shear stresses resulting from the aneurysm growth are discussed in Chapters 3 and 4. The measurements have been conducted respectively in symmetric and non-symmetric models of abdominal aortic aneurysms. In order to validate the experimental measurements of the WSS, an analytical model of the flow inside a vessel (healthy aorta or AAA), based on the well-known Womersley solution, is also presented in Chapter 3. Chapter 5 describes the changes in shear stresses acting on circulating blood cells, and Lagrangian changes in the shear stresses acting on them are analyzed as a function of the AAA geometry.

Chapter 2

Methods

A. Experimental apparatus

1. Aneurysm models

The hemodynamics inside an aneurysm depends on the flow characteristics (cardiac output, blood pressure, cardiac rate) and on the geometry of the bulge. In order to characterize the changes in the hemodynamic forces as the aneurysm enlarges, we have conducted a parametric study, in which we have varied the size and symmetry parameters of the aneurysmal dilatation. The experimental study is based on the use of *in vitro* aneurysm models, all fusiform in shape. The models consist of an expansion blown in a straight tube. The effect of the lumbar curvature has been not considered in the present study (Ku & Zhu 1997). This limitation will be further discussed at the end of Chapter 3.

Both symmetric and non-symmetric models have been considered. Incipient aneurysms tend to be symmetric in shape. But aneurysms with a maximum diameter greater than 4 cm typically expand non-symmetrically, because of the presence of the spinal column (Figure 2.1).

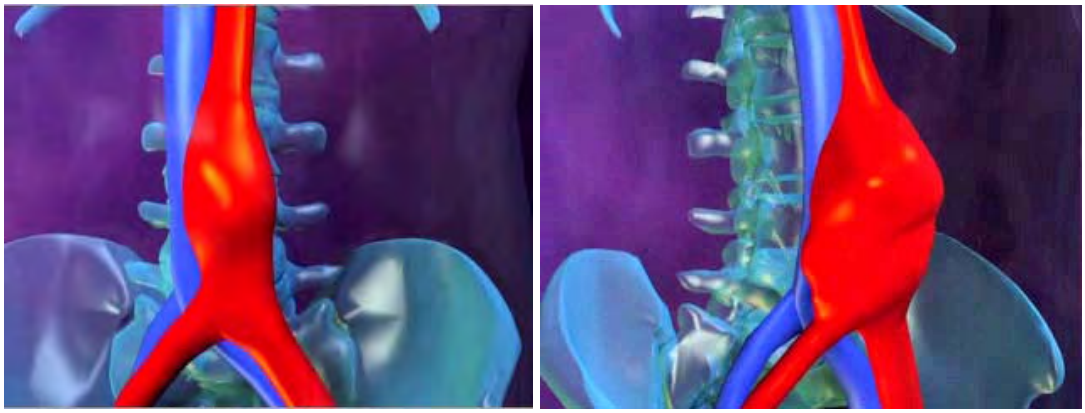

Figure 2.1: Sketches of a small (D < 4.5 cm) and later stage aneurysm

The geometry of the models can be characterized by three parameters: the dilatation ratio (D/d), the aspect ratio (L/d) and the asymmetry parameter $\beta = 2e/d$, where D and L are respectively the maximum internal diameter and the length of the aneurysm, d the internal diameter of the parent vessel and e the eccentricity (see Figure 2.2 for the symmetric models and Figure 2.3 for the non-symmetric ones). The eccentricity is defined as the distance between the axis of symmetry of the parent vessel and the centerline at the maximum bulge diameter. The asymmetry parameter β ranges from zero for a symmetric aneurysm to one for a non-symmetric model with a flat posterior wall.

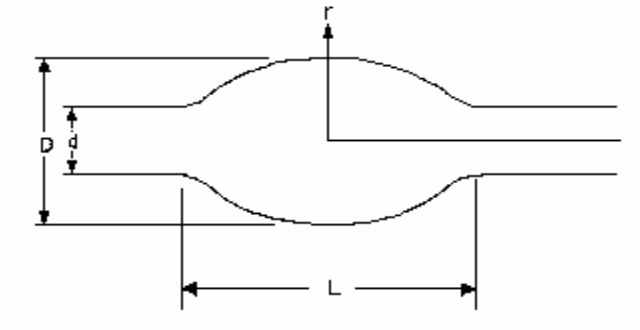

Figure 2.2: Geometry of a symmetric aneurysm model.

In the experiment, these three parameters have been systematically varied in order to study the effects of the aneurysm growth on the hemodynamic forces. Table 2.I summarizes the characteristics of the models considered in the study. The choice of an

idealized geometry for the models was made in order to control their shape with only three parameters. Although the models are not physiologically correct in shape, we hope that all the important physical processes can be observed and measured accurately. The models are supposed to be devoid of an endoluminal thrombus, since the largest diameter considered here is D = 4 cm, which is just below the critical size, above which an endoluminal thrombus has been clinically observed to develop (Harter *et al.* 1982).

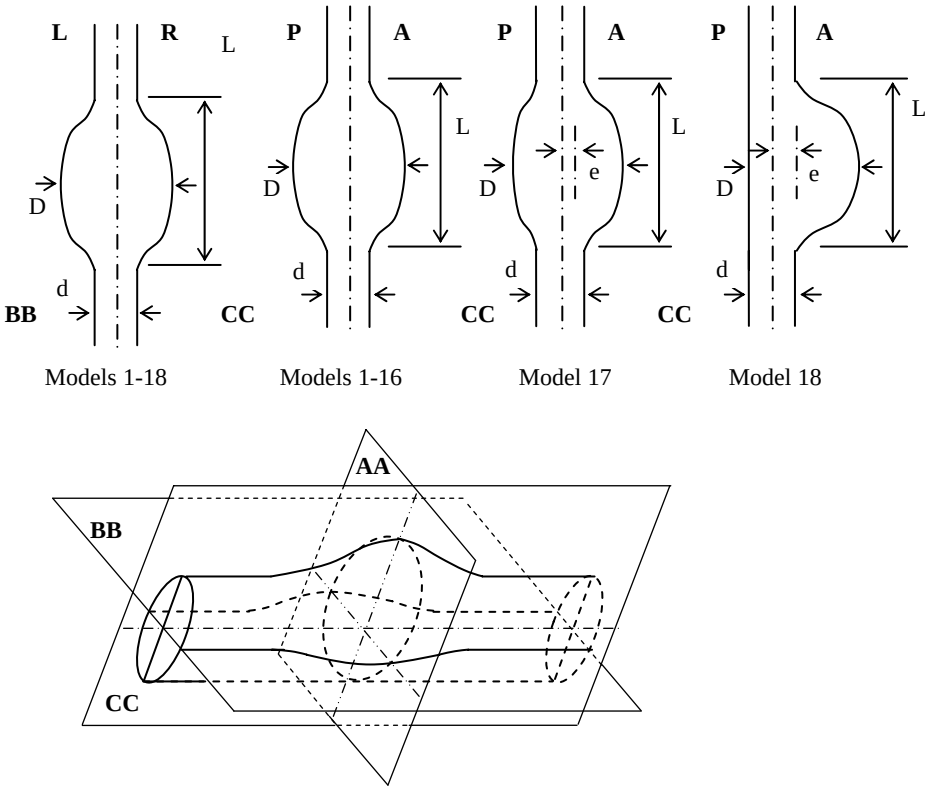

Figure 2.3: Geometry of the aneurysm models. L: left, R: right, P: posterior, A: anterior.

The models are made out of glass and are therefore rigid. AAAs have been shown to become much stiffer as they expand, because of the degradation of the elastin fibers in the walls (see Chapter 1). Calcification of the walls further increases the wall stiffness over time. Physiologically, the compliance of the arteries is crucial for the shaping of the flow waveform. However, in the experiment, the pump reproduces directly the flow

waveform measured in the infrarenal abdominal aorta. Therefore, the rigidity of the models does not affect the actual waveform inside the aneurysm.

		L/d		
	Models	2.9	3.9	5.2
D/d	1.3	*1*	*6*	*11*
	1.5	*2*	*7*	*12*
	1.7	*3*	*8*	*13*
	1.9	*4*	*9*	*14*
	2.1	*5*	*10*	*15*

Models	*D/d*	*L/d*	*β*
16	2.3	4.5	0
17	2.3	4.5	0.5
18	2.3	4.5	1

Table 2.I: Geometric parameters of the different models considered in the study. The first table indicates the values of the dilatation and aspect ratios for the 15 symmetric models considered in the first part of the study. The targeted aspect ratios were respectively 3, 4 and 5, but due to the inherent difficulty of the process of fabrication of the glass models, the ratios came out slightly different. The second table shows the 3 models considered in the study of the loss of symmetry. Larger dilatation and aspect ratios have been chosen, since the non-symmetry develops at later stages of the disease.

2. Experimental setup

Figure 2.4 schematically shows the experimental flow facility. The pulsatile flow is provided by a programmable piston pump (Sidac Engineering, Ontario, Canada). A micro-stepping motor (Compumotor Corporation, Cupertino, CA) controls the displacement of the piston on a rack inside a cylinder. The piston diameter is 6.3 cm and the cylinder contains a volume of 450 ml. Each time the piston reaches the end of the cylinder, a four-way spool valve (Numatics, Highlands, MI) reverses the inlet and outlet pathways, in order to always keep the flow in the same direction in the test section.

The programmable piston pump reproduces the abdominal aortic flow. The chosen waveform is based on the measurements by Maier *et al.* (1989), conducted in a healthy

male patient at rest (Figure 2.5). Similarly to the results by Long *et al.* (2000), it comprises a quite large reversal of the flow in the diastole, which has been shown to be the case in a healthy person at rest by Holenstein & Ku (1988). Retrograde flow at this point of the cycle is thought to provide blood flow to the coronary arteries (McDonald 1974; Caro *et al.* 1978). Other groups have, however, measured the abdominal aortic flow to have a very small reversal flow (Mills *et al.* 1970, Pedersen *et al.* 1993). For this study, we have elected the extreme case of a subsequent diastolic flow reversal. This choice should not affect greatly the key phenomena, which are the flow separation and the formation of a vortex. Flow separation is guaranteed to occur at the peak systole at the latest. Earlier flow separation will depend on the acceleration and on the geometric parameters of the model.

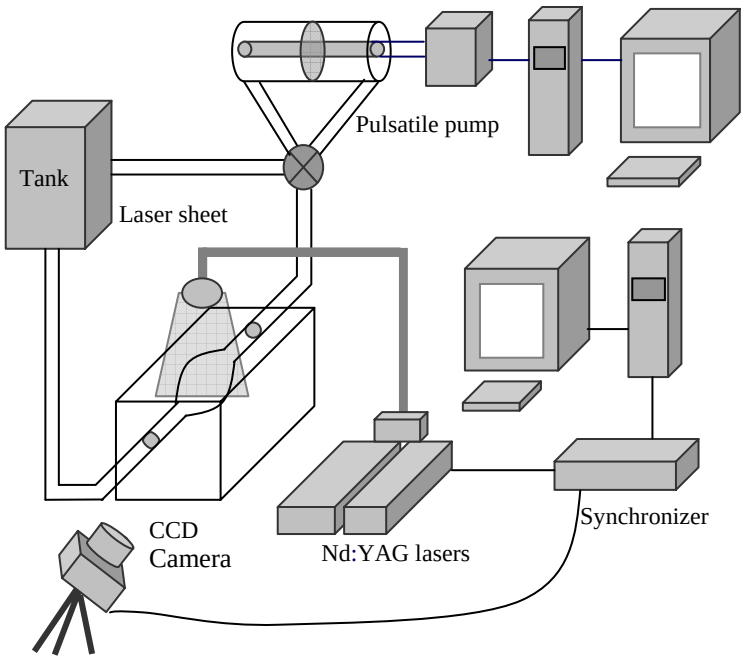

Figure 2.4: Experimental setup

By using water as the perfusion fluid, we neglected the non-Newtonian behavior of blood in the experiments. In the case of non-Newtonian fluids, the viscosity coefficient can still be assumed constant in the high shear stress regions, but it is a function of the stress in the regions of low shear stress. For large vessels, larger than 1 mm in diameter (Nichols 1998), the regions of low shear stresses are confined to the core of the fluid. Most of this study focuses on the quantification of the shear stresses at the wall, where they are the highest. The quantification of the shear stresses on individual blood cells may need a small correction factor for the few cells launched in the core of the aneurysm. Nevertheless, we will see that these cells either leave the aneurysm very quickly without noticing the presence of the aneurysm or they are entrained into the recirculating region, where they are again in closer contact with the wall. Assuming blood as Newtonian should therefore be a valid hypothesis.

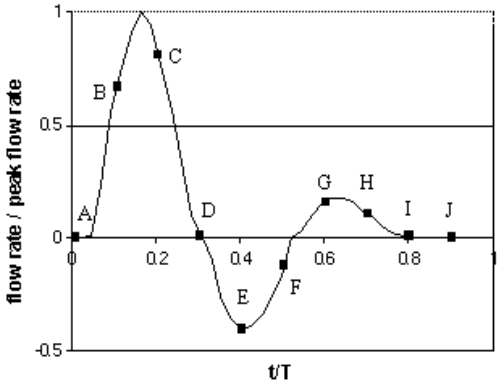

Figure 2.5: The waveform delivered by the pulsatile pump reproduces the typical infra-renal flow rate of a male patient at rest. The letters indicate the approximate times along the cardiac cycle when the measurements were made.

The use of pure water was dictated by the pump, which is not powerful enough to deliver the aortic sub-renal flow rate. The fluid viscosity was then reduced by a factor of 3.9, as compared to whole blood. In order to maintain a complete similarity, the aneurysm models were scaled down by a factor of 1.9 (d = 9 mm in the experiment). The goal was to keep both the Reynolds number, ratio of the convective inertial forces to the

viscous forces, and the Womersley number, ratio of the unsteady inertial forces to the viscous forces, identical to the physiological flow conditions. This complete similarity ensures that the Strouhal number remains constant as well, since it is proportional to $\alpha^2/\overline{Re}$, where $\alpha = d/2\sqrt{\omega/\nu}$, $\overline{Re} = \overline{U}d/\nu$, $\overline{U}$ being a characteristic cross-averaged velocity, ω the pulsation frequency of the flow and ν the fluid kinematic viscosity. More specifically, the flow conditions used in this study correspond to a peak Reynolds number of 2700, a mean Reynolds number of 330 and a Womersley number of 10.7. With a same peak Reynolds number, the mean Reynolds number would have been higher if we had chosen to use a flow waveform without flow reversal ($\langle \overline{Re} \rangle \sim 550$). The measured quantities (velocity, vorticity, stresses) presented in the next sections have been converted into the physiological values.

B. Particle Image Velocimetry

Particle Image Velocimetry (PIV) measurements of the instantaneous velocity field have been conducted in a cross-section of the AAA. The PIV system (TSI Incorporated, St Paul, MN) is composed of two 50 mJ pulsed Nd:YAG lasers, a synchronizer and a CCD camera (Figure 2.4). The lasers produce short duration (6 ns), high-energy (12 mJ) pulses of light in the green band (532 nm). The energy is produced from a flashlight that can be fired at variable frequencies up to 10 Hz. The use of two lasers allows us to control very precisely the time between two pulses. Any pulse separation can be achieved from very short to long, while maintaining the full power in each laser. The light beam is converted into a light sheet using consecutively a cylindrical and a spherical lens. The laser sheet is 1 mm thick at the focal point.

Optical access to the model is provided at two orthogonal locations, one for the laser sheet and the other for the CCD camera (630046 PIVCAM 10-30), which has a resolution of 1024×1024 pixels and a 8-bit dynamic range. The flow is seeded with 10 μm-diameter

lypocodium particles (Carolina Biological Supply Company, Burlington, NC), which are illuminated each time the lasers are fired. The AAA models are placed in a transparent box filled with water in order to limit optical deformations due to refractions. The light scattered by the tracer particles are recorded by the camera, which is synchronized with the lasers (TSI Laserpulse^{TM} synchronizer). The displacements of the particles are obtained by locally cross-correlating sequential images recorded by the camera. The cross-correlation function for an image pair is calculated using fast Fourier transforms. The interrogation window is 64×64 pixels in size and a 50% overlapping is employed in both directions. The resolution varies from one experiment to the next, depending on the total size of the measurement window. It ranges between 0.4 mm for the zoom measurements to 1.8 mm for the larger aneurysm models. The few incorrect vectors have then been removed by hand and replaced with an interpolated vector. No post-processing smoothing or averaging function has been used. The velocity vectors are computed knowing the time interval between two pulses of the lasers. Validation of the measured velocity field will be discussed in Chapter 3, when comparing the measurements in a healthy vessel with the Womersley solution.

Chapter 3

Evolution of the wall shear stresses during the progressive enlargement of symmetric Abdominal Aortic Aneurysms

A. Introduction

The prevailing view concerning the formation and growth of abdominal aortic aneurysms is based on the assumption that they result from a coupling between structural changes in the intimal and medial layers of the arterial wall and disturbed patterns of hemodynamic stresses acting on the vessel wall. Any structural or conformational wall change has an influence on the flow in the implicated arterial segment and downstream of it. Conversely, changes in the blood flow result in altered pressure and wall shear stresses (WSS) and may lead to wall inflammation, thrombus formation and breakdown of the wall integrity. Thus, once an aneurysm is formed, it is reasonable to assume that the expansion processes are not purely dependent on cellular and molecular processes, but rather on an interplay between mechanical stimuli exerted by the pulsatile blood flow and physiological wall changes. As detailed in the introduction, past investigators have shown that regions of high wall shear stresses, low and oscillating WSS and high

gradients of WSS may all contribute to the vascular disease, primarily via their effect on the endothelial cells.

All the flow studies have provided a good qualitative description of the flow in an AAA. However, no comprehensive quantitative study of the evolution of the flow field as the AAA enlarges has been reported and, more importantly, there has been no accurate measurements of the evolution of the WSS. The aim of chapters 3 and 4, therefore, is to conduct precise measurements of the spatial and temporal changes in the wall shear stresses acting on the endothelial cells as the AAA grows. In the following, we will discuss the results of a parametric study, in which the flow characteristics were studied inside symmetric aneurysms, while varying systematically the geometric parameters of the models. Aneurysms tend to be symmetric at the early stages of the disease ($D < 4$ cm), but they may become non-symmetric when they reach larger sizes. The effects of non-symmetry will be considered in the next chapter. Quantitative measurements of the velocity field inside the AAA models are obtained using Particle Image Velocimetry (PIV), while reproducing a physiologically correct pulsatile flow waveform. The hemodynamic stresses acting on the vessel wall are then calculated in each model from the measured velocity field. In order to validate our experimental measurements of the WSS, we analyze these measurements in the context of an analytical model of the flow inside a healthy aorta as well as in an AAA, which was developed based on the well-known Womersley solution.

Section C describes the flow in a healthy infrarenal aorta measured experimentally. The results are compared to the standard analytical results of a pulsatile flow in a straight infinitely long tube. Section D details the results of the parametric study performed in *in vitro* models of AAAs and of the analytical solution. A discussion about the physiological implications of the measured changes in the flow properties resulting from the AAA enlargement is given in section E.

B. Experimental setup

The experiments consist of a parametric study in symmetric models of AAA. The aspect and dilatation ratios have been systematically varied in order to analyze the changes in the hemodynamic forces as the aneurysm enlarges. The different parameters considered in this part of the study are indicated in the left-hand side table of Table 2.I.

The instantaneous velocity fields are measured inside the AAA under pulsatile flow conditions using the two-dimensional Particle Image Velocimetry system described in Chapter 2. In the case of transverse measurements, the use of a prism in contact with the free surface of the water contained in the box enabled us to avoid any problem resulting from the free surface distortion and changes in the index of refraction (see Schowalter, Van Atta & Lasheras (1994) for further information).

C. Characteristics of the flow in a healthy abdominal aorta

1. Measurements of the flow in a healthy abdominal aorta

Hemodynamics

Before discussing the flow characteristics in an aneurysmal aorta, we shall first characterize the flow in a healthy infrarenal aorta as the reference case. The infrarenal aorta is idealized as a straight pipe of diameter *d*. The model is supplied with the typical pulsatile inflow waveform measured in a male subject at rest. The mean flow rate is 1 liter/min and the simulated heart rate 71 pulses per minute. This input flow condition corresponds to a peak Reynolds number $\overline{Re}_p$ = 2700, a time-averaged Reynolds number $\langle \overline{Re} \rangle$ = 330 and a Womersley number α = 10.7, where the Reynolds numbers are calculated based on the flow rate. The input waveform of the flow rate, non-dimensionalized by the systolic peak, is plotted in Figure 3.1 (*a*).

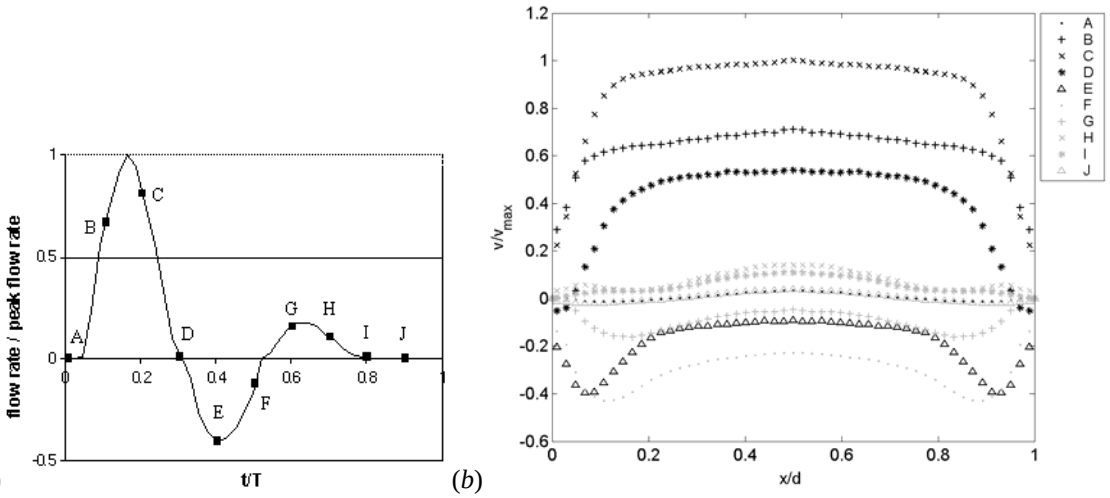

(*a*) (*b*)

Figure 3.1: (*a*) Flow waveform input in the pump, non-dimensionalized by the peak flow rate Q_p, (*b*) corresponding velocity profiles across the abdominal aorta, non-dimensionalized by the velocity based on Q_p, at different instants of time in one cardiac cycle. The *y*-axis is along the symmetry axis of the model and the *x*-axis is in the transverse direction.

The time evolution of the velocity field was measured in the central axial plane of the tube using the PIV system. The measurements were done zooming in on only half the vessel in order to achieve a high spatial resolution (mesh size $0.019d \times 0.019d$). Figure 3.1 (*b*) shows, at 10 representative instants of time in the cardiac cycle, the profiles of the longitudinal velocity, *v*, phase-averaged over 6 cardiac cycles. At the beginning of the cycle, the fluid is almost at rest (Figure 3.1 (*b*) A). During the acceleration portion of the systole (Figure 3.1 (*b*) B), the flow develops into the characteristic top-hat velocity profile. When the Womersley number is small, viscous forces dominate and the velocity profiles are parabolic in shape. However, for Womersley number above 10, which is the case in the abdominal aorta, the unsteady inertial forces dominate, and the flow is nearly top hat with thin boundary layers. At the peak systole, the thickness of the boundary layer scales as d/α. After the peak systole, the flow decelerates first along the walls and quickly reverses, while the bulk of the fluid still moves forward, with a blunt velocity profile (Figure 3.1 (*b*) D). The bulk of the flow reverses only at peak diastole (Figure 3.1 (*b*) E-F). At the end of the diastole, the flow sets forward again (Figure 3.1 (*b*) G-H) and over

the resting period (Figure 3.1 (*b*) I-J), the flow relaxes to near rest before being accelerated again at the beginning of the next cardiac cycle. It is important to point out that although the flow develops an inflexional velocity profile during diastole, it remains entirely laminar during the whole cardiac cycle. At the high values of Womersley number corresponding to these measurements, the characteristic time for the growth of the instability is much longer than the period of the pulsatility.

Wall shear stresses

The evolution of the wall shear stresses was calculated over time from the velocity measurements described above. In the case of a laminar, axisymmetric flow, the WSS is simply given by

$$WSS = -\mu \frac{\partial v}{\partial x}. \tag{3.1}$$

The wall shear stresses have been calculated using a linear interpolation between the velocity measurement the closest to the wall and the null velocity at the wall (see Appendix A for calculation of WSS). A linear interpolation was used in the vicinity to the wall, similarly to what is commonly used for turbulent boundary layers.

The measured temporal evolution of the wall shear stress, plotted in Figure 3.2, follows closely the evolution of the flow rate. The WSS ranges from -3 Pa to 4.9 Pa, the extrema occurring respectively at peak diastole and peak systole. The convention is to assign a negative value to WSS corresponding to reversed flow. As mentioned in Chapter 2, all the measured values correspond to the physiologically correct flow. The time-averaged WSS,

$$WSS_{mean} = \frac{1}{T}\int_0^T WSS\, dt, \tag{3.2}$$

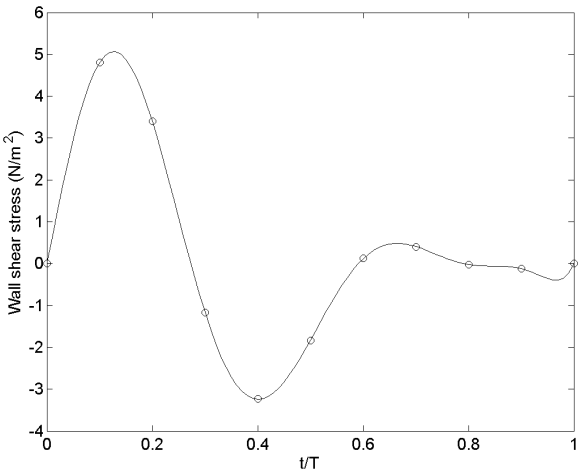

Figure 3.2: Wall shear stresses measured in a model of healthy infrarenal aorta.

is measured to be equal to 0.27 Pa, T being the period of the cardiac cycle. The time-average of the magnitude of the shear stress,

$$WSS_{mag} = \frac{1}{T}\int_0^T \left|WSS\right| \, dt, \tag{3.3}$$

is equal to 1.5 Pa. The oscillating shear index,

$$OSI = \frac{1}{2}\left(1 - \frac{WSS_{mean}}{WSS_{mag}}\right), \tag{3.4}$$

is equal to 0.4. This index quantifies the pulsatility of the flow and the main direction of the flow. It ranges from 0 (forward flow throughout the cardiac cycle) to 1 (fully reversed flow). An *OSI* index of 0.5 corresponds to a pure oscillating flow with a WSS_{mean} of 0.

Oyre *et al.* (1997) measured the wall shear stresses along the suprarenal and infrarenal portions of the aorta *in vivo* and non-invasively using magnetic resonance velocity mapping. They found WSS of comparable magnitude to our experiments (-1.3 Pa ≤ *WSS* ≤ 4.9 Pa). From their curve of WSS, one can calculate an *OSI* index of 0.32. Cheng, Parker & Taylor (2002) and Taylor *et al.* (2002) did similar measurements with cine phase-contrast magnetic resonance imaging. But, in the case of a patient at rest, they only measured a peak wall shear stress of 2 Pa and a time-average of 0.16 Pa. Their lower

WSS values may be accounted for by the low spatial resolution of their measurements, which only allowed them to measure the velocity at 7 locations across the vessel. A higher resolution is needed to get a good estimate of the gradient of the velocity at the wall.

2. Analytical solution of the flow in a healthy abdominal aorta

Hemodynamics

As a first approximation, the healthy abdominal aorta can be modeled as a straight infinite rigid tube. The flow of a viscous fluid in an infinite tube under a periodic pressure gradient was first studied by Richardson & Tyler (1929). Womersley (1954) and Helps & McDonald (1954) calculated analytical solutions for the arterial pulsating flow expressing the time-varying pressure gradient as the Fourier series of sinusoidal modes (see also Pedley 1979).

In a tube with large *L/d* ratio, the radial motion of the liquid can be neglected and the longitudinal velocity *v* is independent of the distance *y*. The continuity equation is then identically satisfied. The *y*- and *r*-momentum equations that govern the arterial flow can be written in the following non-dimensionalized form

$$\frac{\alpha^2}{Re}\frac{\partial v^*}{\partial t^*} = -\frac{\partial p^*}{\partial y^*} + \frac{1}{Re} r^* \frac{\partial}{\partial r^*}\left(r^* \frac{\partial v^*}{\partial r^*}\right), \tag{3.5a}$$

$$\frac{\partial p^*}{\partial r^*} = 0, \tag{3.5b}$$

in which the longitudinal velocity $v(r,t)$ has been non-dimensionalized by U, the lengths r and y by the radius of the aorta a_0 ($a_0 = d/2$), the time t by the pulsation frequency ω and the pressure p by ρU^2. The stars indicate the dimensionless variables.

The pressure gradient, which is only a function of time (equation (3.5)), can be expressed as a Fourier series with constant coefficients

$$\frac{\partial p^*}{\partial y^*} = -\sum_{n=0}^{\infty} G_n^* e^{int^*}. \tag{3.6}$$

We seek for solutions for the longitudinal velocity under the form of a Fourier series. The solution to equation (3.4) that satisfies the no-slip boundary condition at the walls is

$$v^*(r^*,t^*) = \frac{ReG_0^*}{4}\left(1 - r^{*2}\right) + \frac{Re}{i}\sum_{n=1}^{\infty}\frac{G_n^*}{\alpha_n^2}\left(1 - \frac{J_0(r^* i^{3/2}\alpha_n)}{J_0(i^{3/2}\alpha_n)}\right)e^{int^*}, \tag{3.7}$$

where J_0 is the Bessel function of the first kind of order 0 and $\alpha_n = a_0\sqrt{n\omega/\nu}$. One can remark that $\alpha_1 = a_0\sqrt{\omega/\nu}$ is the Womersley number α previously defined. It is interesting to notice that the time-average term of the Fourier decomposition takes the form of a Poiseuille flow induced by the mean pressure gradient G_0^*.

The velocity profile corresponding to our measurements can be calculated applying the conservation of mass at each instant of time. The input flow rate is

$$Q^*(t^*) = \pi\,\bar{v}^*(t^*) = \frac{\pi\,ReG_0^*}{8} + \sum_{n=1}^{\infty}\frac{ReG_n^*}{i\alpha_n^2}\left(1 - F(\alpha_n)\right)e^{int^*}, \tag{3.8}$$

where $\bar{v}^*$ is the instantaneous velocity, space-averaged over the tube cross-section and

$$F(\alpha_n) = \frac{2}{i^{3/2}\alpha_n}\frac{J_1(i^{3/2}\alpha_n)}{J_0(i^{3/2}\alpha_n)}. \tag{3.9}$$

In order to analyze the above measurements, the input flow rate supplied to the vessel model in our experiment, $Q^*(t^*)$ is decomposed into a Fourier series. The Fourier coefficients of the pressure gradient, G_n^*, are calculated using equation (3.8) and the velocity profile, $v^*(r^*,t^*)$ is then computed from equation (3.7).

Figure 3.3 compares the PIV measurements of the phase-averaged velocity profiles across the abdominal aorta with the profiles predicted by the above Womersley solution for the same flow conditions. The comparison requires changing the variables from the Cartesian coordinate system (x, y) used in the experiment to the cylindrical coordinate system (r, y) used in the analytical solution. This change is valid as long as the

measurements are made in the central axial plane of the model and three-dimensional effects can be neglected. The difference between the experimental and the theoretical profiles is found to be about 8%, whereas the standard deviation between the 6 independent realizations that have been used to compute the average is 3.7%. The agreement between the measured velocity field and the theoretical laminar profile confirms the standard result that although the velocity profile is highly inflectional after the peak systole, the unsteadiness of the flow prevents the instability from developing.

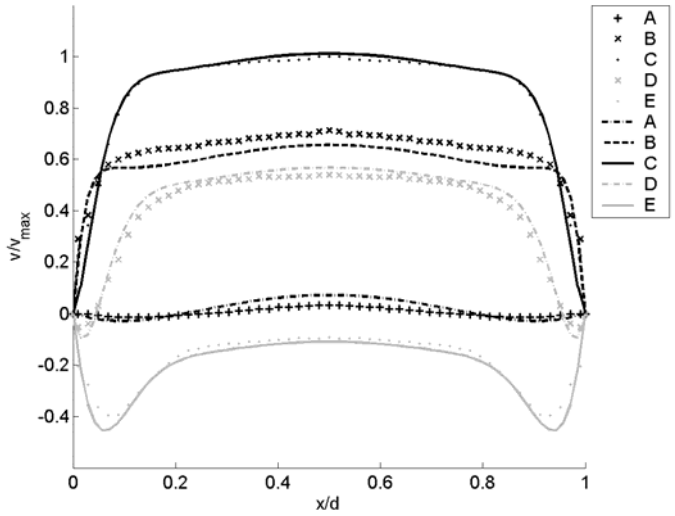

Figure 3.3: Comparison of the velocity profiles across the abdominal aorta measured experimentally with the ones calculated with the Womersley solution.

The differences between the measured and the theoretical profiles may be a consequence of the assumptions used in the analytical model, such as the infinite vessel size. The analytical solution assumes the flow to be fully developed, whereas it may not be quite the case experimentally, since the model of AAA is located only about 20 diameters downstream of the pump. In the experiment, a difference may exist between the output wave profile from the pump and the effective waveform that enters the model. This could be either due to an inaccuracy of the pump or to modifications of the waveform between the outlet of the pump and the model due to entrance effects or to a

weak pressure peak damping. However, it is important to notice, in Figure 3.3, that the first measurement point closest to the wall is almost placed on the theoretical curve at each time step. This should guarantee a good measurement of the wall shear stress.

Wall shear stresses

The wall shear stress can be calculated from the velocity field given in equation

$$WSS^*(t^*) = -\left.\frac{\partial v^*}{\partial r^*}\right|_{r^*=1} = \frac{ReG_0^*}{2} + \sum_{n=1}^{\infty} \frac{ReG_n^*}{2} F(\alpha_n) e^{int^*}. \tag{3.10}$$

The computed time variation of the wall shear stress corresponding to the flow rate used experimentally (Figure 3.1 (*b*)) is shown in Figure 3.4.

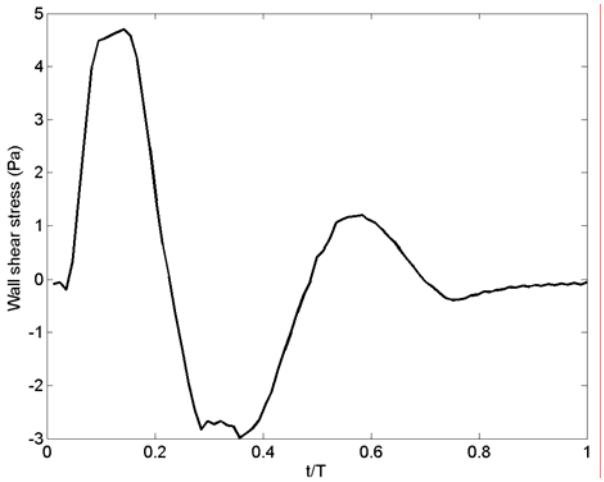

Figure 3.4: Profile of wall shear stresses calculated with the analytical solution in a healthy abdominal aorta over one period.

The theoretical solution predicts a peak WSS of 4.87 Pa, WSS_{mean} = 0.16 Pa, WSS_{mag} = 1.3 Pa and *OSI* = 0.42, which is in good agreement with the measured values, apart from the mean value that is too low. When compared with the WSS profile measured experimentally (Figure 3.2), one can observe a good agreement. The theory, however, predicts a larger slope between the systolic and diastolic peaks. Two explanations may account for this difference in shape. In the experiment, the high frequencies may be

damped, causing a broader systolic peak. The analytical solution may also not correspond to the experimental testing conditions, the assumptions of an infinitely long, rigid model being not satisfied experimentally.

The WSS is the parameter that is physiologically relevant at the level of the endothelial cell response. This section has shown that the WSS fluctuates significantly in a healthy abdominal aorta, where the *OSI* parameter can be between 0.32 and 0.42. As discussed in the introduction, any departure from the healthy pattern of WSS strongly affects the morphology, metabolism and gene expression of the endothelial cells. In the next section, we will analyze how the presence of an AAA influences the spatial and temporal distribution of WSS.

D. Flow in abdominal aortic aneurysms

1. Results of the parametric study of the flow characteristics in AAA

Typical flow in an aneurysm

Before analyzing the effect of aneurysmal growth on the flow topology, we will discuss the important spatial and temporal features, which characterize the typical flow field in an abdominal aortic aneurysm. For that purpose, we have selected an aneurysm with a dilatation ratio D/d = 1.9 and an aspect ratio L/d = 2.9 (model 4). The velocity field was measured in a central axial plane of the aneurysm with the PIV system with a mesh size of $0.068d \times 0.068d$. The vorticity and total stresses were calculated from the velocity field. The total stress is defined as the maximum eigenvalue of the stress tensor (see Appendix B) and is therefore a good measure of the maximum strain rate developing in the flow. It is important to understand how the vorticity and stresses evolve over time inside the aneurysm, since the changes in the wall shear stresses are directly related to them.

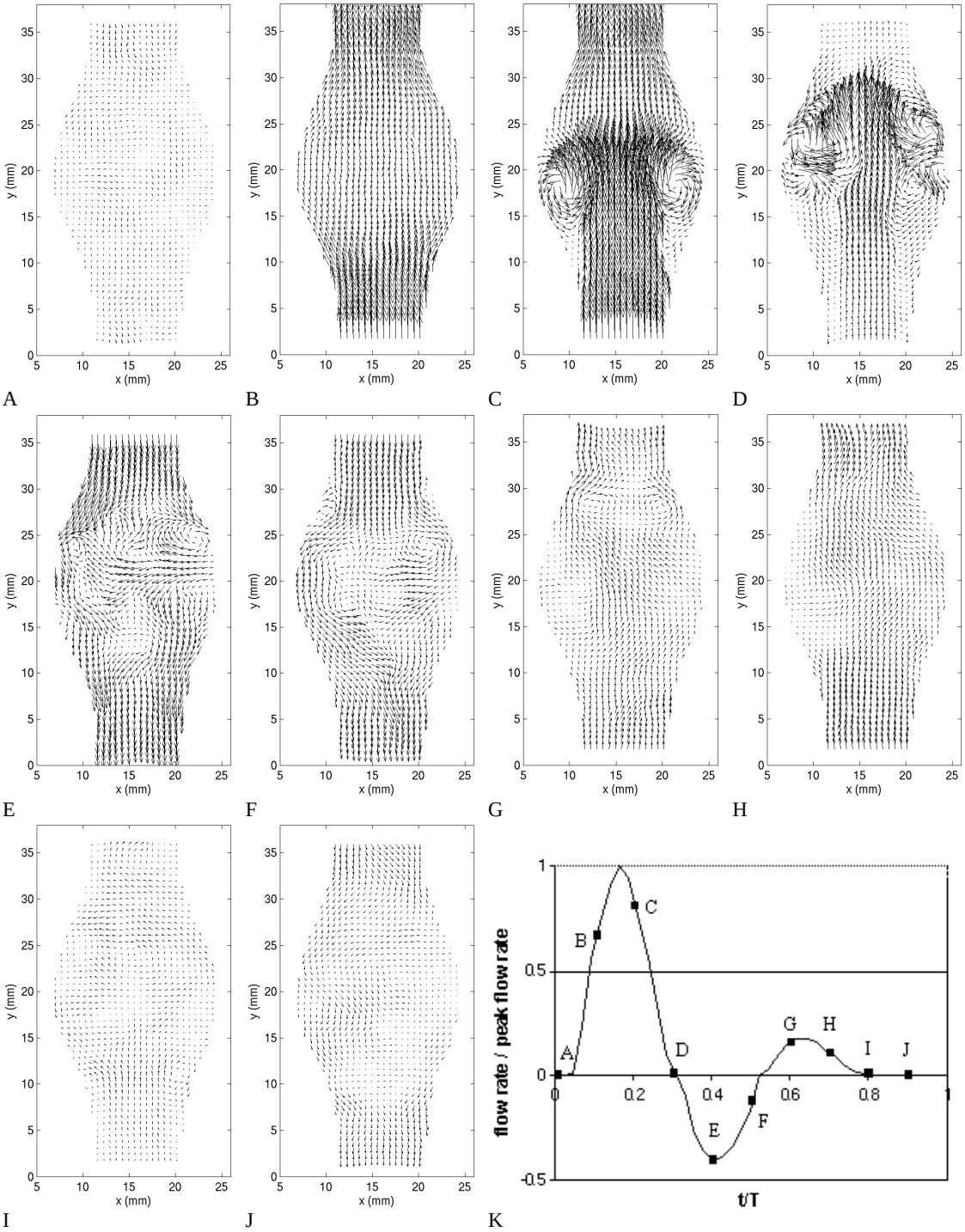

Figure 3.5: Instantaneous velocity field measured in model 4 (*D/d* = 1.9, *L/d* = 2.9) with the PIV system.

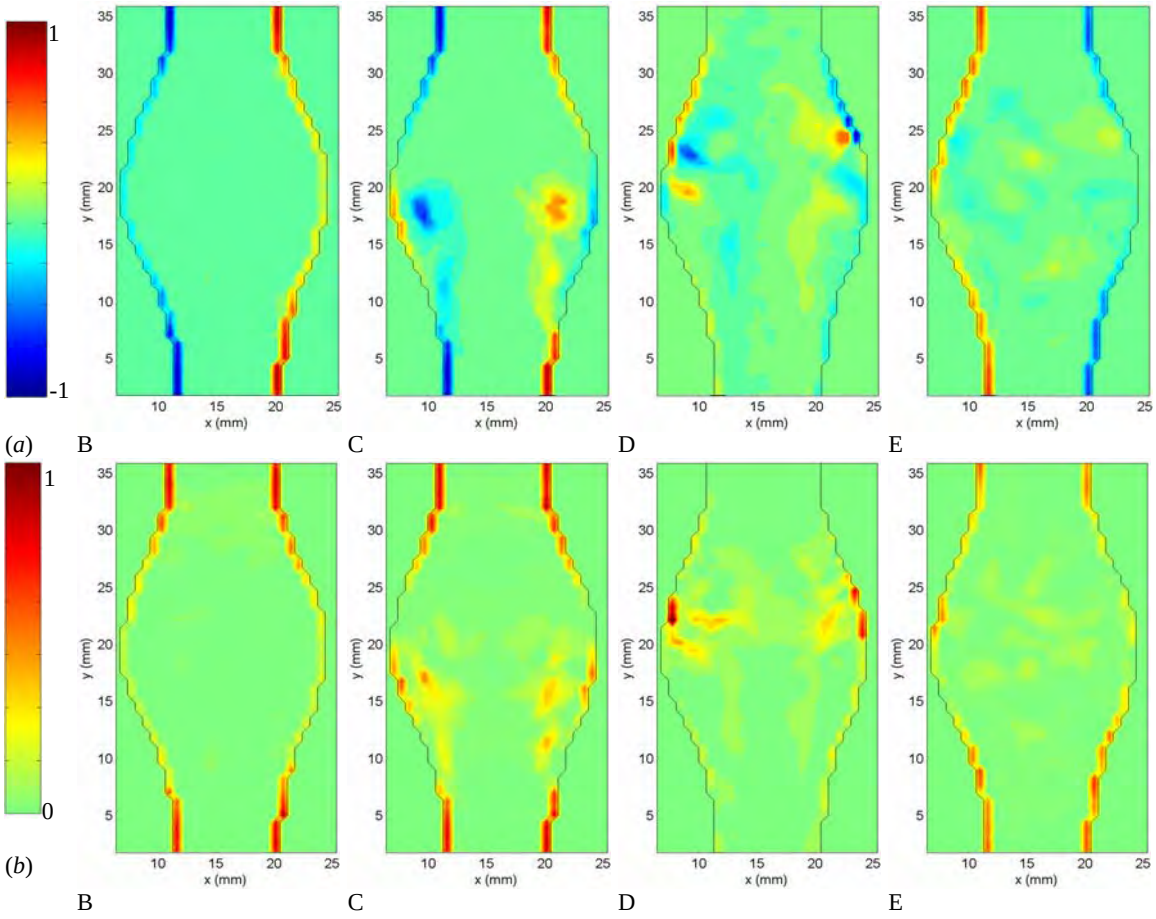

Figure 3.6: (*a*) Instantaneous vorticity and (*b*) stress fields measured in model 4 (*D/d* = 1.9, *L/d* = 2.9) at times B to E, non-dimensionalized by the peak value occurring in the healthy vessel.

During the acceleration portion of the systole, the flow remains laminar and fully attached to the bulging walls (Figures 3.5 and 3.7 (*a*) A-B). The fact that the flow remains attached in the divergent portion is a consequence of the positive pressure gradient generated at the beginning of the systole: the temporal acceleration of the flow is at this point larger than the convective deceleration originated by the upstream (proximal) diverging walls of the artery. Figure 3.6 B shows that, during the entire acceleration portion of the cardiac cycle, the vorticity and stresses are confined to very thin Stokes layers and the bulk of the flow behaves as a potential flow (irrotational and inviscid).

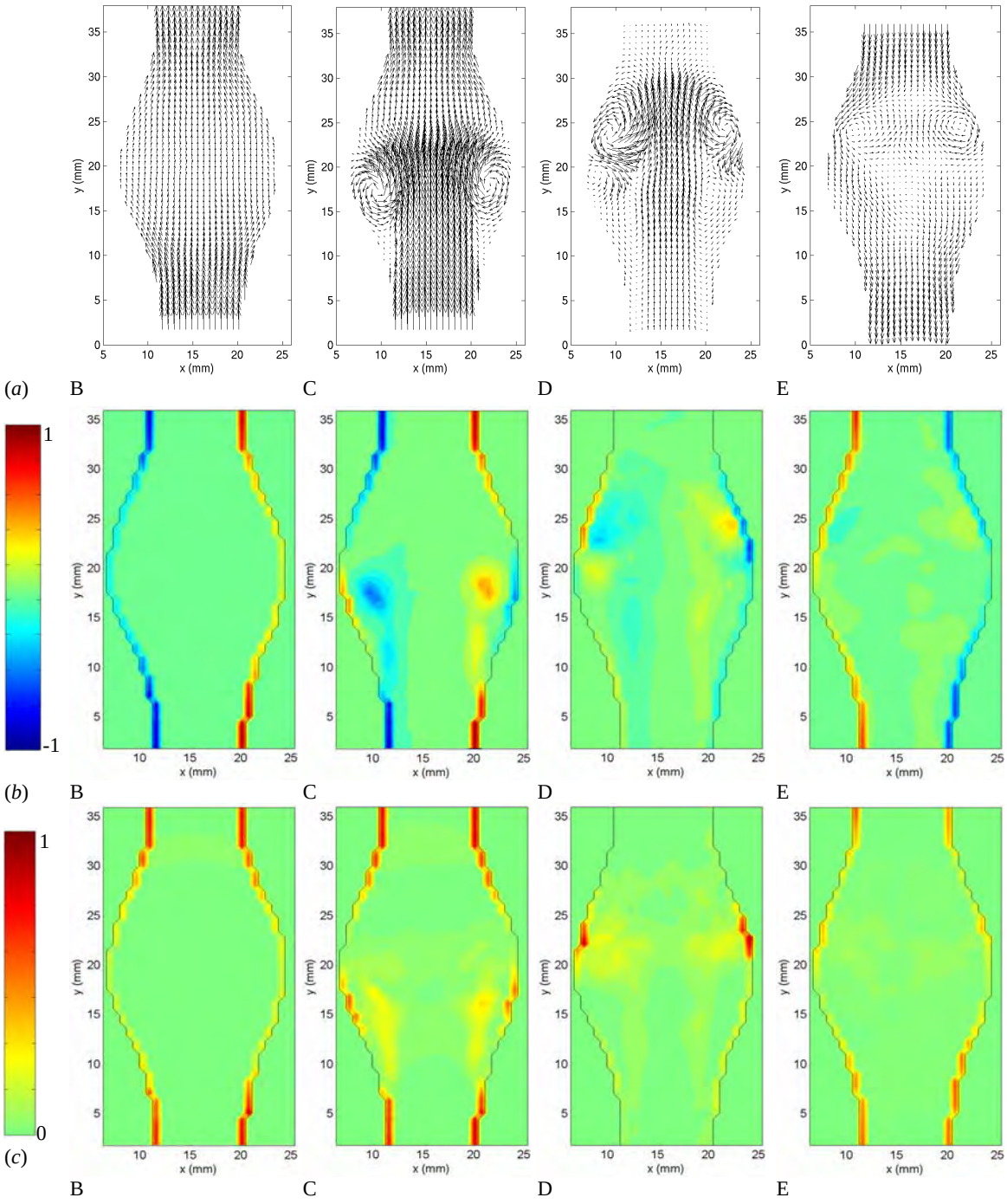

Figure 3.7: (*a*) Velocity, (*b*) vorticity and (*c*) stress fields, at times B to E, measured in model 4 (D/d = 1.9, L/d = 2.9) and phase-averaged over 6 cardiac cycles. The vorticity and stress fields are non-dimensionalized by the peak values occurring in the healthy vessel.

Just after the initiation of the flow deceleration (Figures 3.5 and 3.7 (*a*) C), one can notice the sudden reversal of the velocity field close to the wall, while the bulk of the flow is still moving forward. At this point, the flow detaches from the proximal neck. Downstream of the flow separation, the flow remains laminar and attached to the wall. The vorticity field (Figures 3.6 (*a*) and 3.7 (*b*) C) shows the roll up of the Stokes layer into a large start-up vortex. This intense vortex is followed by a free shear layer, in which some secondary vortices form due to the Kevin Helmholtz instability. The effect of flow separation is also to displace the peak of shear stresses from the wall into the bulk of the flow (Figures 3.6 (*b*) and 3.7 (*c*) C). The wall is now dominated by very low values of shear stresses, with the exception of a small portion, where the WSS is of opposite sign because of the passage of the start-up vortex very close to the wall. The vortex ring leads to a local marked increase in the wall shear stresses.

The vortex ring travels along the aneurysm until it impinges on the distal neck of the AAA (Figures 3.5 and 3.7 (*a*) D), resulting in a sharp increase in wall shear stresses in the converging portion of the AAA. At this point, the cylindrical internal shear layers span across the entire length of the AAA (Figure 3.6 (*a*) D) and the flow is fully detached from the wall along the entire AAA length. At the point of impact, the Stokes layer is again characterized by vorticity and stresses of the opposite sign, because of the presence of the vortex ring.

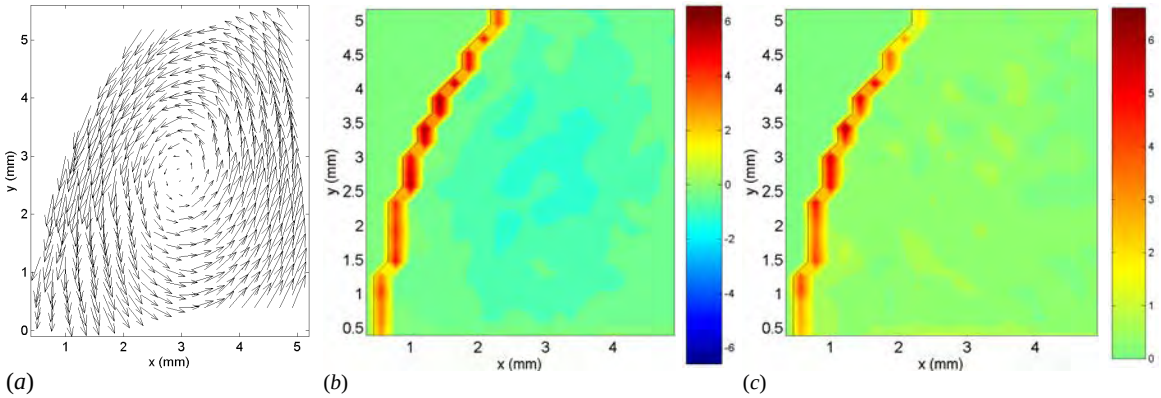

(*a*) (*b*) (*c*)

Figure 3.8: Zoom measurements of the velocity (*a*), vorticity (*b*) and stress (*c*) fields in the distal area of model 4 (*D/d* = 1.9, *L/d* = 2.9). The vorticity and stress values are the ones corresponding to the physiologically correct flow in SI units.

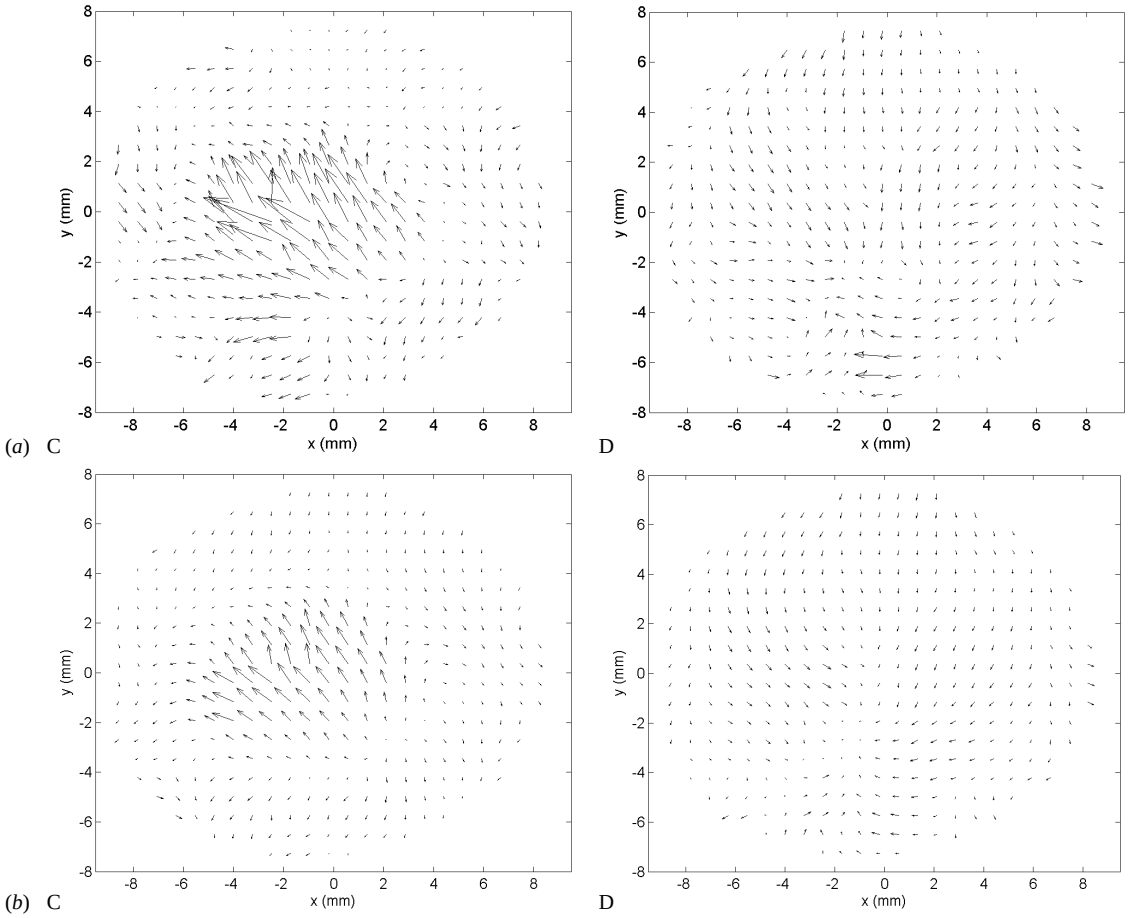

Figure 3.9: Instantaneous (*a*) and phase-averaged (*b*) velocity field measured in the transverse cut located at the point of maximum diameter at times C and D.

However, the characteristic length scale of the Stokes layer becomes so small that the resolution is not sufficient to provide a reliable measurement of the flow characteristics very close to the wall at time D. Therefore, we measured the flow field in model 4, zooming in on the region near the distal wall, in order to increase the resolution (mesh size $0.027d \times 0.027d$). Figure 3.8 shows the velocity, vorticity and stress fields at time D. The measurements show the primary vortex ring hitting the distal wall. On the vorticity

plot (Figure 3.8 (*b*)), one can observe the change in sign of vorticity as one moves from the centerline to the wall passing through the vortex ring. The presence of high velocity so close to the wall induces very thin Stokes layers ($\cong 0.02d$) with high stresses (≥ 6 Pa). Unfortunately, the resolution is still not high enough to resolve the Stokes layer. The measured wall shear stress is therefore still underestimated.

A loss of the two-fold symmetry can be observed on the instantaneous fields as the vortex hits the wall. It corresponds to a loss in axisymmetry, which increases strongly after the vortex ring has hit the distal wall (times E and F). The resulting flow presents a larger randomness, which can be noticed when comparing the instantaneous and phase-averaged fields (Figures 3.5 and 3.6 with 3.7). It is particularly noticeable on the velocity vector plots (Figure 3.5). As the flow reverses in the diastole, the coherent shear layer and the preceding vortex ring break down leading to disordered vortices of decreasing intensity (Figures 3.5 and 3.6 E-F). Even if the Reynolds number is moderate and the range in scale of energetic vortices limited, we will call this stage a weak turbulence. In order to quantify the non-axisymmetry, we measured the velocity field in transverse planes of the AAA. Figure 3.9 shows both the instantaneous and phase-averaged velocity fields measured in the transverse cut located at the point of maximum diameter. At time C, the core of the vortex ring is located right upstream of the measurement plane. The vortex ring must be slightly inclined, since high outward velocity vectors are measured at the center of the aneurysm. However, at time D, a negative radial velocity field is induced at the rear of the vortex ring. Figure 3.9 shows that the loss of symmetry has already occurred at time C.

Near the end of the cardiac cycle corresponding to the resting period of the heart (Figure 3.5 G-J), the turbulence weakens due to vortex entanglement (energy cascade) and viscous dissipation and the flow relaxes back to a near stagnant state. At the beginning of the next cycle, some weak perturbations persist from the dissipated

turbulence. The initial flow conditions are therefore not perfectly identical for each cycle, and a small cycle-to-cycle variation is observed in our measurements.

Effect of the dilatation parameter

In order to assess the effect of the dilatation ratio on the flow topology, the flow field in the decelerating portion of the systole is plotted on Figure 3.10 for 3 comparable models. Models 1, 2 and 5 have the same aspect ratio as model 4, L/d = 2.9, but their dilatation ratio increases linearly with the model number (see Table 2.I). The corresponding vorticity fields are shown on Figure 3.10.

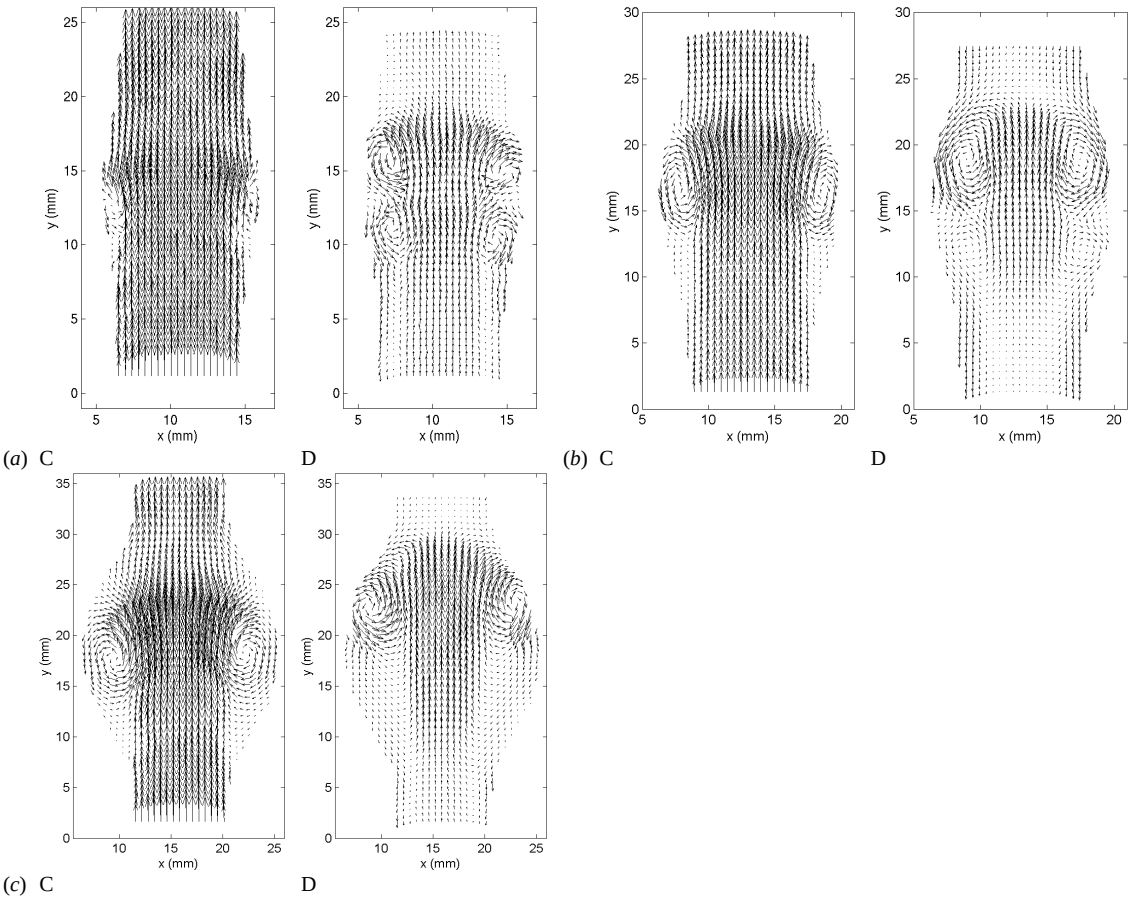

Figure 3.10: Comparison of the phase-averaged velocity field measured with the PIV system in models 1 – D/d = 1.3 (*a*), 2 – D/d = 1.5 (*b*) and 5 – D/d = 2.1 (*c*) at times C and D. A small phase-lag between the different experiments is possible, since the frequency

of acquisition of the measurements is a harmonic of the frequency of the flow, but the relative phase between experiments varies

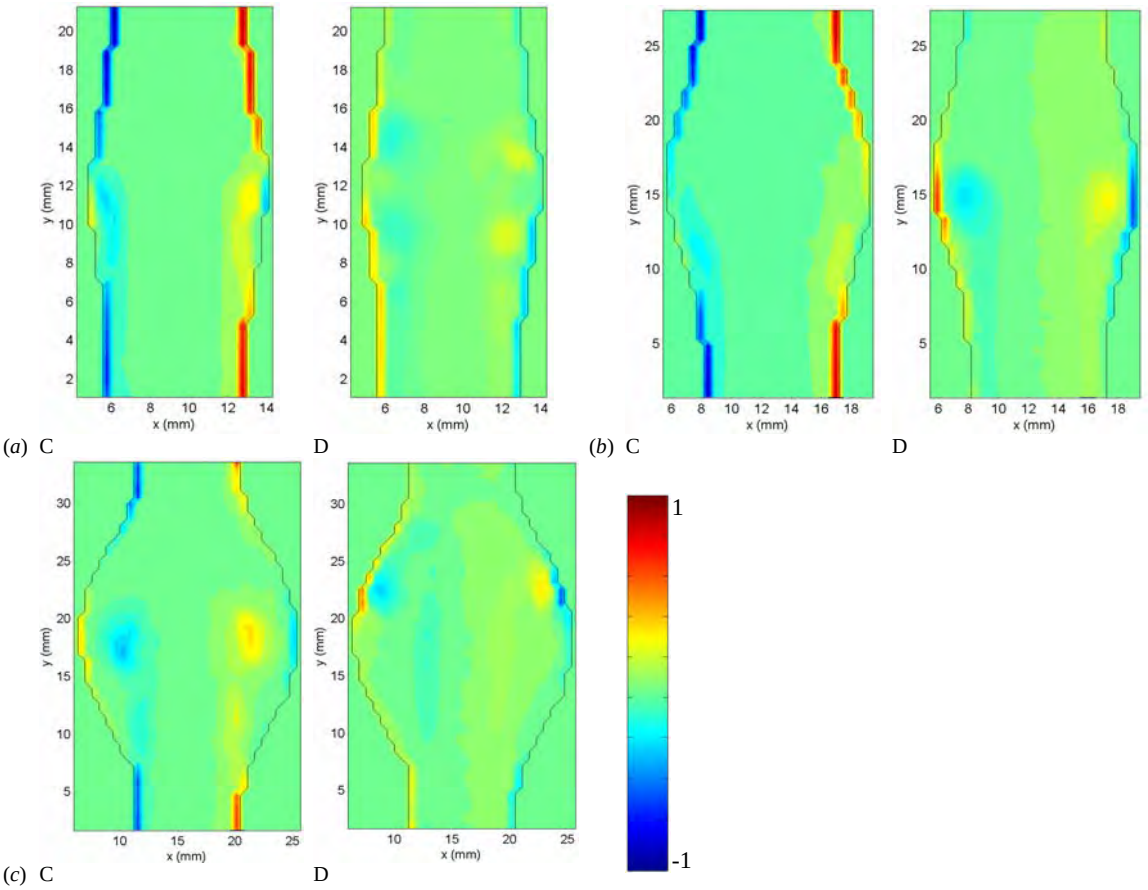

Figure 3.11: Comparison of the phase-averaged vorticity field measured in models 1 – *D/d* = 1.3 (a), 2 – *D/d* = 1.5 (b) and 5 – *D/d* = 2.1 (c) at times C and D, non-dimensionalized by the peak value occurring in the healthy vessel.

It is remarkable that the clinically relevant features of aneurysmal flows, *i.e.* detachment of the flow and impingement on the distal neck, occur even for a dilatation parameter as low as 1.3 for short aneurysms (Figures 3.10 (*a*) and 3.11 (*a*)). Even an incipient aneurysm is characterized by the formation of recirculating zones close to the wall. We can notice that the flow separation occurs around the peak systole in all of the models (between times B and C in Figures 3.10 and 3.11). The time, at which flow separation occurs, does not seem to depend on the dilatation parameter, contrary to the point of flow separation. As the aneurysm grows in size, the point of flow separation gets

closer to the proximal neck. The size of the detached flow region also increases as the dilatation parameter is increased. When *D/d* increases, the detachment becomes more massive and a larger vortex ring is generated. A shear instability length scale can be observed in the shear layer for the small dilatation ratio models. It is of the order of the vessel radius *a* (Figure 3.10 (*a*) and (*b*)). It is, however, impossible to conclude whether this length scale is the primary one or whether vortex pairing has already occurred.

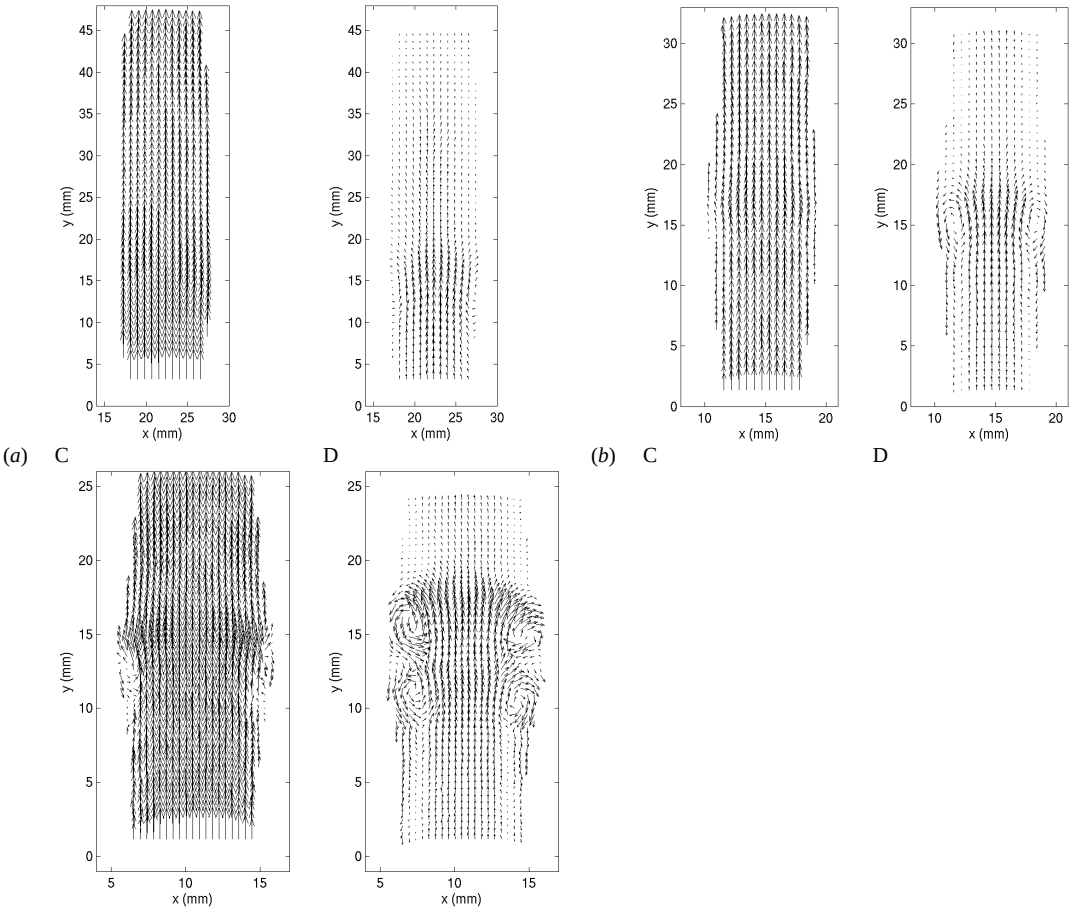

Figure 3.12: Comparison of the phase-averaged velocity field measured in models 11 – *L/d* = 5.2 (*a*), 6 – *L/d* = 3.9 (*b*) and 1 – *L/d* = 2.9 (*c*) at times C and D.

Effect of the aspect ratio

Figure 3.12 features the effects of decreasing the aspect ratio on the phase-averaged velocity fields at times C and D (models 11 – *L/d* = 5.2, 6 – *L/d* = 3.9 and 1 – *L/d* = 2.9).

The models have decreasing aspect ratios, but they all have the same dilatation ratio (*D/d* = 1.3). Figure 3.13 shows the corresponding contours of the phase-averaged vorticity.

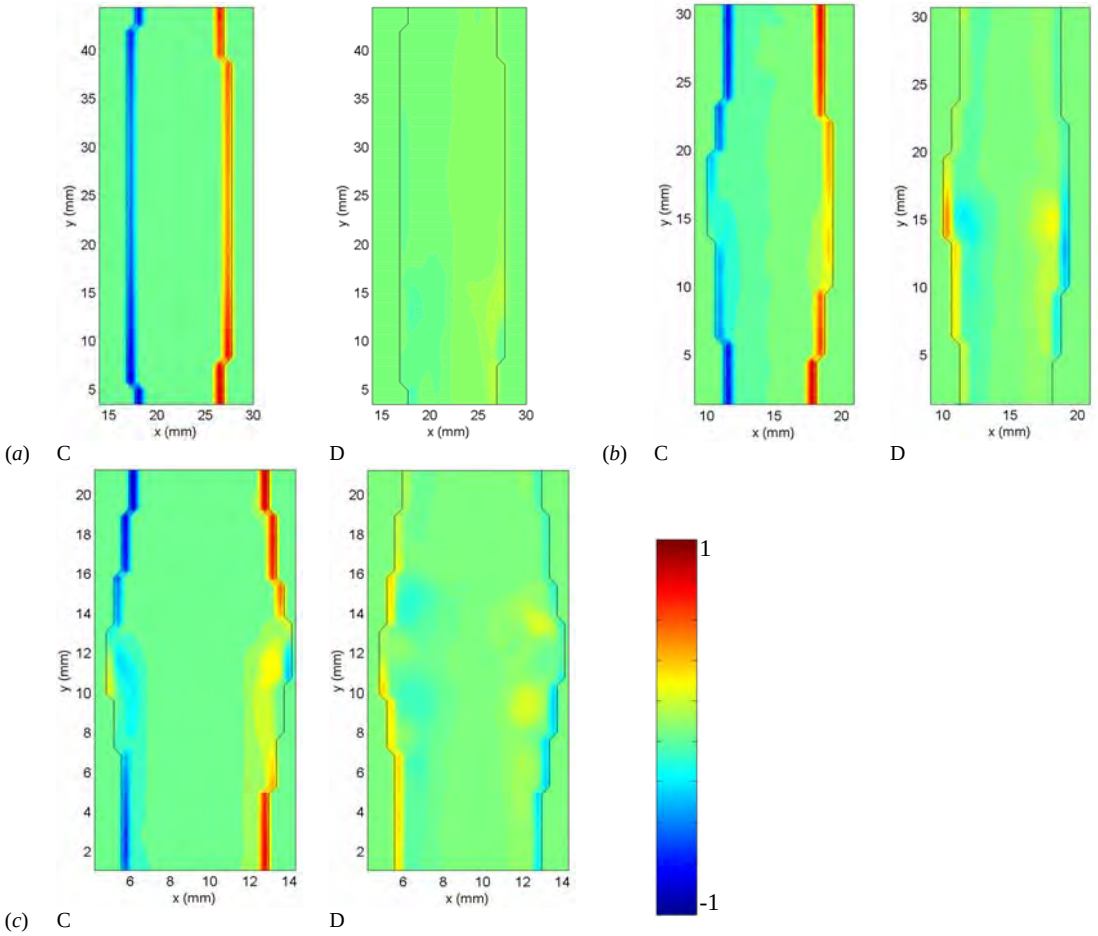

Figure 3.13: Comparison of the phase-averaged vorticity field measured in models 11 – *L/d* = 5.2 (*a*), 6 – *L/d* = 3.9 (*b*) and 1 – *L/d* = 2.9 (*c*) at times C and D, non-dimensionalized by the peak value occurring in the healthy vessel.

A first striking difference is the length traveled by the vortex ring. This length, *l*, measured as the greatest distance between the core of the vortex ring and the proximal neck, was plotted on Figure 3.14 for the different values of *L/d* and *D/d* ratios.

The ratio *l/d* is to be compared with the Strouhal number calculated with the systolic time t_{syst} (Gharib, Rambod & Shariff 1998; Stroud, Berger & Saloner 2000)

$$St_{syst} = \frac{U_{syst} t_{syst}}{d}. \tag{3.11}$$

This Strouhal number is the controlling parameter of the vortex shedding. A characteristic systolic velocity can be chosen as half the peak velocity, which would correspond to an average systolic velocity. The Strouhal number is then found to equal to

$$St_{syst} = \frac{1}{2}\frac{4Q_p}{\pi d^2}\frac{0.16T}{d} = 3. \tag{3.12}$$

since the systolic time is about 16% of the cardiac period *T*. One can see that *l/d* tends to St_{syst}, as *D/d* increases. However the aspect ratio of the model may limit the evolution of the vortex ring, when the length available to the vortex ring to propagate is less than 3*d*, as seen for *L/d* = 2.9. In the models with *L/d* = 2.9, the core of the vortex ring do not go beyond *y/d* = 2.3, which corresponds to the location of the point of impingement on the distal wall. Apart from the case of small aspect ratios, where *L/d* becomes a limiting parameter, the length traveled by the vortex ring inversely scales with *L/d*.

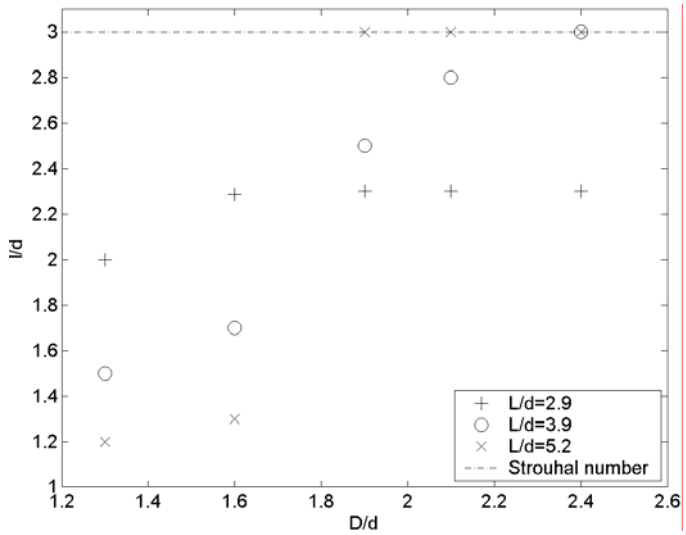

Figure 3.14: Maximum position of the core of the vortex ring inside the AAA plotted as a function of the *D/d* and *L/d* ratios.

The second difference is the time at which flow separation occurs in the cycle. Whereas the flow separates around the peak systole for *L/d* = 2.9 (model 1) (between times B and C on Figures 3.12 (*c*) and 3.13 (*c*)), the separation is delayed to time C for *L/d* = 3.9 (model 6) (Figures 3.12 (*b*) and 3.13 (*b*)) and even further to time D for *L/d* = 5.2 (model 11) (Figures 3.12 (*a*) and 3.13 (*a*)). Since the separation occurs later in the deceleration phase for higher aspect ratios, the generated vortex ring has a reduced strength. This implies that longer aneurysms are less pathological than short ones. An increased length delays the appearance of "disturbed flow" conditions and drastically reduces the magnitude of the vortex strength. As far as the geometrical parameters are concerned, these results correlate well with the ones found by Hatakeyama, Shigematsu & Muto (2001), who characterized the risk factors for rupture as the diastolic pressure, the ratio *D/L* and the expansion rate of the maximum diameter.

2. Results of the parametric study of the wall shear stresses in AAA

Comparison of the WSS in a typical AAA with the reference case

We discuss here the results of the parametric study, concentrating now on the spatial and temporal changes in wall shear stresses, which occur as the AAA enlarges. We shall first present the results obtained in model 4 (*D/d* = 1.9, *L/d* = 2.9) to analyze the general changes that occur in a typical established aneurysm as compared to a healthy abdominal aorta. The effects of the dilatation parameter and aspect ratio will then be discussed in the following subsections.

The wall shear stresses are defined as

$$WSS = 2\mu(\sigma.\vec{n}).\vec{t}, \tag{3.13}$$

$\vec{n}$ and $\vec{t}$ being respectively the normal and tangential unit vectors and

$$\sigma = \frac{1}{2}\mu[\nabla\vec{u} + \nabla\vec{u}^{T}] \tag{3.14}$$

the rate of deformation tensor for a Newtonian fluid.

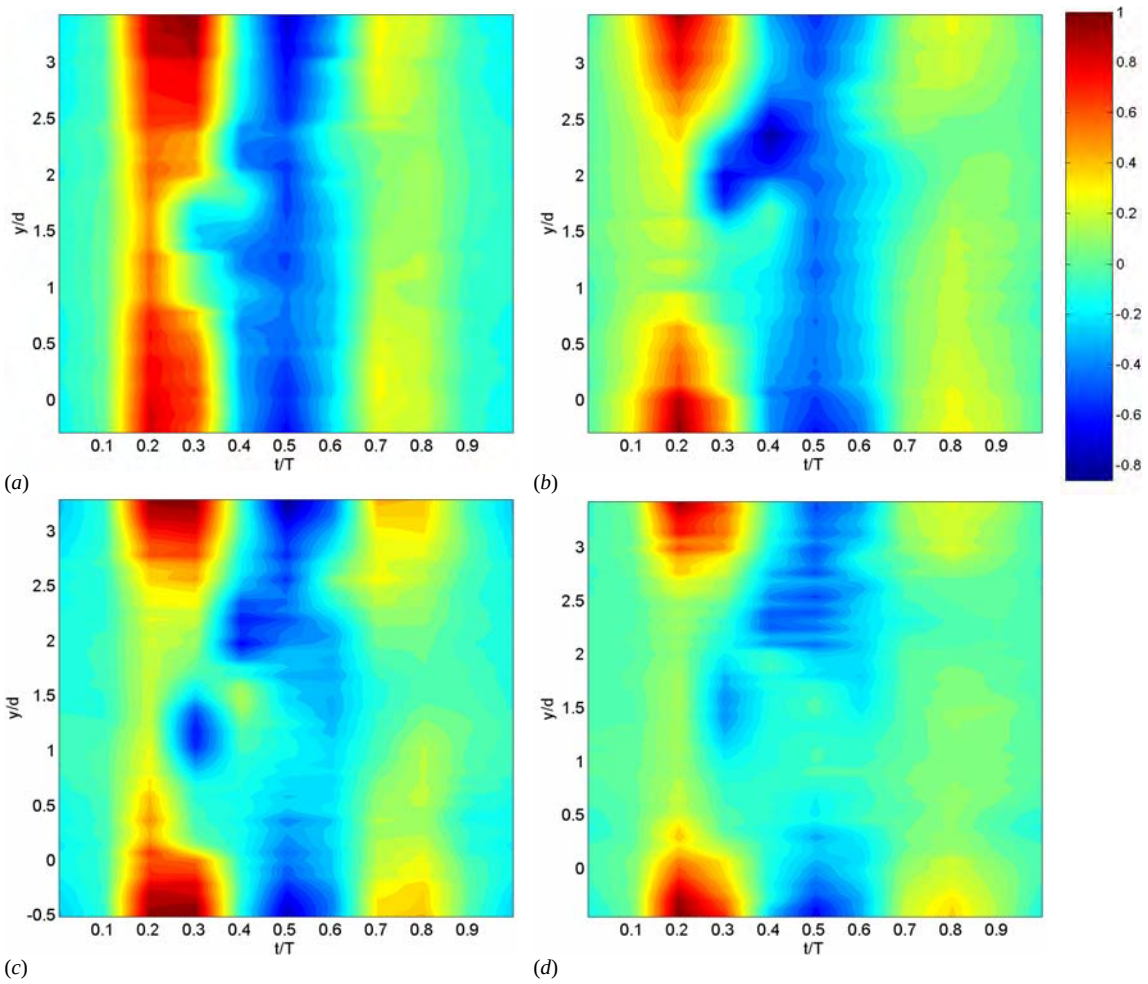

Figure 3.15: Time evolution of the non-dimensionalized, phase-averaged wall shear stresses along the aneurysmal wall in models 1 – D/d = 1.3 (*a*), 2 – D/d = 1.5 (*b*), 4 – D/d = 1.9 (*c*) and 5 – D/d = 2.1 (*d*). y/d = 0 is located at the proximal neck for each of the models. On the time scale, t/T = 0.1 corresponds to time A, t/T = 0.2 to time B, etc.

The phase-averaged WSS, non-dimensionalized by the peak WSS, is shown in Figure 3.15 (*c*) for the case of model 4. In the systole (t/T = 0.2), the WSS decreases as the local diameter increases. The WSS follows a similar trend as the velocity, which inversely scales with the diameter in order to conserve mass. This is due to the fact that the flow is fully attached to the walls at systole. At t/T = 0.3, the flow detaches from the proximal neck (y/d = 0) creating a region of zero WSS between $0 \leq y/d \leq 0.8$. The region of large

negative WSS around y/d = 1.2 is due to the presence of the core of the large primary vortex ring. At t/T = 0.4, the vortex has traveled to y/d = 2.1, but the fact that the measurements are taken at discrete times prevents us from following the vortex ring more closely during its evolution through the AAA. At t/T = 0.4, the vortex ring impinges on the distal wall. However, as discussed in the previous subsection, the WSS value is underestimated at the point of impact, because of the very small size of the Stokes layer and of the resolution of our measurements. Furthermore, the presence of the primary vortex ring so close to the wall induces the roll-up of the Stokes layer into a counter-rotating vortex of smaller size, which can be observed at y/d = 1.5, t/T = 0.4. Upstream of it, the wall still experiences very low WSS ($WSS \cong 0$). At the end of the diastole as well as in the resting period of the cycle, the walls of the entire aneurysm are dominated by very low WSS.

The gradients of the phase-averaged WSS are plotted on Figure 3.16 (*c*). Strong gradients are observed at the proximal and distal necks at times t/T = 0.2, when the changes in WSS are maximum at the necks and t/T = 0.3, when the flow detaches in the aneurysm. The formation of the vortex ring also induces very strong gradients just upstream and downstream of it (t/T = 0.3-0.4). The locations of these regions of high gradients therefore move along with the vortex ring, affecting different parts of the wall over time. But the time, when most of the aneurysm wall experiences strong gradients, occurs after the flow massively detaches from the wall (t/T = 0.3).

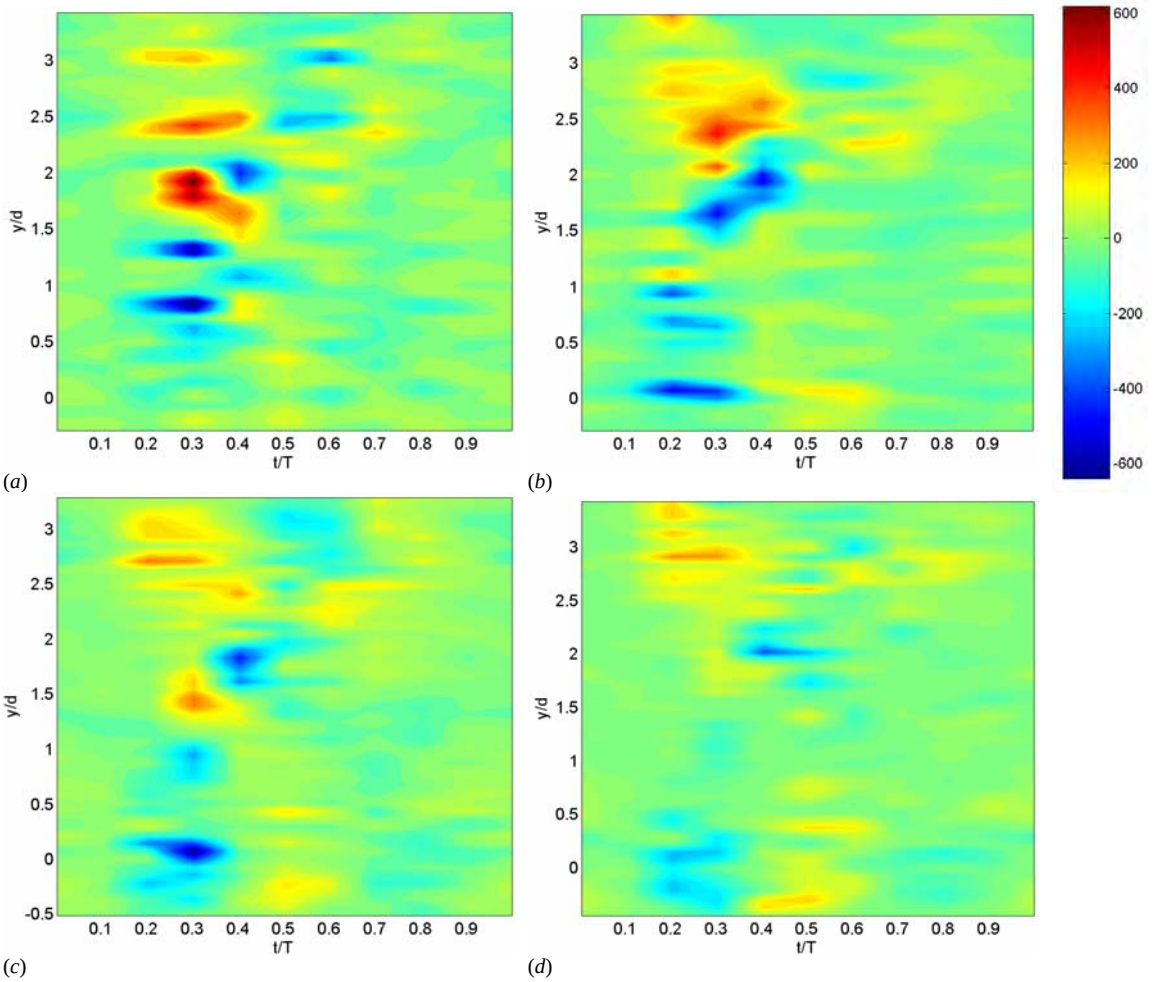

Figure 3.16: Time evolution of the gradient of the phase-averaged wall shear stresses along the aneurysmal wall in models 1 – D/d = 1.3 (*a*), 2 – D/d = 1.5 (*b*), 4 – D/d = 1.9 (*c*) and 5 – D/d = 2.1 (*d*), measured in N/m^3. y/d = 0 is located at the proximal neck for each of the models. On the time scale, t/T = 0.1 corresponds to time A, t/T = 0.2 to time B, etc.

The WSS_{mean}, as defined in section C.1 along with WSS_{mag} and the *OSI* index, sharply drops after the proximal neck to almost zero and remains very low between $0.1 \leq y/D \leq 0.7$. This can be seen on Figure 3.17 (*c*), which shows the WSS_{mean} for model 4. The WSS_{mean} then reaches higher negative values, the negative peaks correlating with the presence of the vortex ring, respectively at times t/T = 0.3 and 0.4. One can observe that, on average, most of the aneurysm wall is subjected to negative WSS_{mean} of small amplitude in the proximal half but large amplitude in the distal half.

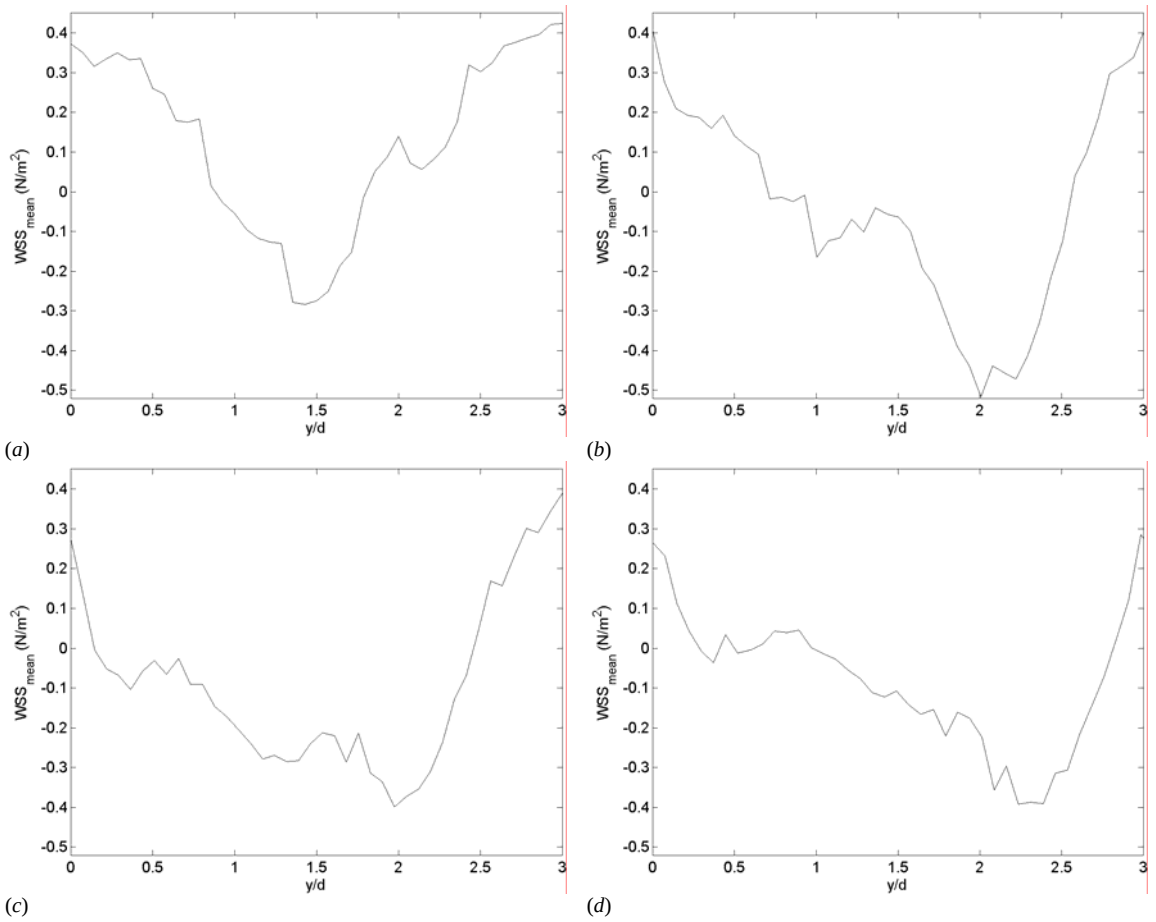

Figure 3.17: Evolution of WSS_{mean} along the aneurysmal wall in models 1 – D/d = 1.3 (*a*), 2 – D/d = 1.5 (*b*), 4 – D/d = 1.9 (*c*) and 5 – D/d = 2.1 (*d*). The results are shown only inside the AAA.

The WSS_{mag} decreases in the proximal half and increases back in the distal half with some fluctuations (see Figure 3.18 (*c*)). One can notice that the values of the healthy vessel are not met at the proximal neck but further upstream, at y/d = -0.4. The presence of the aneurysm partly disrupts the flow at the entrance vessel close to the neck.

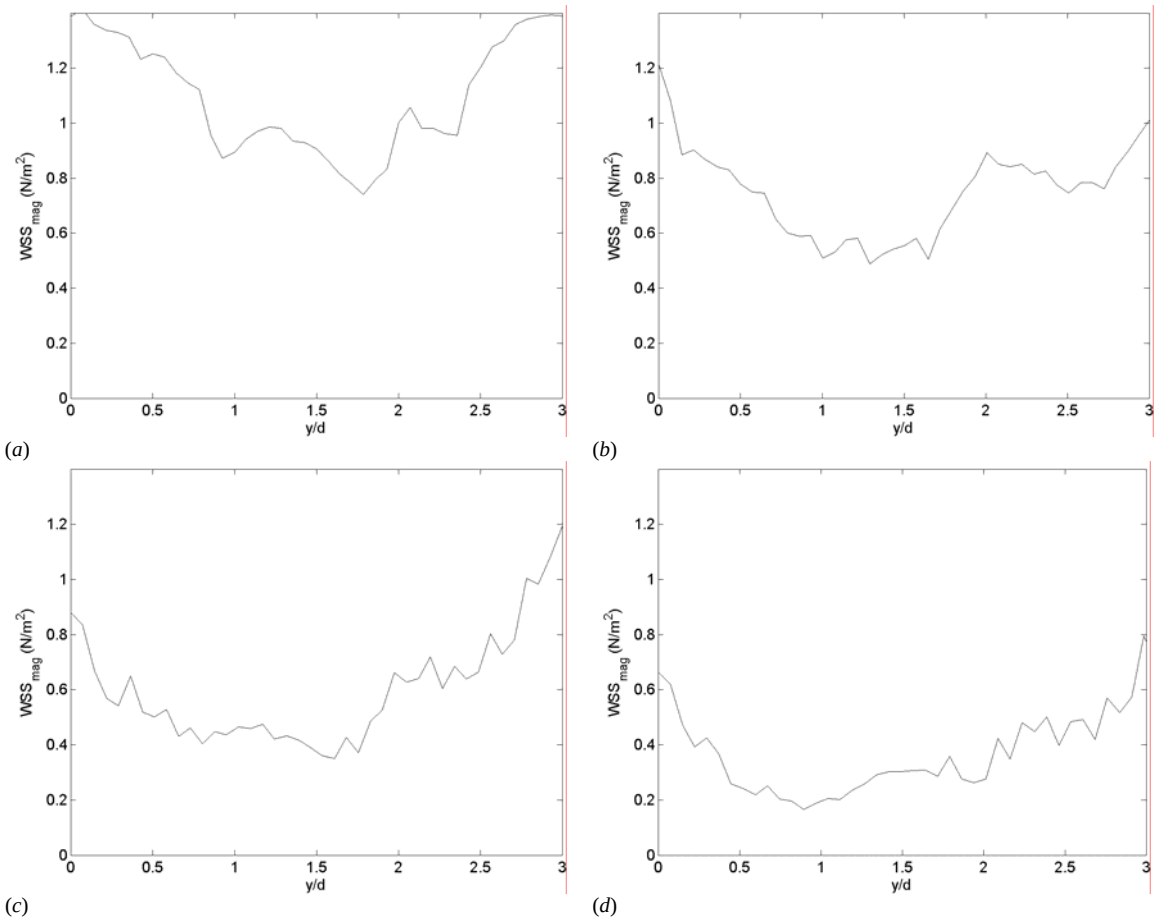

Figure 3.18: Evolution of WSS_{mag} along the aneurysmal wall in models 1 – D/d = 1.3 (*a*), 2 – D/d = 1.5 (*b*), 4 – D/d = 1.9 (*c*) and 5 – D/d = 2.1 (*d*).

The *OSI* index points out the regions of oscillatory flows ($OSI \cong 0.5$) as well as the regions of mean forward ($OSI < 0.5$) or reversed ($OSI > 0.5$) flow. The region of very low WSS_{mean} observed in model 4 ($0.1 \leq y/d \leq 0.7$) is characterized by an *OSI* index close to 0.5 (Figure 3.19 (*c*)). In the regions of high negative WSS_{mean}, the OSI index further increases to reach 0.8 over a large portion of the AAA ($1.3 \leq y/d \leq 2.2$). Most of the aneurysm wall experiences an *OSI* index larger than 0.5, which shows that reversed flow conditions are dominant.

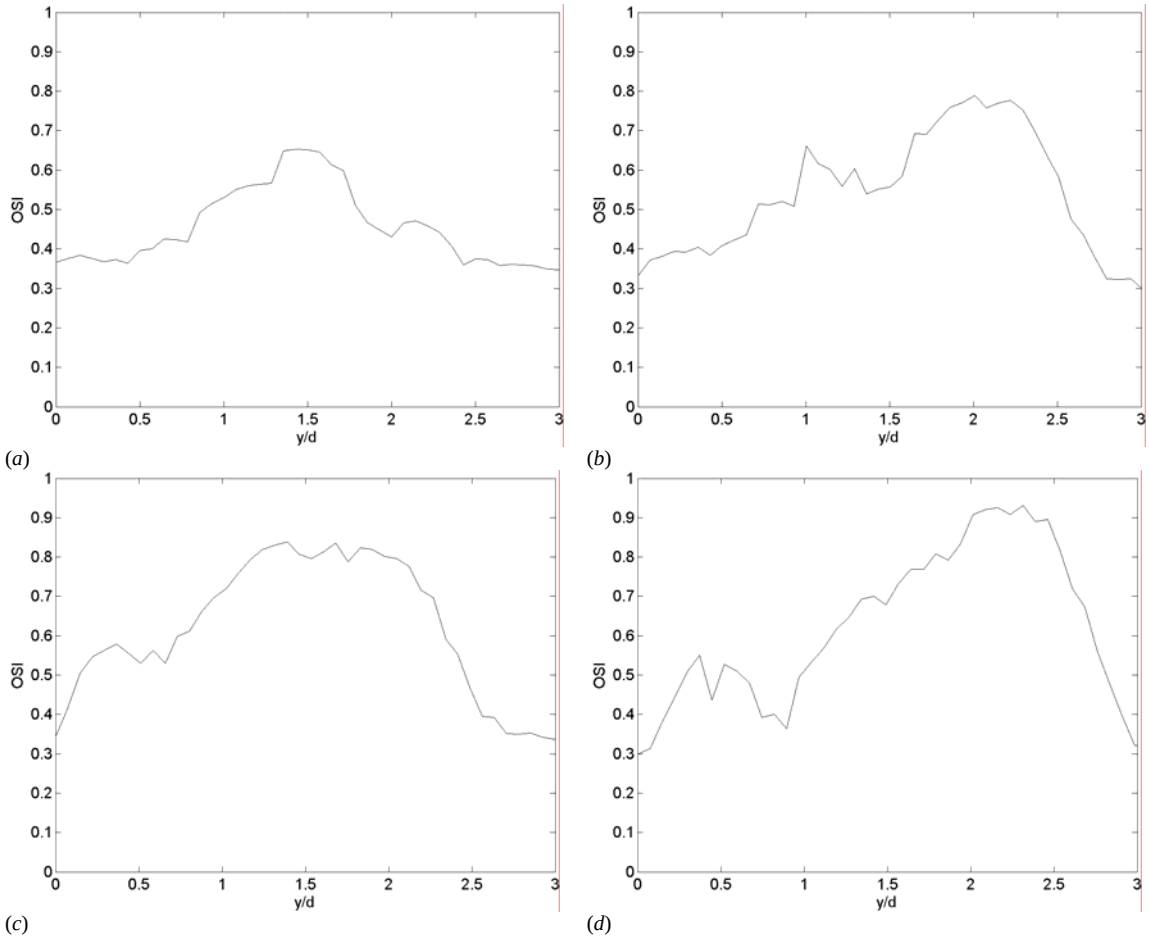

Figure 3.19: Evolution of the OSI factor along the aneurysmal wall in models 1 – *D/d* = 1.3 (*a*), 2 – *D/d* = 1.5 (*b*), 4 – *D/d* = 1.9 (*c*) and 5 – *D/d* = 2.1 (*d*).

Effect of the dilatation parameter on the WSS

In the systole, the decrease of the WSS becomes more pronounced with increasing *D/d* ratio. This can be observed, when comparing the plots of wall shear stresses for models 1, 2, 4 and 5 shown in Figure 3.15. Also, as *D/d* increases, the point of flow separation gets closer to the proximal neck (*y/d* = 0.8 for *D/d* = 1.3 (model 1) to be compared to *y/d* = 0.1 otherwise). So the WSS_{mean} drops more abruptly to near zero values as *D/d* increases (Figure 3.17). The third important effect of the dilatation ratio concerns the size of the detached region. The recirculation region is seen to increase with *D/d*,

increasing from a length equivalent to 1*d* for *D/d* = 1.3 (model 1), to 2*d* for *D/d* = 1.5 (model 2), to the whole length of the aneurysm (2.8*d*) for *D/d* = 2.1 (model 5). The increase in the size of the detached region leads to an increase in the section of the vessel wall subjected to a reversed flow, characterized by a negative mean WSS (Figure 3.17) and an *OSI* index greater than 0.5 (Figure 3.19). The accentuation of the drop in WSS in the systole and the increase in size of the regions subjected to very low WSS are responsible for the gradual decrease in WSS_{mag} as *D/d* increases (Figure 3.18). The average value of the WSS_{mag} inside the AAA drops from 1.1 Pa for *D/d* = 1.3 (model 1), to 0.75 Pa for *D/d* = 1.5 (model 2), to 0.60 Pa for *D/d* = 1.9 (model 4) and finally to 0.37 Pa for *D/d* = 2.1 (model 5). The decrease in WSS_{mag} causes an increase in the maximum value of the *OSI* index (Figure 3.19), so that the index average value dramatically increases as *D/d* increases. The dilatation ratio does not seem to influence the amplitude of the negative WSS at the location of the vortex ring.

Effect of the aspect ratio on the WSS

For a same dilatation parameter *D/d*, the main effect of increasing the aspect ratio of the aneurysm is to make all the above described changes in the patterns of WSS less pronounced. Figure 3.20 shows the spatial and temporal evolution of the WSS in models 11, 6 and 1, which have a dilatation ratio of 1.3 and decreasing aspect ratios (5.2, 3.9 and 2.9). In the systole, the effect of the dilatation is visible for all the models. Note that, even in model 11, the increase in diameter leads to a decrease in WSS.

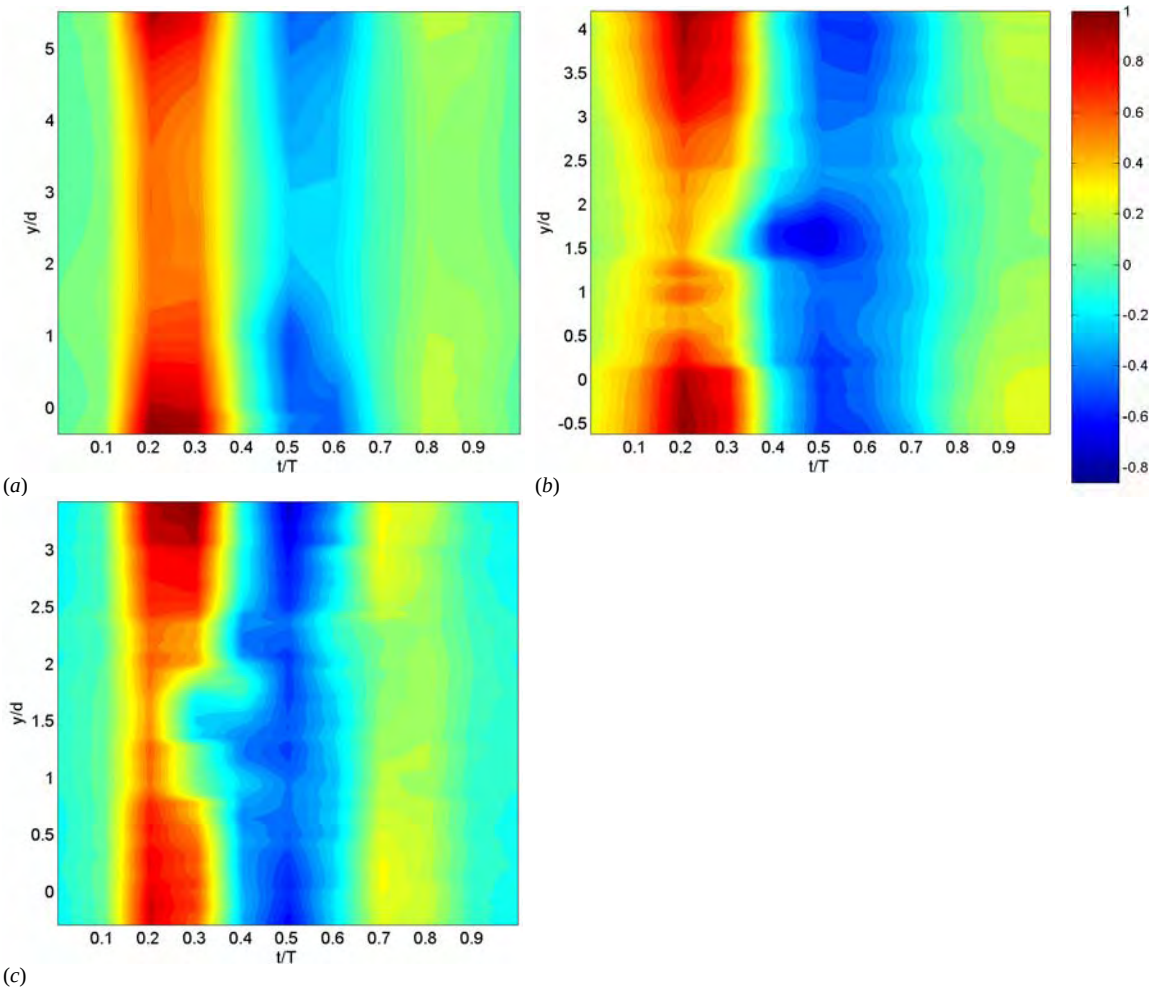

Figure 3.20: Time evolution of the non-dimensionalized, phase-averaged wall shear stresses along the aneurysmal wall in models 11 – L/d = 5.2 (*a*), 6 – L/d = 3.9 (*b*) and 1 – L/d = 2.9 (*c*). y/d = 0 is located at the proximal neck for each of the models. On the time scale, t/T = 0.1 corresponds to time A, t/T = 0.2 to time B, etc.

As L/d increases, the flow separation is delayed, as shown in Figure 3.20. It is observed to occur only at t/T = 0.3 for L/d = 3.9 (model 6) and at t/T = 0.4 for L/d = 5.2 (model 11). The vortex ring, generated at a later time in the cardiac cycle, is therefore weaker in intensity, inducing smaller negative WSS. The delay of the flow separation to instants when the WSS are smaller and the decrease in intensity of the vortex ring are the reasons for the very large decrease in WSS gradients measured as L/d increases (Figure 3.21). Note that, in model 11, the GWSS drop to negligible values (Figure 3.21 (*a*)). In

this case, the flow separation is so incipient that no appreciable vortex ring is seen forming, which explains why the WSS_{mean} (Figure 3.22 (*a*)) and the *OSI* index (Figure 3.23 (*a*)) remain in the normal range measured in the healthy abdominal aorta. For the rest of the discussion, we will now set model 11 aside, since it is the only model not to exhibit the classical characteristics of the flow in an AAA.

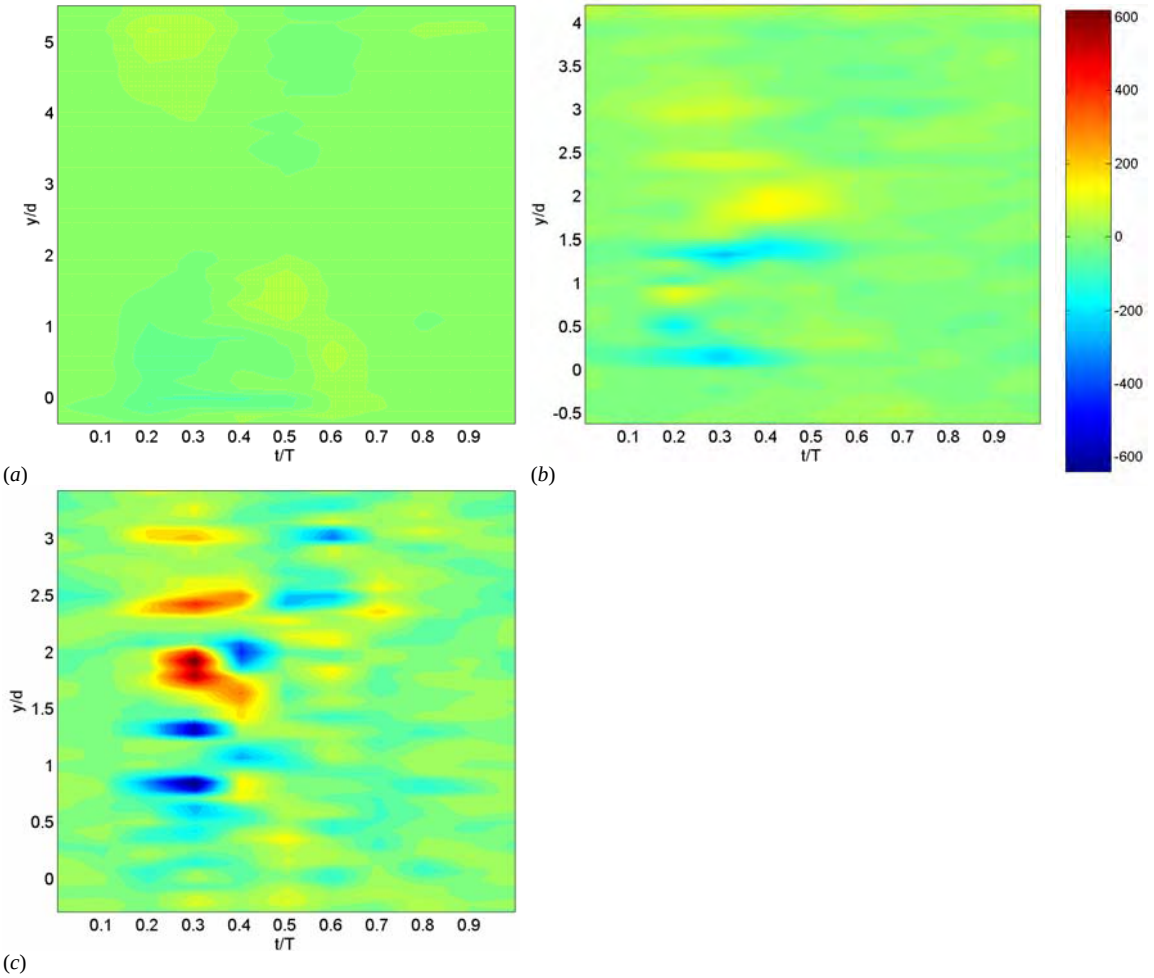

Figure 3.21: Time evolution of the gradient of the phase-averaged wall shear stresses along the aneurysmal wall in models 11 – *L/d* = 5.2 (*a*), 6 – *L/d* = 3.9 (*b*) and 1 – *L/d* = 2.9 (*c*), measured in N/m^3. *y/d* = 0 is located at the proximal neck for each of the models. On the time scale, *t/T* = 0.1 corresponds to time A, *t/T* = 0.2 to time B, etc.

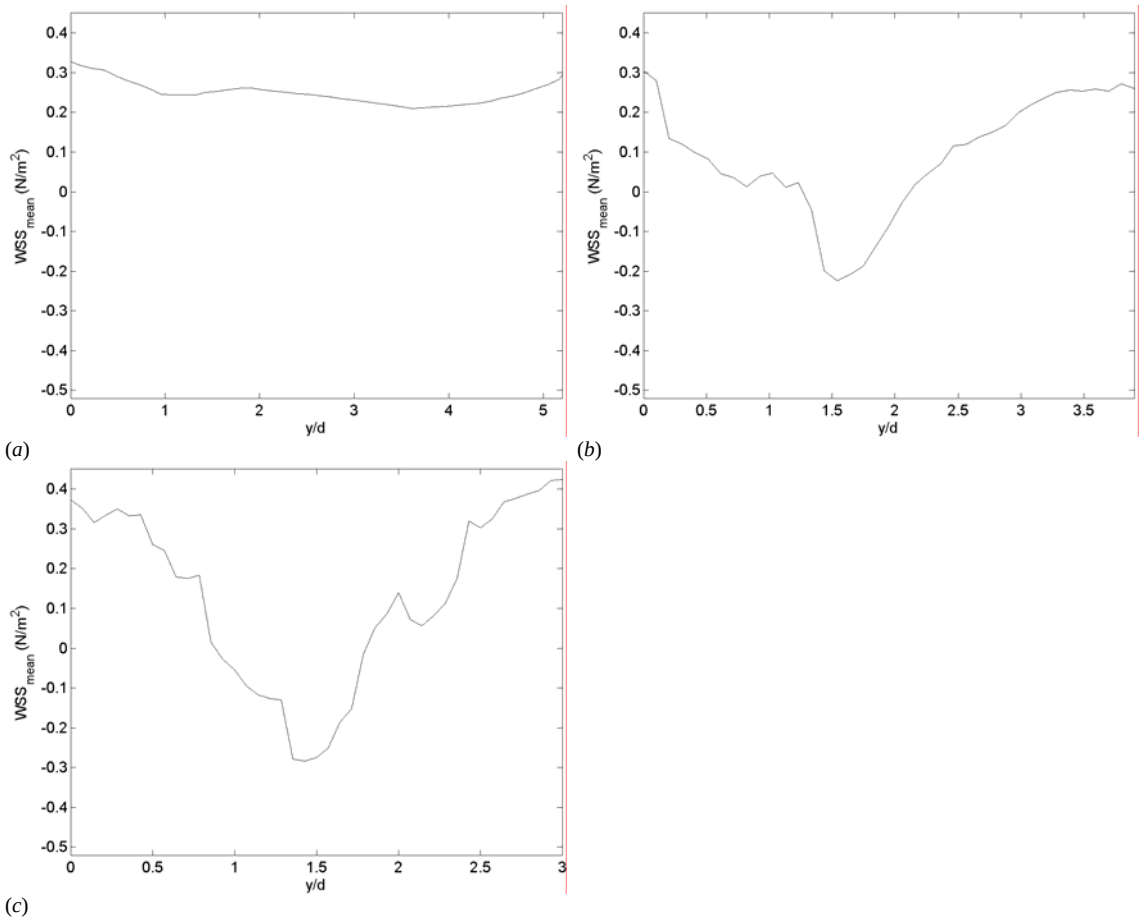

Figure 3.22: Evolution of WSS_{mean} along the aneurysmal wall in models 11 – L/d = 5.2 (*a*), 6 – L/d = 3.9 (*b*) and 1 – L/d = 2.9 (*c*). The results are shown only inside the AAA.

One can notice that the relevant parameters, such as the WSS_{mean} or the *OSI* index, have a similar variation in space for both models. The values are practically identical in each case and the maximum in *OSI* or the minimum in WSS_{mean} occur at the same location, although the length of the models is different. This shows that the L/d parameter has little effect on the physical processes that occur inside the AAA.

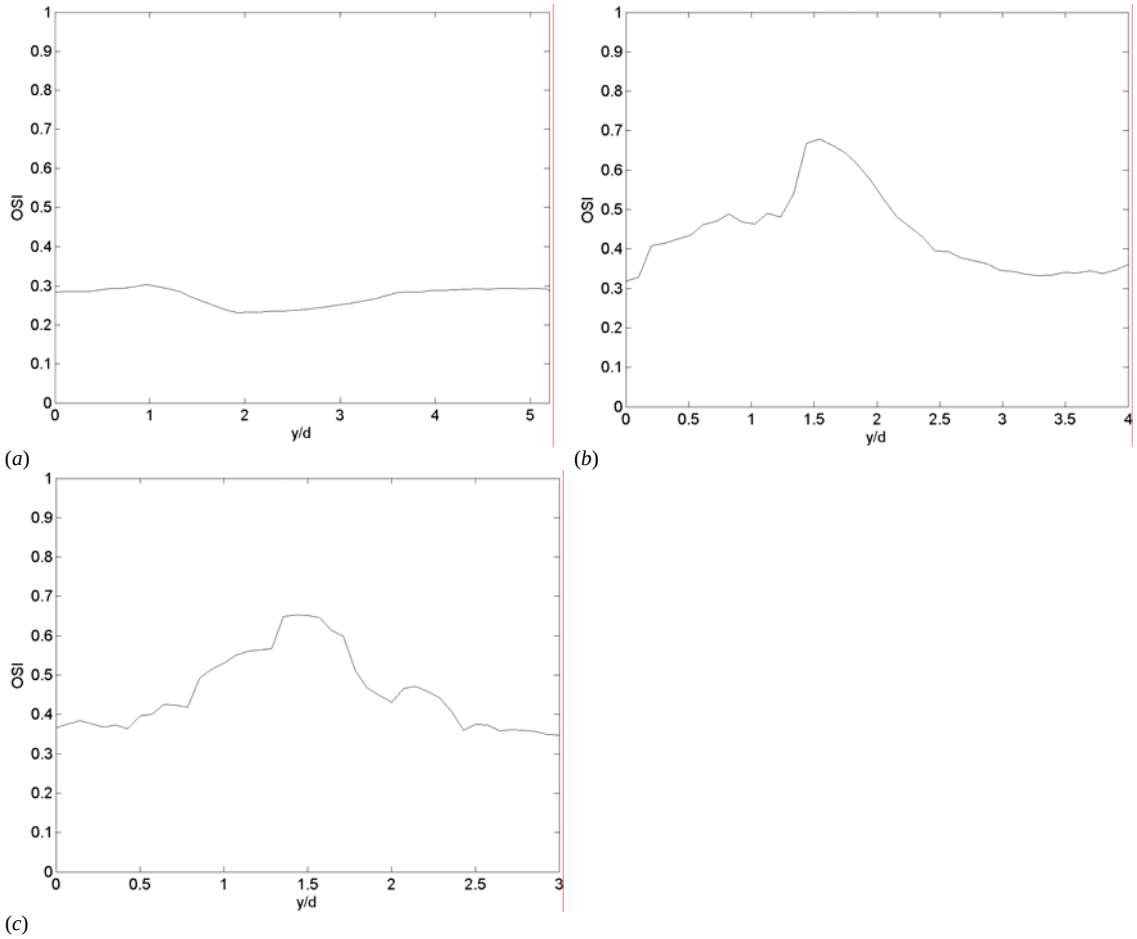

Figure 3.23: Evolution of the *OSI* index along the aneurysmal wall in models 11 – L/d = 5.2 (*a*), 6 – L/d = 3.9 (*b*) and 1 – L/d = 2.9 (*c*).

3. Analytical solution for a slowly expanding abdominal aorta

Hemodynamics

The study of the changes in the WSS resulting from very small dilatations of the abdominal aorta, prior to their development into an aneurysm, is crucial for a better understanding of the etiology of the disease. An analytical solution of the flow in an incipient aneurysm, such as the one studied in model 11 (D/d = 1.3, L/d = 5.2), would therefore be a useful tool to study the evolution of AAAs in a systematic way.

One can obtain an analytical solution for the WSS by extending the case of a straight pipe, shown in section C.2, to a slowly expanding pipe. In this case, the radial velocity,

$u_r(y, r, t)$, cannot be neglected. Using the dimensionless variables introduced in section C.2, the equation of mass conservation can be written as

$$\frac{\partial u_r^*}{\partial r^*} + \frac{u_r^*}{r^*} + \frac{\partial v^*}{\partial y^*} = 0 \tag{3.15}$$

and the y- and r-momentum equations as

$$\frac{\alpha^2}{Re}\frac{\partial v^*}{\partial t^*} + u_r^*\frac{\partial v^*}{\partial r^*} + v^*\frac{\partial v^*}{\partial y^*} = -\frac{\partial p^*}{\partial y^*} + \frac{1}{Re}\left(\frac{\partial^2 v^*}{\partial y^{*2}} + \frac{1}{r^*}\frac{\partial}{\partial r^*}\left(r^*\frac{\partial v^*}{\partial r^*}\right)\right), \tag{3.16a}$$

$$\frac{\alpha^2}{Re}\frac{\partial u_r^*}{\partial t^*} + u_r^*\frac{\partial u_r^*}{\partial r^*} + v^*\frac{\partial u_r^*}{\partial y^*} = -\frac{\partial p^*}{\partial r^*} + \frac{1}{Re}\left(\frac{\partial^2 u_r^*}{\partial y^{*2}} + \frac{\partial^2 u_r^*}{\partial r^{*2}} + \frac{\partial (u_r^*/r^*)}{\partial r^*}\right). \tag{3.16b}$$

Let Λ be the characteristic length along which the local radius $a(y)$ varies, *i.e.* $\Lambda = a_0 da/dy$. We assume that the changes in the y-velocity, $v^*(y^*, r^*, t^*)$, are small along y. We therefore introduce a new variable $Y^* = \varepsilon y^*$, where the small parameter ε is defined as $\varepsilon = \Lambda / a_0$. Furthermore, we define a new radial velocity, U_r^*, such that $u_r^* = \varepsilon U_r^*$ with U_r^* of order 1 and a new pressure $P^* = \varepsilon p^*$. With the introduction of these new variables, the conservation of mass and momentum equations become

$$\frac{\partial U_r^*}{\partial r^*} + \frac{U_r^*}{r^*} + \frac{\partial v^*}{\partial Y^*} = 0 \tag{3.17}$$

$$\frac{\alpha^2}{Re}\frac{\partial v^*}{\partial t^*} + \varepsilon U_r^*\frac{\partial v^*}{\partial r^*} + \varepsilon v^*\frac{\partial v^*}{\partial Y^*} = -\frac{\partial P^*}{\partial Y^*} + \frac{1}{Re}\left(\varepsilon^2\frac{\partial^2 v^*}{\partial Y^{*2}} + \frac{1}{r^*}\frac{\partial}{\partial r^*}\left(r^*\frac{\partial v^*}{\partial r^*}\right)\right), \tag{3.18a}$$

$$\frac{\alpha^2}{Re}\frac{\partial U_r^*}{\partial t^*} + \varepsilon U_r^*\frac{\partial U_r^*}{\partial r^*} + \varepsilon v^*\frac{\partial U_r^*}{\partial Y^*} = -\frac{1}{\varepsilon^2}\frac{\partial P^*}{\partial r^*} + \frac{1}{Re}\left(\varepsilon^2\frac{\partial^2 U_r^*}{\partial Y^{*2}} + \frac{\partial^2 U_r^*}{\partial r^{*2}} + \frac{\partial (U_r^*/r^*)}{\partial r^*}\right). \tag{3.18b}$$

Assuming α^2/Re of order unity[3], the leading order of equation (3.18*b*) leads to $\partial P^*/\partial r^* = 0$. At the first order, the momentum equations are decoupled and reduce to the

[3] In the abdominal aorta of a healthy adult male at rest, $\alpha \approx 10$ and $\langle \overline{Re} \rangle \approx 300$, so that $\alpha^2 / Re \approx 1$.

ones corresponding to the straight pipe. The dimensionless longitudinal velocity $v^*(Y^*, r^*, t^*)$ is then given by

$$v^* = \frac{ReG_0^*}{4}(R^{*2} - r^{*2}) + \sum_{n=1}^{\infty} \frac{ReG_n^* R^{*2}}{i\alpha_n^2}\left(1 - \frac{J_0(i^{3/2}\alpha_n r^*/R^*)}{J_0(i^{3/2}\alpha_n)}\right)e^{int^*}. \tag{3.19}$$

where $R^*(Y^*) = a(Y^*)/a_0$ is the dimensionless local radius, $\alpha_n(Y^*) = a(Y^*)\sqrt{n\omega/\nu}$ is the Womersley number corresponding to the n^{th} harmonic of the pulsation ω and $G_n^*(Y^*)$ is the n^{th} Fourier coefficient of the pressure gradient $\partial P^*/\partial Y^*$.

To achieve mass conservation, the flow rate at any location Y^* inside the aneurysm

$$Q^* = \int_0^{R^*} 2\pi r^* v^* dr^* = \frac{\pi ReG_0^* R^{*4}}{8} + \sum_{n=1}^{\infty} \frac{\pi ReG_n^* R^{*4}}{i\alpha_n^2}[1 - F(\alpha_n)]e^{int^*}. \tag{3.20}$$

must be equal to the flow rate input at the pump

$$Q^* = \int_0^1 2\pi r^* v^*(Y^* = 0, r^*, t^*) dr^*, \tag{3.21}$$

which is only a function of time. Therefore the Fourier coefficients of the flow rate cannot depend on Y^*, which implies

$$G_0^* R^{*4} = \text{const}, \tag{3.22a}$$

$$G_n^* R^{*2}[1 - F(\alpha_n)] = \text{const}. \tag{3.22b}$$

The radial velocity $U_r^*(Y^*, r^*, t^*)$ is then calculated integrating the mass conservation equation (3.17) along with the conditions (3.22).

$$U_r^* = \frac{ReG_0^* R^{*2}}{4}\frac{dR^*}{dY^*}\frac{r^*}{R^*}\left(1 - \frac{r^{*2}}{R^{*2}}\right) + \sum_{n=1}^{\infty} \frac{ReG_n^* R^{*2}}{4}\frac{dR^*}{dY^*}\frac{F(\alpha_n)^2}{1 - F(\alpha_n)}\left(\frac{r^*}{R^*} - \frac{J_1(i^{3/2}\alpha_n r^*/R^*)}{J_1(i^{3/2}\alpha_n)}\right)e^{int^*}. \tag{3.23}$$

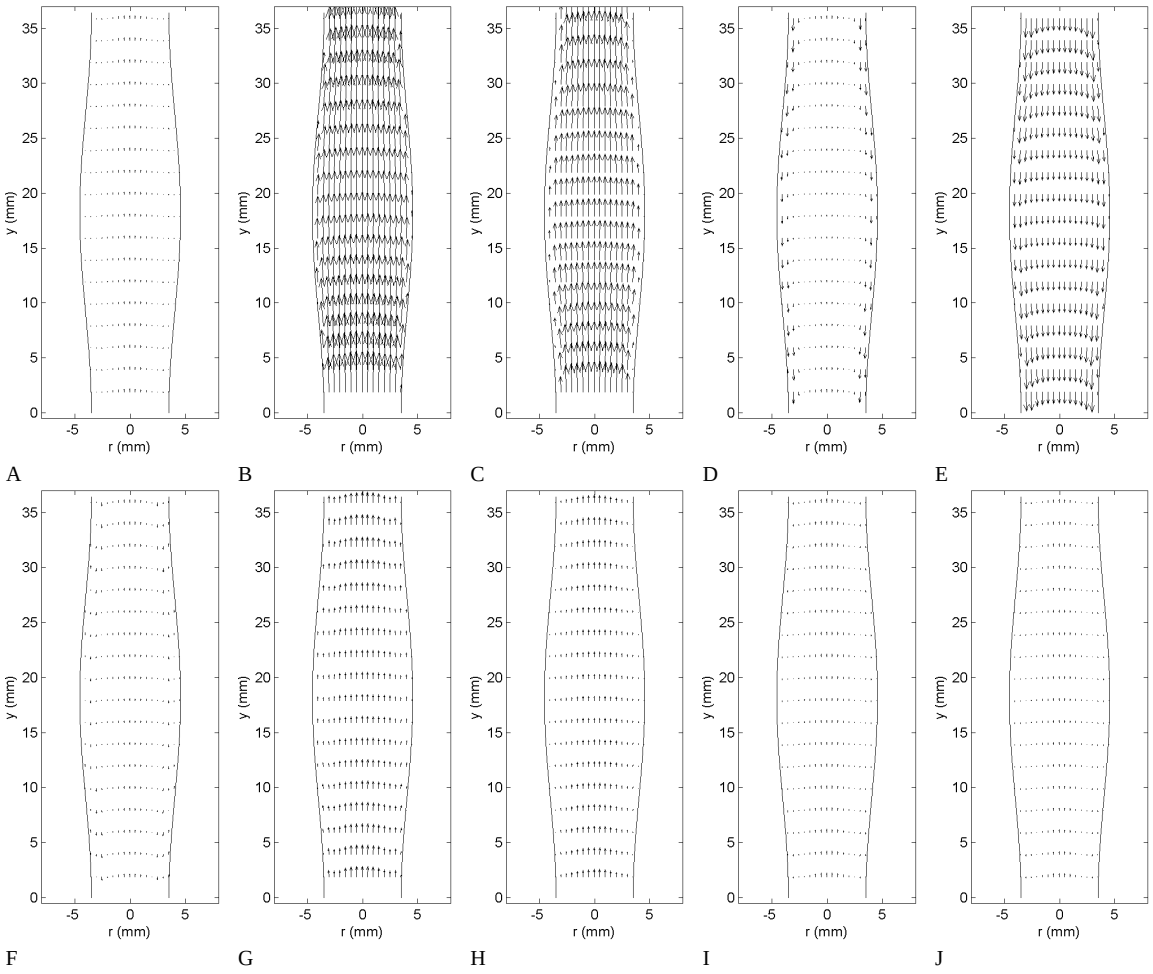

Figure 3.24: Velocity field calculated with the slowly expanding aneurysm model in an AAA with the same geometry as model 11.

From the Fourier decomposition of Q^*, one can calculate the Fourier coefficients of the pressure gradients, $G_n^*(Y^*)$ using (3.20) and then the velocity components, $v^*(Y^*, r^*, t^*)$ and $U_r^*(Y^*, r^*, t^*)$, respectively from (3.19) and (3.23). Figure 3.24 shows the velocity field across a small aneurysm calculated for a slowly expanding aneurysm model with a dilatation ratio D/d = 1.3 and aspect ratio L/d = 5.2 (geometric parameters of model 11). The flow conditions are the same as the ones used experimentally.

Wall shear stresses

At the first order, the wall shear stresses are given by:

$$WSS^*(Y^*,t^*) = -\left.\frac{\partial v^*}{\partial r^*}\right|_{r^*=R^*} = \frac{ReG_0^*}{2} + \sum_{n=1}^{\infty}\frac{ReG_n^*}{2}F(\alpha_n)e^{int^*}. \qquad (3.24)$$

Figure 3.25 shows the profile of WSS calculated for an aneurysm corresponding to model 11. Note that for this incipient AAA, the WSS profile is very similar to the one measured in model 11 (Figure 3.20 (*a*). The only slight difference is the presence of slightly higher negative WSS at the location of the incipient flow separation (*y/d* = 1) in the experimental result, followed by smaller negative values of WSS associated with the separation of the shear layer from the wall.

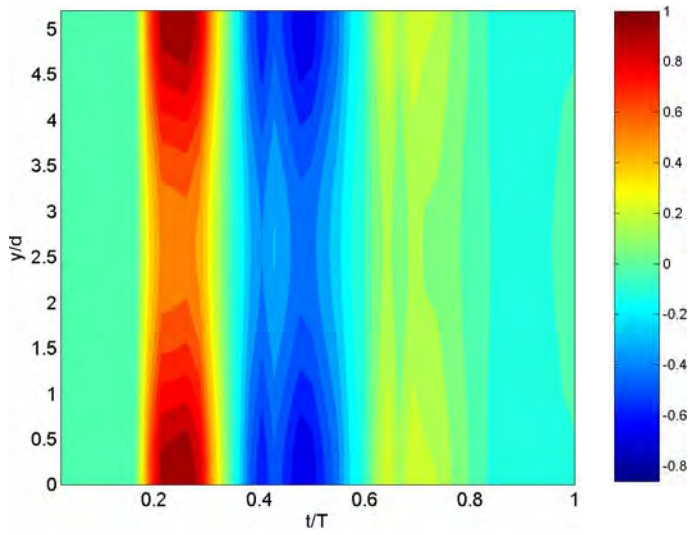

Figure 3.25: Wall shear stresses calculated with the slowly expanding aneurysm model in an AAA with the same geometry as model 11.

E. Discussion

It has been long known that the structural function of the intimal layer of the abdominal aorta (comprising the endothelial cells) is sensitive to the local hemodynamic parameters. Experiments, in which the temporal distribution of shear stresses applied to the endothelial cells could be carefully controlled, have shown that the endothelial

behavior depends not only on the magnitude of the shear stresses but also on their spatial and temporal variations. These mechanotransduction mechanisms have been postulated to play a key role in vasoregulation and in the localization of intima hyperplasia and intima lesions in regions of “disturbed flow conditions”, i.e. regions where the WSS and GWSS differ from the healthy conditions. Thus, the characterization of the changes in the WSS resulting from the enlargement of the artery is essential to understand the etiology of AAAs as well as the role that the hemodynamics plays in its progression.

Our comparative measurements of the spatial and temporal distribution of the wall shear stresses in idealized models of AAA have shown that the flow inside the aneurysm is characterized by the formation of regions of larger and lower amplitude of wall shear stresses than in the healthy vessel, as well as regions of large gradients of wall shear stresses, which are virtually non existent in the healthy case. We have found that, even at large values of the dilatation parameter, the flow remains attached to the walls during systole as a consequence of the large systolic acceleration, typical of the flow waveform in the aorta. However, we have found that, in all cases studied, the flow detaches from the wall during the deceleration period immediately following the peak systole. A large start-up vortex forms and, as it propagates through the aneurysm, secondary vortex rings develop in the associated internal shear layers. With the exception of a small zone affected by the vortex, the vessel walls are then exposed to very low and oscillating wall shear stresses. The flow detachment and the impingement of the vortex ring on the distal end of the AAA cause the formation of regions along the wall with large spatial gradients of wall shear stresses. In addition, we have shown that a region of sustained gradients of wall shear stresses always forms for aspect ratios smaller than the systolic Strouhal number, St_{syst}, when the primary vortex ring impinges on the distal end. During the diastole, the flow reversal causes a transition to a state of weak turbulence, which is subsequently dissipated over the resting period of the cardiac cycle.

	A_{-1}	A_0	A_1	A_2	A_3	A_4
	y/d = -0.4	y/d = 0	y/d = 0.75	y/d = 1.5	y/d = 2.25	y/d = 3
WSS_{max} (N/m^2)	4.5	2.8	1.2	0.8	1	3.3
WSS_{min} (N/m^2)	-2.5	-1.5	-1	-1	-2	-2
WSS_{mean} (N/m^2)	0.44	0.28	-0.09	-0.23	-0.24	0.39
WSS_{mag} (N/m^2)	1.46	0.88	0.46	0.38	0.6	1.2
OSI	0.35	0.34	0.60	0.81	0.70	0.34

Table 3.I: Comparison of different characteristic quantities, WSS_{max}, WSS_{min}, WSS_{mean}, WSS_{mag} and *OSI*, at 6 positions along the AAA in model 4 (D/d = 1.9): A_{-1} (y/d = -0.4), A_0 (y/d = 0), A_1 (y/d = 0.75), A_2 (y/d = 1.5), A_3 (y/d = 2.25) and A_4 (y/d = 3).

These changes in the flow characteristics result in very large changes in the spatial and temporal WSS distribution acting on the endothelial cells as compared to those acting on the healthy aorta (Figure 3.4). Depending on their location along the aneurysm wall, the EC experience very different patterns of WSS and GWSS as the AAA enlarges. Our measurements show the existence of two main regions, the location and size of which change as the aneurysm grows: the detached region and the reattachment region. The first region is located approximately in the proximal half of the AAA and is dominated by a large decrease in the magnitude of the WSS, as shown in Table 3.I. The WSS profile evolves from the highly pulsatile waveform measured in the healthy vessel (y/d = -0.4) to an oscillatory waveform of small amplitude (±1 N/m^2) and zero mean value near the mid-point region (y/d = 0.75) to a waveform of even smaller amplitude and negative mean at the point of maximum diameter (Figure 3.26). A peak in the GWSS occurs at the time of flow separation (Figure 3.27). However, this peak, owing to its short duration, is unlikely to have an important impact on the function of the endothelial cells.

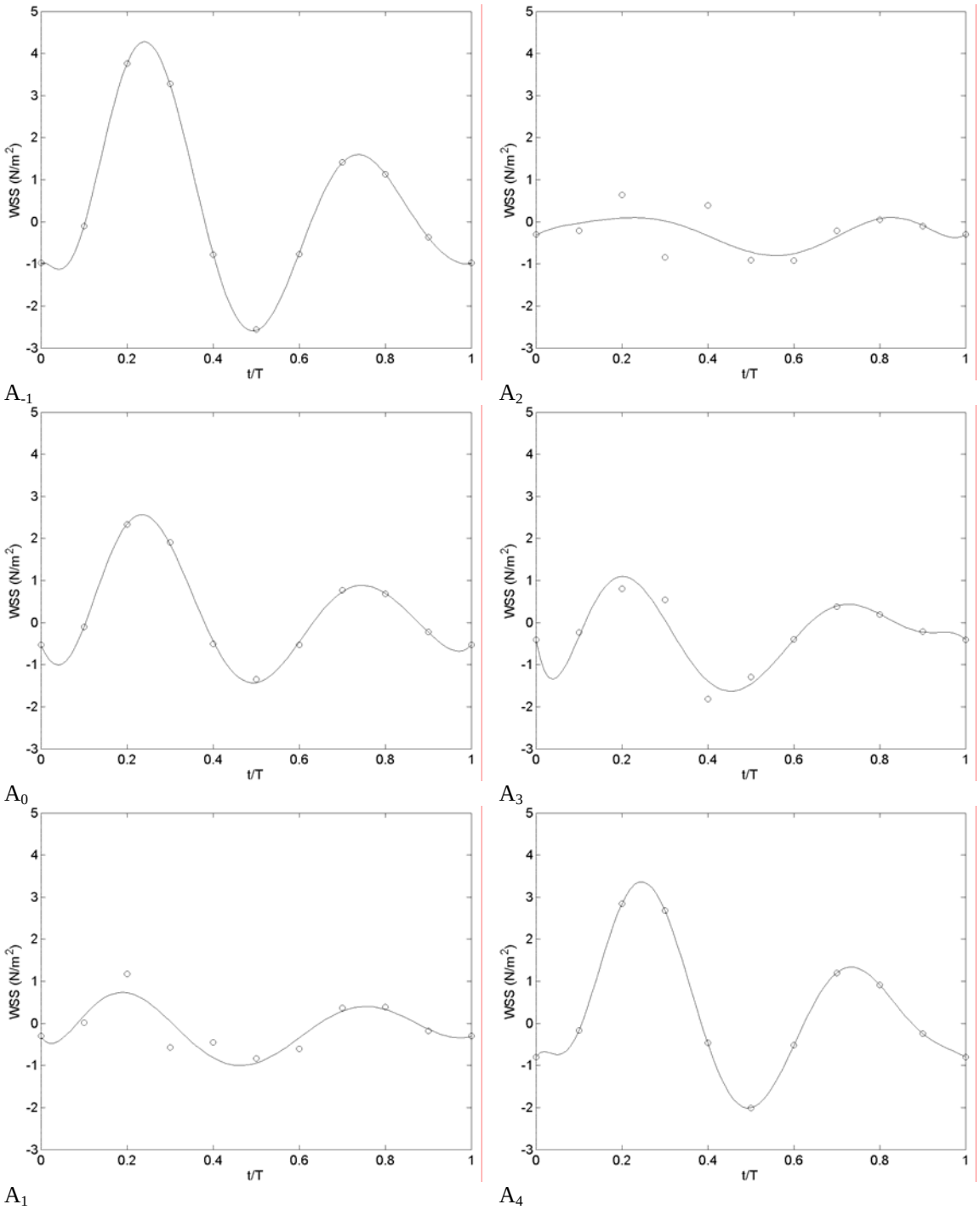

Figure 3.26: Time evolution of the wall shear stresses at a few locations inside model 4 (D/d = 1.9): A_{-1} (y/d = -0.4), A_0 (y/d = 0), A_1 (y/d = 0.75), A_2 (y/d = 1.5), A_3 (y/d = 2.25) and A_4 (y/d = 3). One can see again the similarity between the WSS profile measured in the healthy part of the tube (A_{-1}) with the analytical solution (Figure 3.4). One can then observe the extent of the changes in WSS inside the aneurysm, when comparing the profiles of WSS at location A_0, A_1, A_2 and A_3 with Figure 3.4.

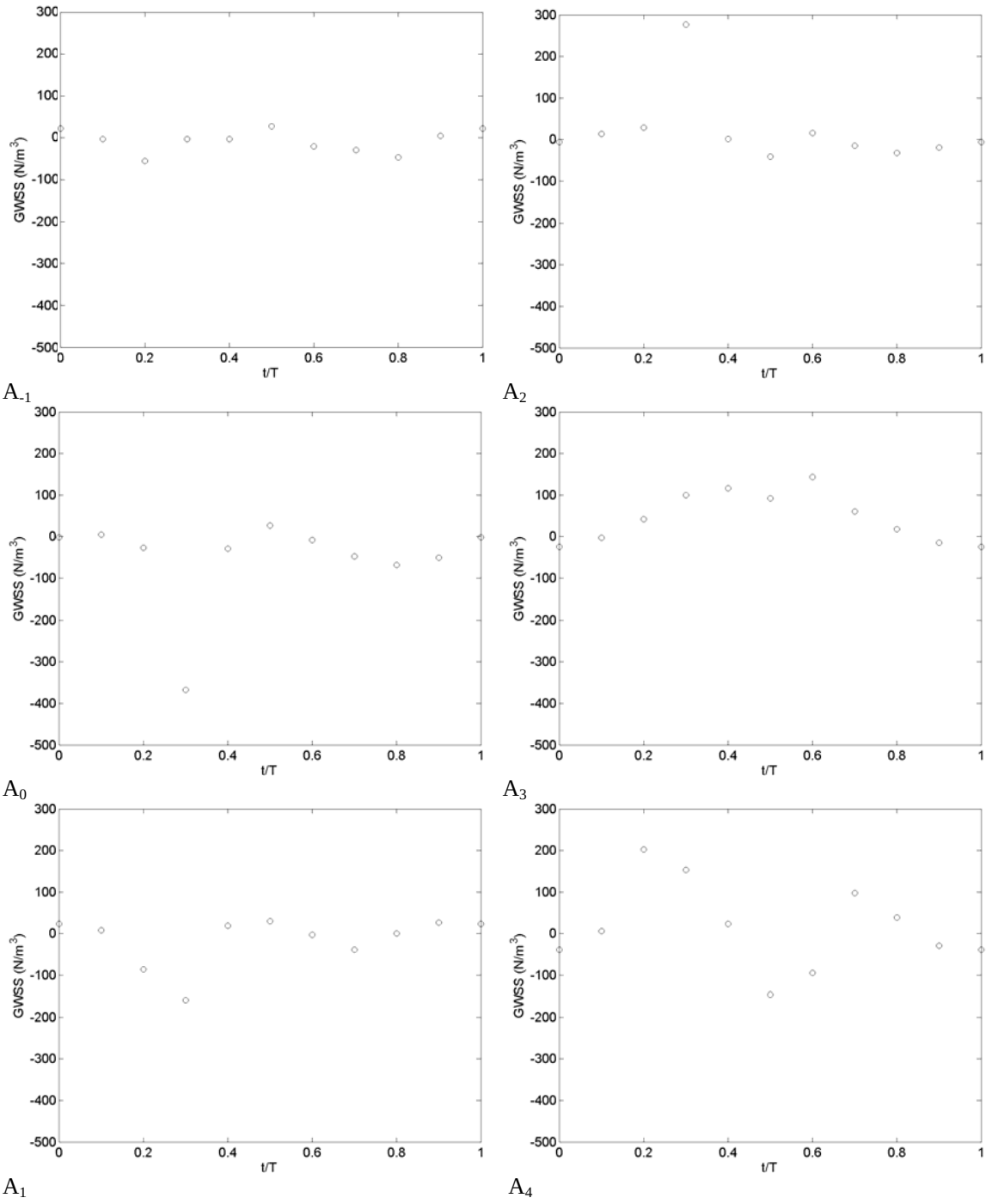

Figure 3.27: Time evolution of the gradients of wall shear stresses at a few locations inside model 4 (D/d = 1.9): A_{-1} (y/d = -0.4), A_0 (y/d = 0), A_1 (y/d = 0.75), A_2 (y/d = 1.5), A_3 (y/d = 2.25) and A_4 (y/d = 3).

In contrast, in the reattachment region, comprising nearly the second half of the AAA, we have measured sustained GWSS along with high negative WSS (around y/d =

2.25 in Figures 3.26 and 3.27). Our measurements show that this second region is subjected to GWSS over 70% of the duration of the cardiac cycle (Figure 3.27). Even the distal neck experiences strong fluctuating gradients. Furthermore, the impinging vortex ring produces high wall shear stresses in the reversed flow direction (negative values) at a late time in the cardiac cycle.

Our measurements of the spatial and temporal distribution of WSS could provide the basis for the design of endothelial cell experiments, where one could study their proliferation, altered gene expression, cell adhesion as well as the activation of the various biological processes under the realistic flow conditions encountered inside the AAA. These studies will greatly enhance our understanding of the role that the mechanical stimuli play in the etiology and progression of AAAs.

The flow changes reported here for symmetric AAA are expected to be even more pronounced in *in vivo* AAAs, since most later-stage aneurysms grow non-symmetrically, because of the presence and support of the spinal column. In the next chapter, we will show that the basic mechanisms linked to the separation of the flow at the peak systole and the roll up of the vortices are similar for non-axisymmetric AAAs. Since the vortex stretching is stronger and occurs sooner in the non-symmetric case, the turbulence is likely to be more intense. *In vivo*, the presence of the renal arteries and the lumbar curvature may also have an important effect on the flow and constitute a limitation of our study. The low distal impedance in the renal arteries leads to a suction effect that causes blood at the posterior wall to reverse and to flow back upstream into the renal arteries. Vortices are therefore formed at the entrance of the infrarenal aorta (Moore *et al.* 1992), modifying partly the flow in the parent vessel to the AAA, especially along the posterior wall. The lumbar curvature may also cause the formation of detached vortices leading to a mechanism similar to the one described here for a straight aneurysm. We can infer in both cases that the flow field may be phenomenologically similar as far as flow

separation, vortex roll up, vortex impingement on the wall as the one we conducted. Therefore, although this study was conducted in simplified models of AAA, it captures all the critical flow changes that occur once an aneurysm forms, and provides a much needed tool to analyze quantitatively the effects of the modifications in the mechanical stimuli on the formation and growth of AAAs.

F. Conclusion

We have measured systematically the effects of the growth of AAAs on the spatial and temporal distribution of the wall shear stresses. Measurements conducted in rigid symmetric AAA models have shown that flow separation occurs even at very early stages during the AAA formation ($D/d \geq 1.3$). The flow separation and the associated formation of a strong vortex ring and of internal shear layers lead to regions of perturbed stress distribution, which do not exist in a healthy abdominal aorta. For all the aneurysm models characterized by a dilatation ratio greater than 1.5, the mean WSS consistently drops from the healthy aorta value of 0.40 N/m^2 to values very close to zero, when averaged over the whole aneurysm length. However, the decrease in the average magnitude of the WSS becomes larger as the dilatation ratio increases.

In terms of WSS patterns, two main regions were identified, the detached region and the reattachment region, the size and location of which change as the aneurysm grows. On the one hand, the detached region, located in the proximal half of the aneurysm, is dominated by oscillatory wall shear stresses of very low, negative WSS_{mean}. A very large peak in the GWSS occurs at the location and time of flow separation and reaches about −600 N/m^3. But the gradients remain otherwise quite small in the proximal half.

On the other hand, the region of flow reattachment is characterized by large, sustained GWSS and large negative WSS. Most of the distal wall is subjected to GWSS throughout the cardiac cycle. The gradients fluctuate between ±400 N/m^3, the peak

values occurring upstream and downstream of the traveling vortex ring. Simultaneously, the WSS_{mean}, negative over the entire distal half of the AAA, reaches -0.4/-0.5 N/m^2 and the *OSI* index a maximum of 0.8 in the region of impact of the vortex ring.

Further studies of endothelial cell subjected to the specific spatial and temporal distribution of WSS and GWSS reported here should provide the necessary information, in order to elucidate the possible role that these disturbed patterns of WSS may have on the etiology and progression of AAAs.

Chapter 4

Effects of the loss of symmetry on the wall shear stresses in Abdominal Aortic Aneurysms

A. Introduction

Owing to their effect on the endothelial cells, wall shear stresses appear to be one of the most physiologically relevant parameter to characterize in order to improve the current understanding of the pathological processes accounting for the growth of AAAs. The evolution of the wall shear stresses during the aneurismal growth in symmetric models have been discussed in Chapter 3. This chapter is devoted to the analysis of the effects of the loss of symmetry on the flow structures and patterns of wall shear stresses. Medium to large size aneurysms (diameter > 4 cm) tend to be non-symmetric due to the presence of the vertebral column, which brings some structural support and prevent the growth in the posterior direction. It can be noticed, as detailed in the general introduction, that very few studies have involved non-symmetric models of aneurysm. None of the studies considered the changes in the wall shear stresses inside the AAA. Thus, the objective of this chapter is to quantify the changes in the spatial and temporal distribution of WSS in AAAs at progressive stages of asymmetry.

Precise measurements of the velocity field have been conducted using Particle Image Velocimetry (PIV). The evolution of the hemodynamics and WSS patterns are shown in section C. The physiological consequences of the measured patterns of WSS on the endothelial cells are detailed in section D.

B. Experimental setup

In order to study the effects of the loss of axisymmetry on the flow characteristics in AAAs, three aneurysm models have been considered, one symmetric (model 16) and 2 non-symmetric (models 17 and 18) (see Table 2.I). The three models have the same dilatation ratio (D/d = 2.3) and aspect ratio (L/d = 4.5), but an increasing asymmetry parameter (β = 0, 0.5 and 1 respectively).

PIV measurements of the instantaneous velocity field were conducted inside the two perpendicular planes (planes BB and CC) indicated in Figure 2.3 using the method described in Chapter 2.

C. Results

1. Flow characteristics in abdominal aortic aneurysms

Flow field in a symmetric AAA

Most fusiform aneurysms with a maximum diameter greater than 4 cm grow non-symmetrically. It is therefore important to understand how the flow properties change when the asymmetry parameter is increased. We shall first describe the flow in the symmetric model (model 16), which will serve as the reference case in this part of the study. The effects of the loss of symmetry will be discussed in the next sub-section. A detailed description of the evolution of the flow field in symmetric aneurysms at different stages of enlargement has already been reported in the previous chapter. For the purpose

of comparison, we discuss here the flow field in the symmetric model that has the same dilatation and aspect ratios as the non-symmetric models (D/d = 2.3, L/d = 4.5), which has not been discussed in Chapter 3. Thus, this chapter concentrates on the sole effect of increasing the asymmetric parameter. A new reference case is therefore defined in this chapter.

The velocity field has been measured in a central axial plane of the aneurysm using the PIV system with a mesh size of $0.06d \times 0.06d$. Figure 4.1 shows the instantaneous velocity field in the symmetric model (model 16) and Figure 4.2 the corresponding vorticity and stress fields at times B through E (see Appendix B for the stress calculation). The same fields are shown in Figure 4.3 phase-averaged over 6 cardiac cycles. Note that the total stress, non-dimensionalized by the peak value measured in the healthy aorta, ranges from 0 to 1, when the non-dimensionalized vorticity ranges from –1 to 1. The red scale corresponds to positive values and the blue scale to negative ones. A hyperbolic tangent color scale was chosen in order to better visualize the inner flow features, a linear scale showing only the flow dynamics at the walls.

During the accelerating phase of the systole, the flow remains attached to the walls despite the large dilatation ratio of the model (Figure 4.1 B). This is a consequence of the positive pressure gradient that dominates at the beginning of systole, as the temporal flow acceleration is larger than the convective deceleration due to the increase in the diameter inside the aneurysm. Although the flow meanders slightly, it remains laminar with the bulk of the flow almost inviscid and irrotational (Figure 4.2 B). The vorticity and shear stress are concentrated along the walls and confined to thin Stokes layers.

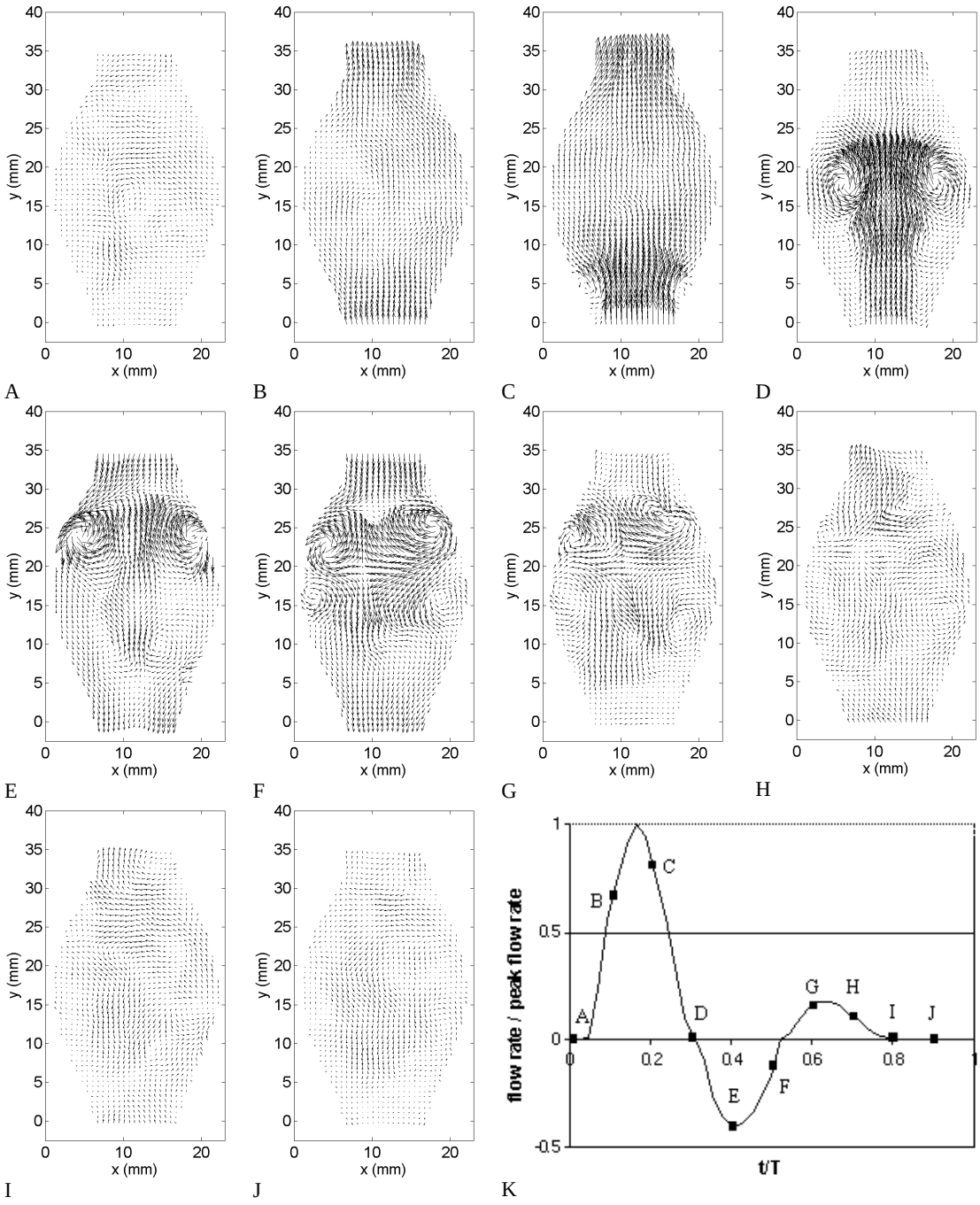

Figure 4.1: Instantaneous velocity field measured in the symmetric model (model 16) with the PIV system during one cardiac cycle.

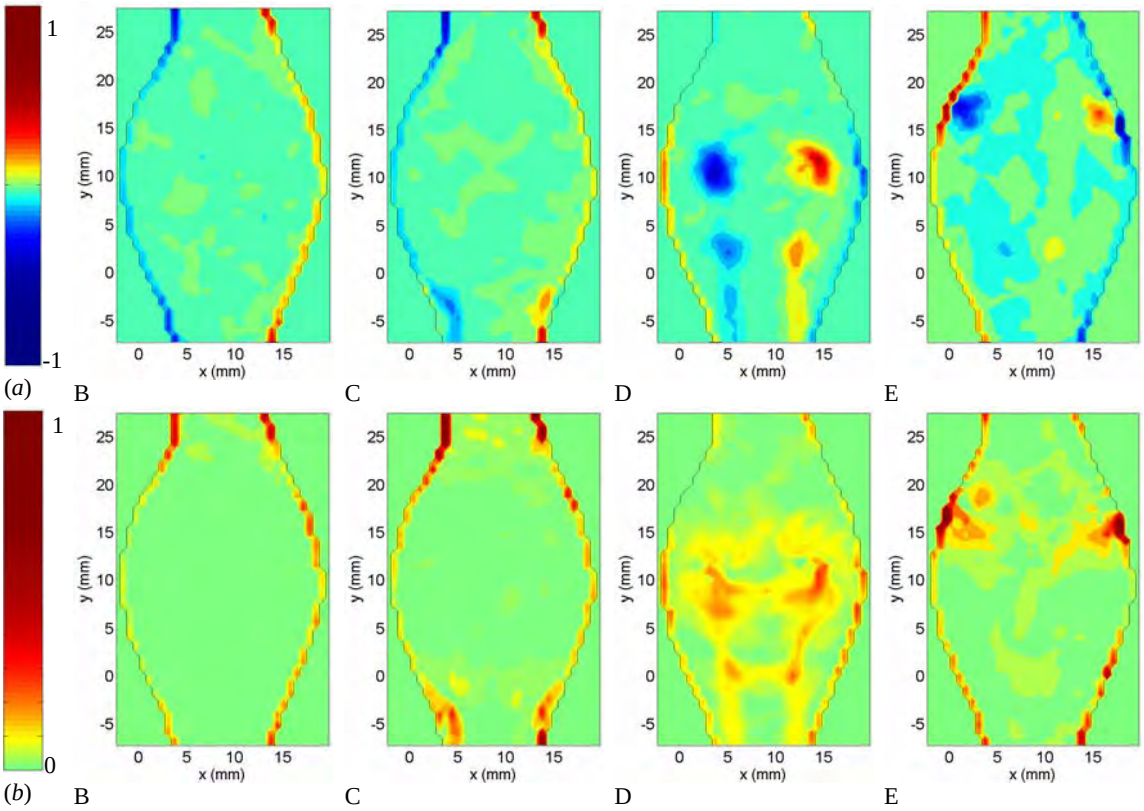

Figure 4.2: Instantaneous vorticity (*a*) and stress (*b*) fields measured in the symmetric model with the PIV system and non-dimensionalized by the peak systolic value measured in the healthy vessel.

One of the main characteristics of aneurysmal flow is its detachment from the proximal (entrance) wall in the decelerating phase of the systole (Figure 4.1 C). A strong start-up vortex ring forms proximally, while the flow remains attached to the wall downstream of it. The primary vortex ring travels along the aneurysm cavity and, as a result of the Kelvin Helmholtz instability, secondary vortices develop in the internal shear layer that is generated behind the start-up vortex (Figures 4.1 and 4.3 (*a*) D). These vortex rings can also be clearly seen in the vorticity plots (Figures 4.2 and 4.3 (*b-c*) D). The detachment of the flow from the wall leads to the formation of a large recirculating flow region that surrounds the core of the flow that is still moving forward. This region that extends over the first half of the aneurysm, is dominated by very low velocities and very small wall shear stresses as will be discussed in the next section.

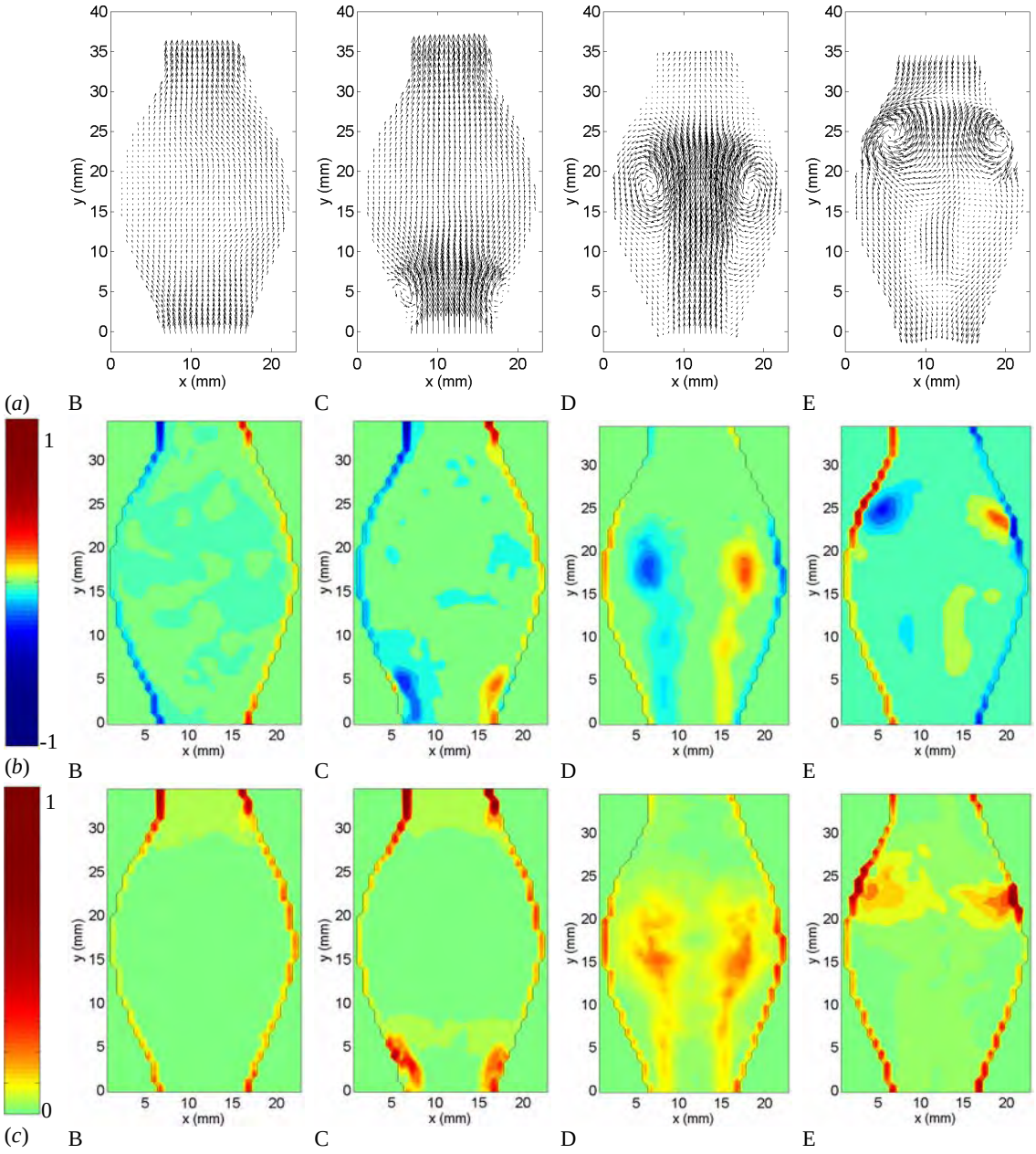

Figure 4.3: Non-dimensionalized phase-averaged velocity (*a*), vorticity (*b*) and stress (*c*) fields measured in the symmetric model with the PIV system.

In the symmetric model, the ratio *l/d*, where *l* is the maximum distance available to the vortex ring to travel inside the aneurysm, is equal to 2.5 and is therefore less than the systolic Strouhal number (St_{syst} = 3), which is the controlling parameter of the vortex shedding (Chapter 3). This explains why the vortex ring impinges on the distal neck of

the aneurysm, generating very high negative shear stresses at the point of impact (time E in Figures 4.1, 4.2 and 4.3).

It should be noted that even in this symmetric geometry, a loss in the symmetry of the flow occurs as the primary vortex ring impinges on the distal wall (Figure 4.1 E). The flow becomes even more disorganized at time F, when the Stokes layers roll up into a counter-rotating vortex ring upstream of the primary ring (Figure 4.1 F). The intensity of these weakly turbulent motions decreases in the resting portion of the cardiac cycle due to viscous dissipation (Figure 4.1 G-J). The flow almost returns to a stagnant flow field at the end of the cardiac cycle (Figure 4.1 J). Some residual stirring of the flow still remains at the end of the cycle and causes a small cycle-to-cycle variation in the measurements.

Flow field in a non-symmetric AAA

a. Measurements in the symmetric plane. The flow field was measured in the symmetric plane (plane BB in Figure 2.3 (*b*)) in the partially (β = 0.5) and fully (β = 1) non-symmetric models, using the PIV system. The phase-averaged velocity, vorticity and stress fields are respectively shown in Figures 4.4 and 4.5 at times B to F.

During the accelerating phase of the systole, no appreciable qualitative difference can be observed between the flow in the non-symmetric and symmetric models: the flow stays attached to the walls, since the controlling parameter, the aspect ratio, is identical for all the models (Figures 4.4 B and 4.5 B). The effect of the non-symmetry becomes apparent, as the flow decelerates. Although a start-up vortex still forms when β = 0.5 (model 17) followed by an internal shear layer (Figure 4.4 C), its progression is impaired by the three-dimensional patterns of the flow at times D and E. Even though the vortex ring is too weak to impinge on the distal wall, as would occur in the symmetric case, it persists through the diastole, before being dissipated in the resting period of the cardiac

cycle. The Stokes layer is therefore dominated by low vorticity and shear stresses throughout the diastole (Figure 4.4 D-E).

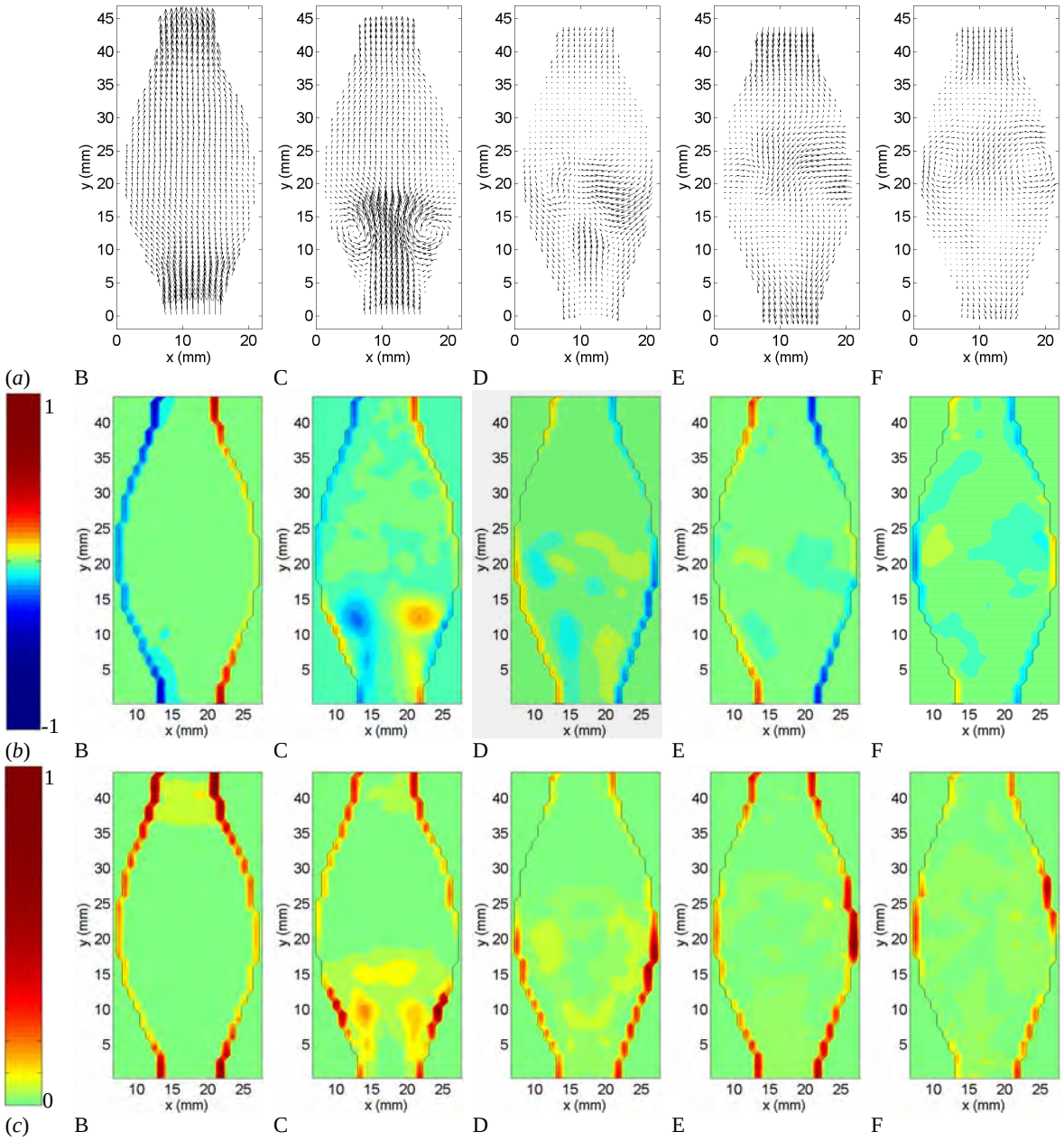

Figure 4.4: Non-dimensionalized phase-averaged velocity (*a*), vorticity (*b*) and stress (*c*) fields measured in the symmetric plane in model 17 (β = 0.5) with the PIV system.

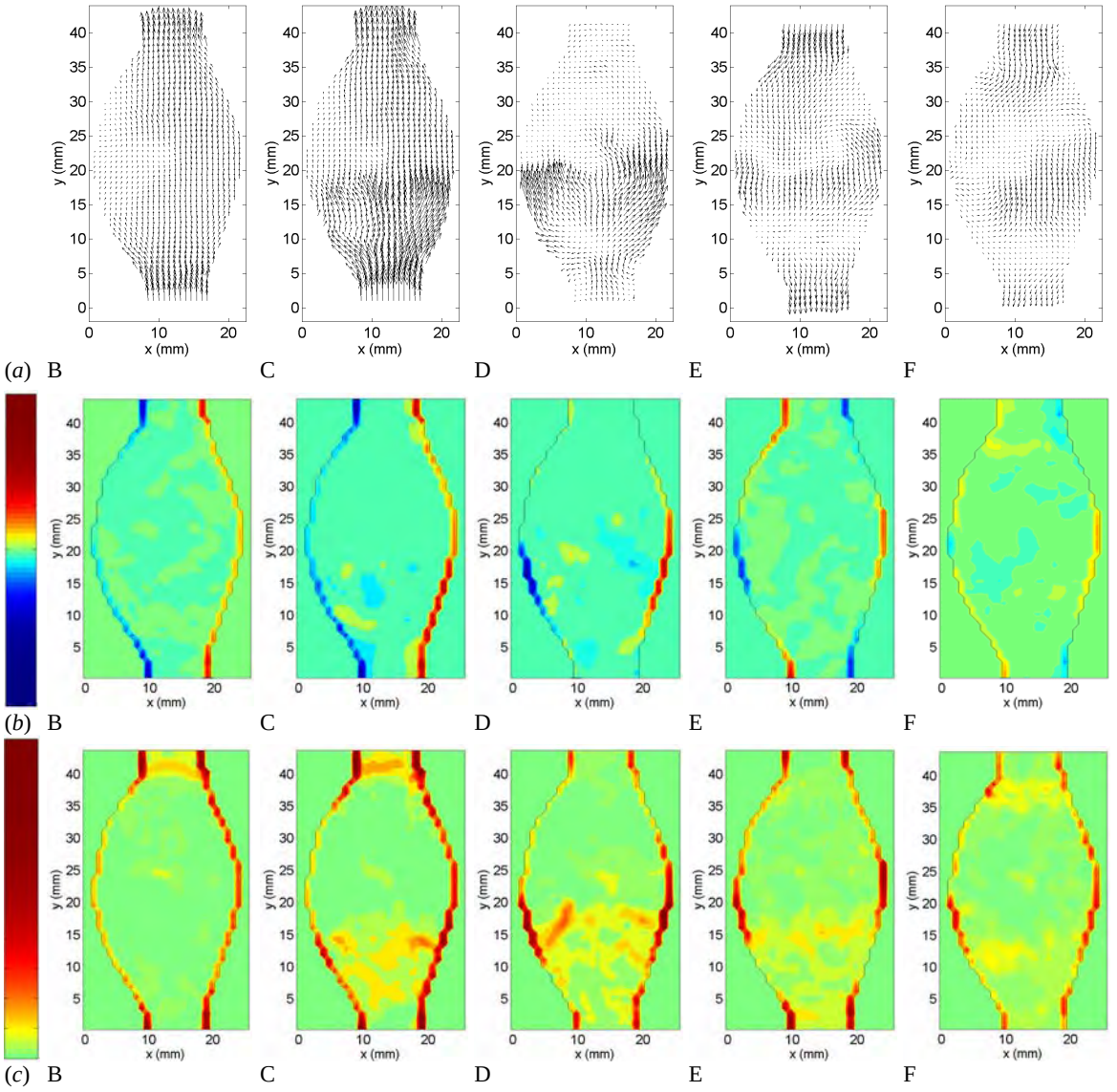

Figure 4.5: Non-dimensionalized phase-averaged velocity (*a*), vorticity (*b*) and stress (*c*) fields measured in the symmetric plane in model 18 (β = 1) with the PIV system.

On the contrary, none of the flow features encountered in symmetric aneurysms (formation of a large start-up vortex ring and of internal shear layers, impingement of the vortex ring on the distal neck, breakdown of the axisymmetry in the diastole, etc.) are seen for large asymmetry parameters, as shown in Figure 4.5 for β = 1 (model 18). We can see that, as the asymmetry parameter β increases to large values, the flow features are dominated by the very massive detachment that occurs in the non-symmetric plane.

b. Measurements in the non-symmetric plane. The instantaneous flow field measured in the non-symmetric mid-plane (plane CC on Figure 2.3 (*b*)) is shown in Figure 4.6 for β = 0.5 (model 17) and in Figure 4.7 for β = 1 (model 18) at times B to F, along with the vorticity and stress fields. One can notice that, for β = 1, the flow is no longer attached to the anterior wall during the systolic acceleration (Figure 4.7 B), when the flow is still attached for β = 0.5 (Figure 4.6 B). For the flow waveform used in this experiment, the limiting dilatation ratio that guarantees no flow separation during the acceleration therefore lies between 3.1 and 4.5, which are, respectively, the equivalent dilatation ratios of the anterior wall in non-symmetric models 17 (β = 0.5) and 18 (β = 1).

The effect of the non-symmetry of the models is even more pronounced from the peak systole (time C) onwards, as the flow massively detaches: in the non-symmetric plane, the roll-up of the boundary layer into a strong vortex occurs only from the anterior proximal neck, while the flow remains attached to the posterior wall (see time C on Figure 4.6 for β = 0.5 and time B on Figure 4.7 for β = 1). This leads to the formation of a hairpin vortex. Flow separation occurs sooner as the asymmetry parameter increases. A small phase lag can be observed between the three sets of experiments. The points A, B, C, etc. are indicative of the time position in the cycle but due to the framing rate of our measurements, they do not correspond to exact times along the cardiac cycle.

After being formed, the hairpin vortex moves towards the posterior wall, inducing very high shear stresses at the location where it hits the wall (time D on Figure 4.6 for β = 0.5 and time C on Figure 4.7 for β = 1). The flow is seen to separate briefly from the wall downstream of the point of impact (Figure 4.7 C). For both models, it can be noted that the vortex is sufficiently strong to persist throughout the cardiac cycle. It is only washed out of the aneurysmal cavity at the systolic acceleration of the following cycle. It is this vortex that dominates the flow features in the case of β = 1, accounting for the disrupted flow patterns in the symmetric plane.

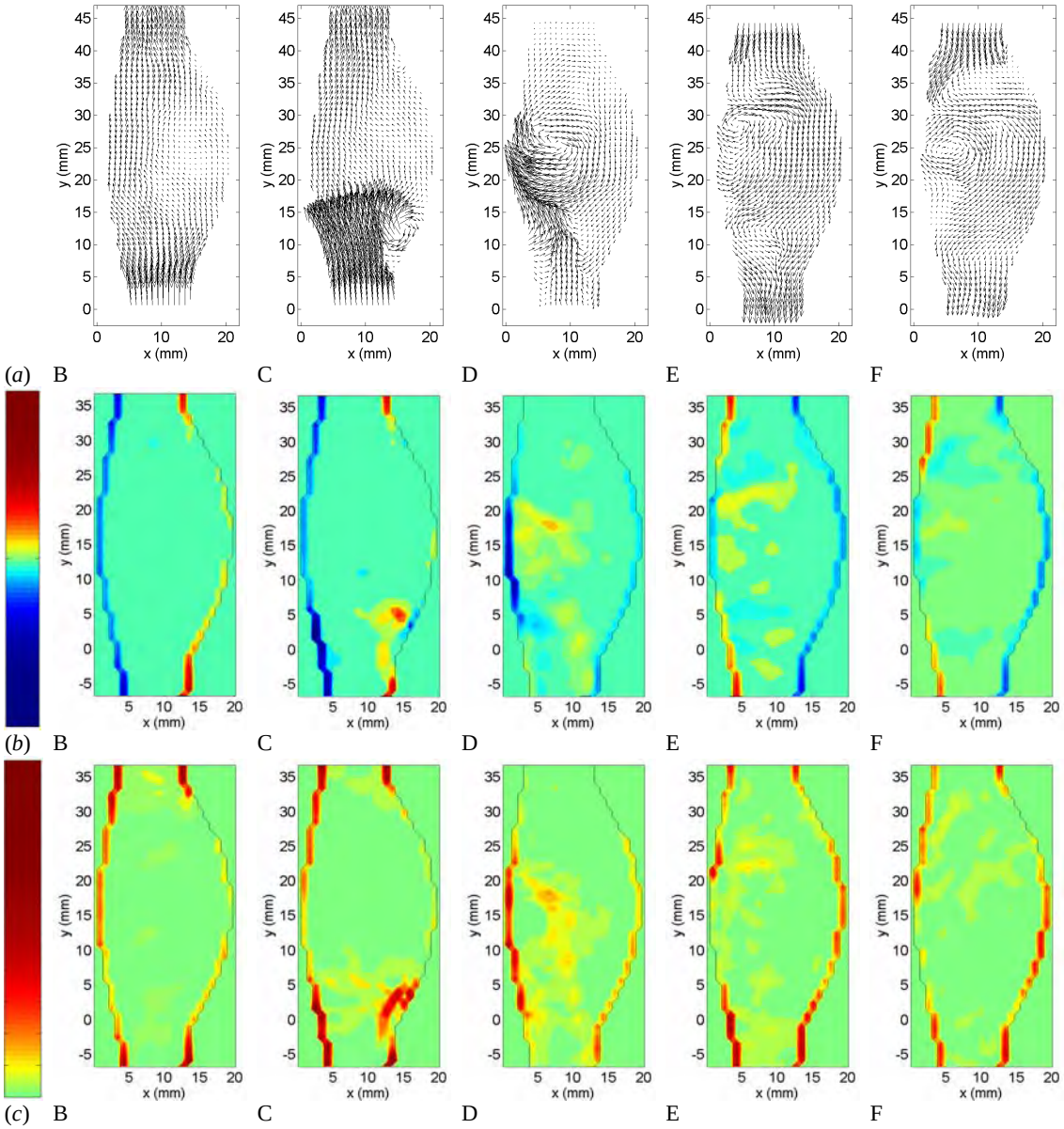

Figure 4.6: Non-dimensionalized instantaneous velocity (*a*), vorticity (*b*) and stress (*c*) fields measured in the non-symmetric plane in model 17 (β = 0.5) with the PIV system.

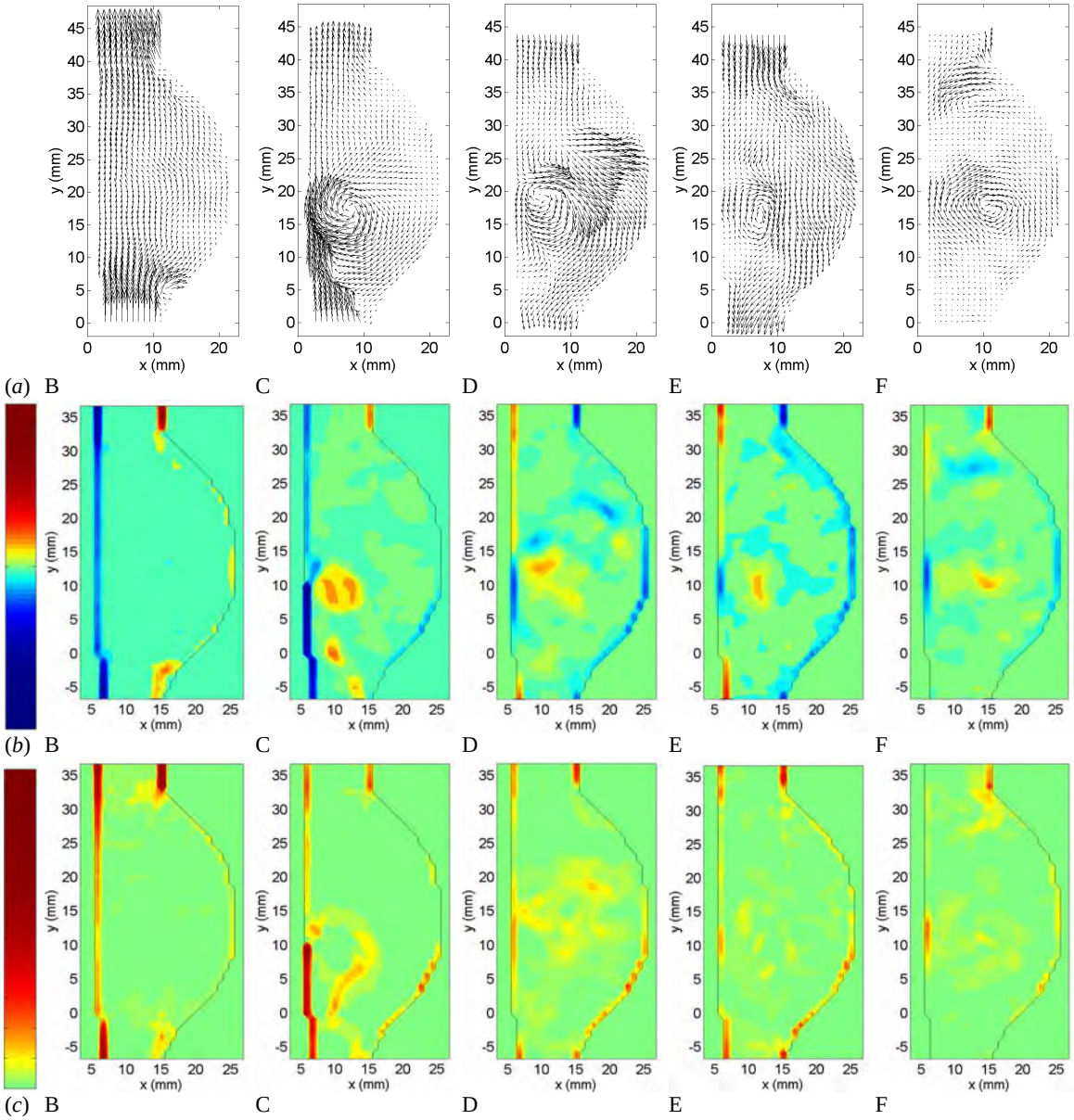

Figure 4.7: Non-dimensionalized instantaneous velocity (*a*), vorticity (*b*) and stress (*c*) fields measured in the non-symmetric plane in model 18 (β = 1) with the PIV system.

One very important difference of the flow in non-symmetric geometries as compared to the symmetric case is the formation of a stagnation point along the bulged wall, as the detached flow impinges on the anterior wall. Our measurements show that this feature is enhanced as the asymmetry parameter is increased. The formation of a stagnation point is

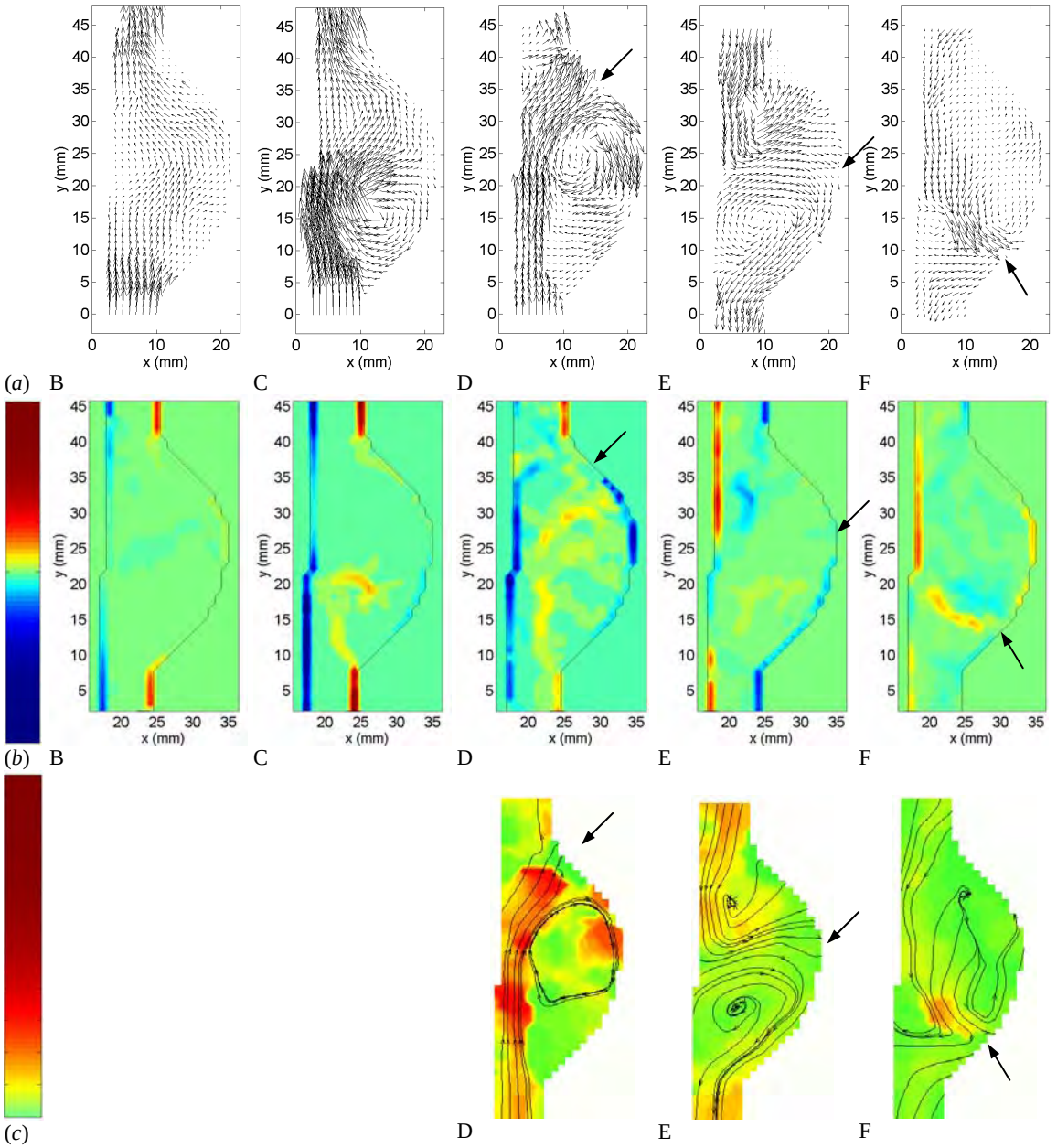

Figure 4.8: (*a*) Instantaneous velocity field measured in model 18 (β = 1) with the same flow waveform but increased flow conditions ($\overline{Re}_m$ = 540, $\overline{Re}_p$ = 4550), (*b*) corresponding non-dimensionalized instantaneous vorticity field, (*c*) streamlines superimposed on the plot of the non-dimensionalized instantaneous velocity magnitude. The arrow indicated the location of the stagnation point.

only incipient for β = 0.5 (Figure 4.6 F), but it is more pronounced for β = 1 (Figure 4.7 D and E). The stagnation point, characterized by a large spike in pressure and spatial

gradients of wall shear stress appears towards the point of maximum diameter, damaging the wall at what seems to be its weakest point. Increasing the Reynolds number strengthens the stagnation point. At high Reynolds numbers, the stagnation point is observed to form distally and then sweep the entire anterior wall (Figure 4.8).

2. Patterns of WSS and GWSS in AAAs

WSS in a symmetric AAA

Detailed results of the spatial and temporal distribution of WSS in different symmetric aneurysms has already been described (Chapter 3). In order to ascertain the effects of the loss of symmetry on the WSS, we briefly discuss here the most relevant features. With respect to the WSS and GWSS, the two dramatic events in the case of a symmetric aneurysm, are the formation of a start-up vortex ring and its later impingement on the distal neck.

The phase-averaged WSS, measured in the symmetric model (model 16) and non-dimensionalized by the peak WSS of the healthy vessel, are shown in Figure 4.9 (*a*). The corresponding gradients of the phase-averaged WSS are given in Figure 4.9 (*b*). The convention followed is to assign a negative value to the WSS in regions of reversed flow. During the systolic acceleration (t/T = 0.2), the WSS are much smaller along the aneurysm wall than in the parent vessel. Since the flow stays attached to the walls at this stage, the WSS evolve similarly to the velocity, which inversely scales with the diameter in order to conserve mass. The subsequent large decrease in WSS that occurs at the aneurysm necks induces very strong gradients of WSS at these locations (y/d = 0 and 4.6 at times t/T = 0.2 and 0.3). Some level of GWSS persists at the necks throughout the cardiac cycle. The flow detachment from the wall at t/T = 0.3 gives rise to a region of large negative WSS around y/d = 0.6-0.8. The formation of the strong vortex ring also leads to the generation of very large GWSS upstream and downstream of it. The impact

of the vortex ring on the distal wall at t/T = 0.5 is associated with the formation of very large negative WSS at y/d = 3.6 and high GWSS around this point.

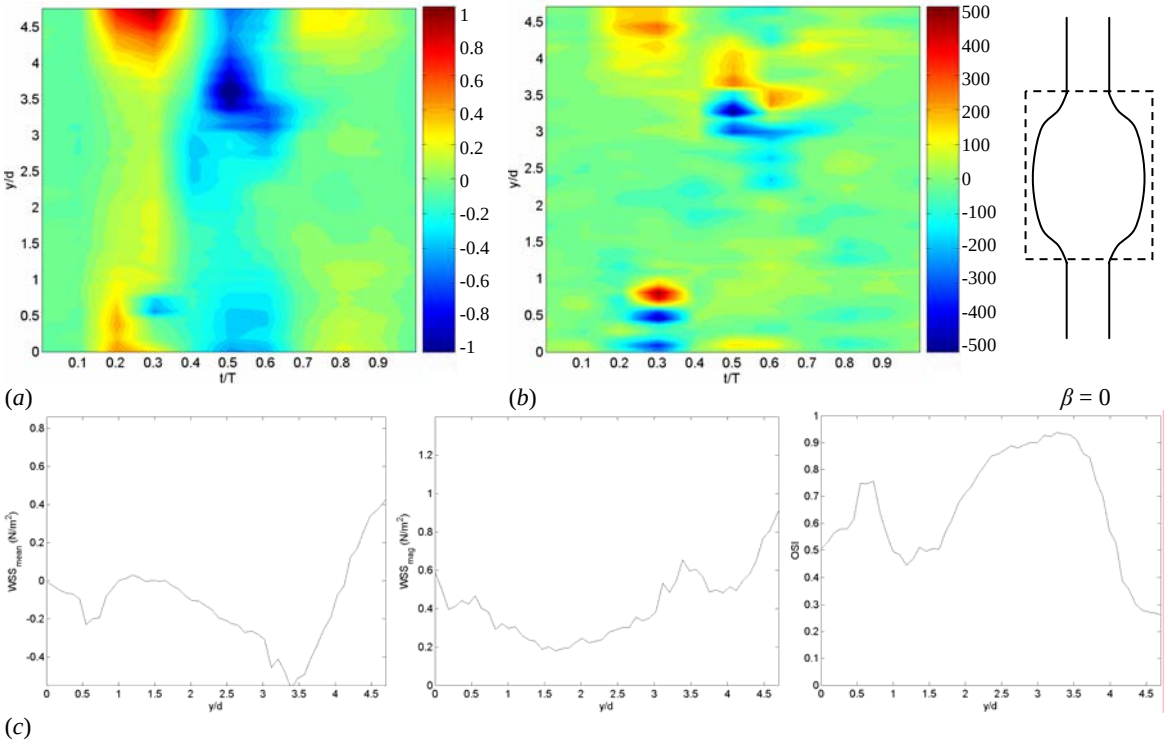

Figure 4.9: (*a*) Phase-averaged WSS measured in the symmetric model (model 16), non-dimensionalized by the peak WSS of the healthy vessel. (*b*) Gradient of the phase-averaged WSS in N/m^3. (*c*) Mean WSS, magnitude of the WSS and oscillating shear index.

The evolution of the time-averaged WSS, WSS_{mean}, magnitude of the WSS, WSS_{mag}, and of the oscillatory shear index, *OSI* (see definitions in the previous chapter), is shown in Figure 4.9 (*c*). The formation of an AAA has a very important effect on all these parameters. In the symmetric case, the WSS_{mean} drops from 0.35 N/m^2 in a healthy abdominal aorta to an average of -0.11 N/m^2 in the aneurysm, the WSS_{mag} decreases from 1.2-1.3 N/m^2 to an average of 0.42 N/m^2 and the OSI index increases from 0.3 to an average of 0.65. In conclusion, the aneurysm walls are subjected to WSS of low magnitude and the flow inside the AAA is mainly reversed, as indicated by the WSS_{mean} and the *OSI* index.

More specifically, the flow separation from the wall leads to a region, where the WSS are very low and oscillating (OSI ~ 0.5) through most of the cardiac cycle (y/d = 0.7-2). The distal half of the aneurysm is dominated by the presence of the vortex ring, which induces reversed flow conditions, as indicated by the OSI index being well above 0.5. The peak (OSI = 0.93) occurs at the location of the vortex ring impingement on the wall, where the WSS_{mean} drops to very high negative values (-0.55 N/m^2). The distal half is also subjected to sustained gradients of WSS.

WSS in a non-symmetric AAA

a. Measurements in the symmetric plane. The measurements of the phase-averaged WSS and GWSS, along with the evolution of the WSS_{mean}, WSS_{mag} and OSI index, are shown in Figures 4.10 and 4.11, taken in the symmetric plane of models 17 (β = 0.5) and 18 (β = 1), respectively. As discussed in the previous section, the flow in the symmetric plane of model 17 retains most of the characteristics seen in an axisymmetric model. The WSS patterns are likewise characterized by a marked decrease during systole, which leads to GWSS at the necks. The magnitude of the stimulation on the wall is very comparable, with an average WSS_{mag} of 0.40 N/m^2. The formation of the large vortex induces a zone of negative WSS and higher GWSS around it, although the intensity of the GWSS is three times lower than in the axisymmetric model. The main difference with the symmetric model comes from the trajectory of the vortex. For β = 0.5, the vortex stays confined to the proximal half and does not impinge on the distal wall. Since it is not disturbed by the vortex, the distal half of the AAA is dominated by a WSS_{mean} very close to the healthy value (~ 0.3 N/m^2). Contrary to the symmetric model, the WSS_{mean} is then on average positive inside the aneurysm ($\overline{WSS}_{mean}$ = 0.13 N/m^2) and the average OSI index remains in the healthy range ($\overline{OSI}$ = 0.36).

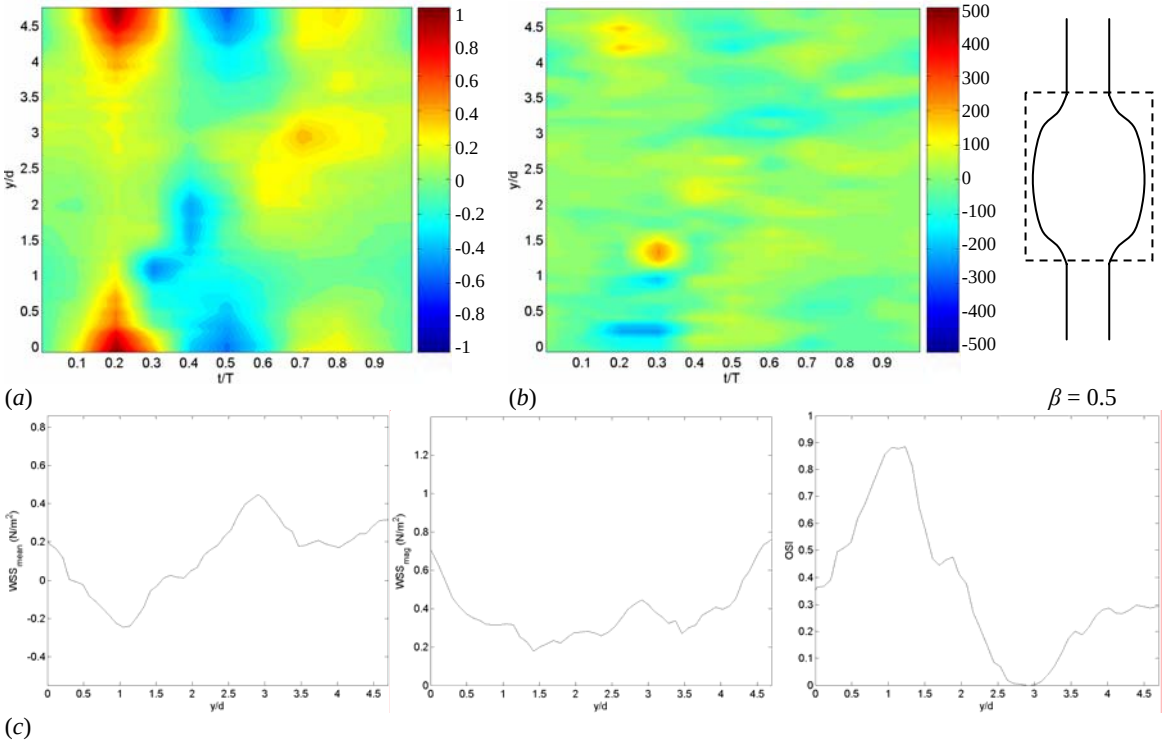

Figure 4.10: (*a*) Phase-averaged WSS measured in the symmetric plane in model 17 (β = 0.5), non-dimensionalized by the peak WSS of the healthy vessel. (*b*) Gradient of the phase-averaged WSS in N/m^3. (*c*) Mean WSS, magnitude of the WSS and oscillating shear index.

In the case of β = 1, however, the proximal walls are subjected to positive WSS in the decelerating portion of the systole, with values close to the ones measured in a healthy vessel. This explains why the WSS_{mean} does not decrease sharply in the proximal half and remains around 0.2 N/m^2. The distal half is dominated by negative WSS of very small magnitude (WSS_{mag} ~ 0.2 N/m^2), situation that corresponds to a high value of the *OSI* index (~ 0.8). GWSS form at the transition between the 2 regions of the AAA in the late systole (y/d = 2.2 at t/T = 0.4).

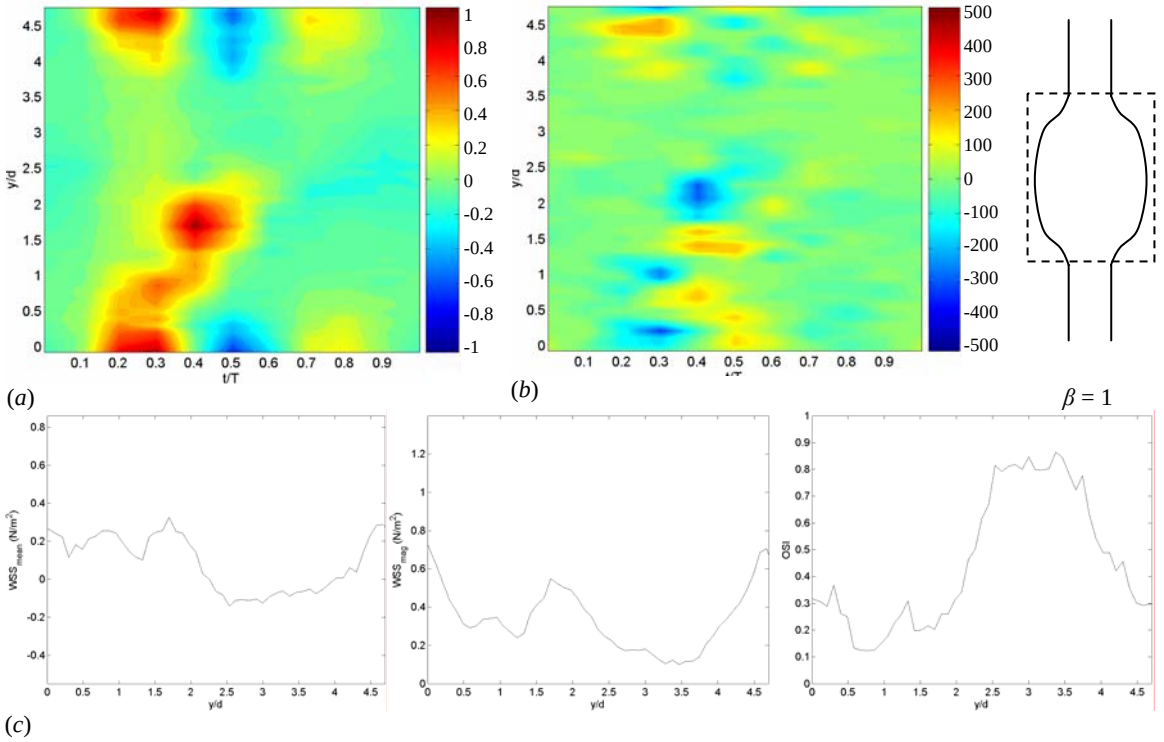

Figure 4.11: (*a*) Phase-averaged WSS measured in the symmetric plane in model 18 (β = 1), non-dimensionalized by the peak WSS of the healthy vessel. (*b*) Gradient of the phase-averaged WSS in N/m^3. (*c*) Mean WSS, magnitude of the WSS and oscillating shear index.

b. Measurements in the non-symmetric plane. The WSS and GWSS measured in the non-symmetric plane of models 17 (β = 0.5) and 18 (β = 1) are shown in Figures 4.12 and 4.13 for the posterior wall and in Figures 4.14 and 4.15 for the anterior wall.

The peculiarity along the posterior wall is the persistence of a mean forward flow in the non-symmetric models. With high WSS acting on the proximal half of the AAA (~ 0.46 N/m^2 on average), the *OSI* index even drops to a zero value (forward flow) in the middle portion of the wall. The average *OSI* index is consequently much lower along the posterior wall than in the healthy vessel ($\overline{OSI}$ = 0.20), when the average WSS_{mean} is of the same order of magnitude ($\overline{WSS}_{mean}$ = 0.37 N/m^2). The average WSS_{mag} is higher as well than anywhere else in the aneurysm, but at 0.58 N/m^2, it remains still far from the healthy value. A positive peak in WSS occurs at the location, where the vortex, formed at

the anterior proximal neck touches the posterior wall. At this location (at y/d = 2.5 and t/T = 0.4 for β = 0.5 and y/d = 1.8 and t/T = 0.3 for β = 1), the vortex induces a very high value of WSS_{mean} and WSS_{mag} as well as high gradients of WSS. Downstream of the point of impact, the WSS progressively match with the healthy vessel values.

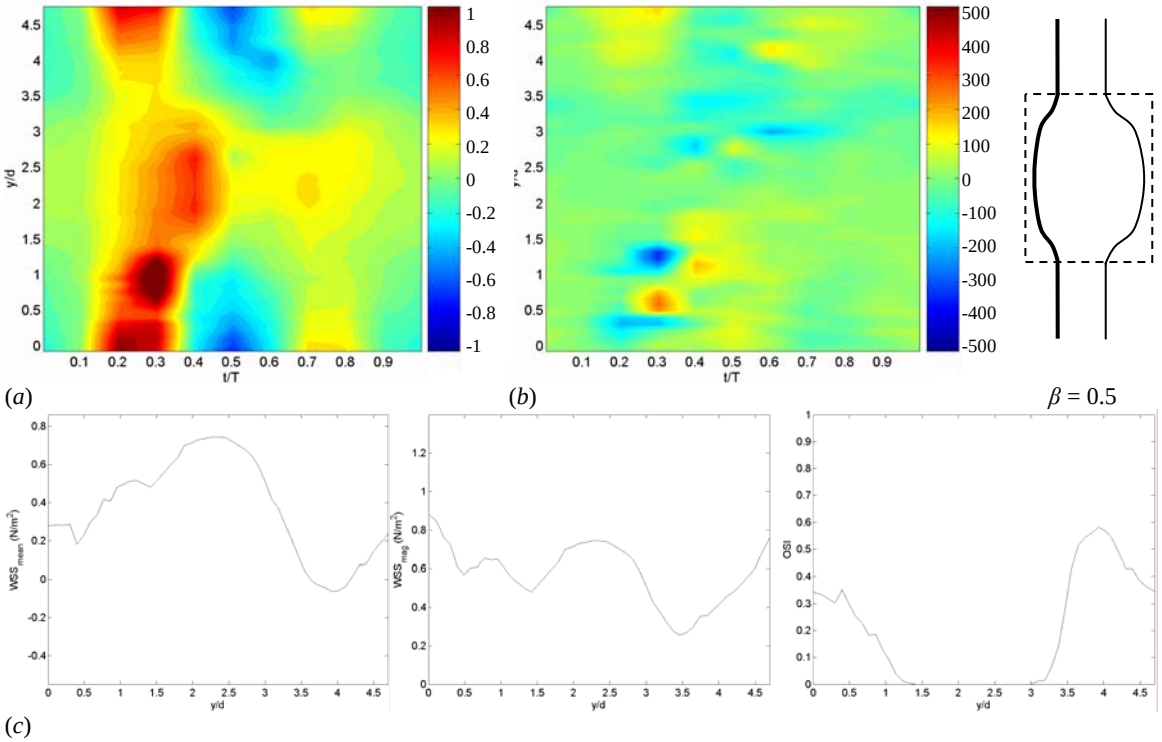

Figure 4.12: (*a*) Phase-averaged WSS measured in the non-symmetric plane in model 17 (β = 0.5) along the posterior wall, non-dimensionalized by the peak WSS of the healthy vessel. (*b*) Gradient of the phase-averaged WSS in N/m^3. (*c*) Mean WSS, magnitude of the WSS and oscillating shear index.

While the posterior wall is mainly stimulated by positive WSS, the anterior wall is dominated by an almost fully reversed flow with very low WSS throughout the cardiac cycle. The particularity of the anterior wall is the presence of a very large region of slowly recirculating flow that extends over most of the wall. This region, characterized by an *OSI* index of 1 (fully reversed flow) is dominated by negative WSS of very low magnitude ($\overline{WSS}_{mean}$ = -0.20 N/m^2, $\overline{WSS}_{mag}$ = 0.20 N/m^2). The very marked decrease in the WSS at the necks generates strong gradients of WSS, twice as large as the ones

measured in the axisymmetric model. Note that the proximal neck is not resolved on the measurements in model 18 (β = 1).

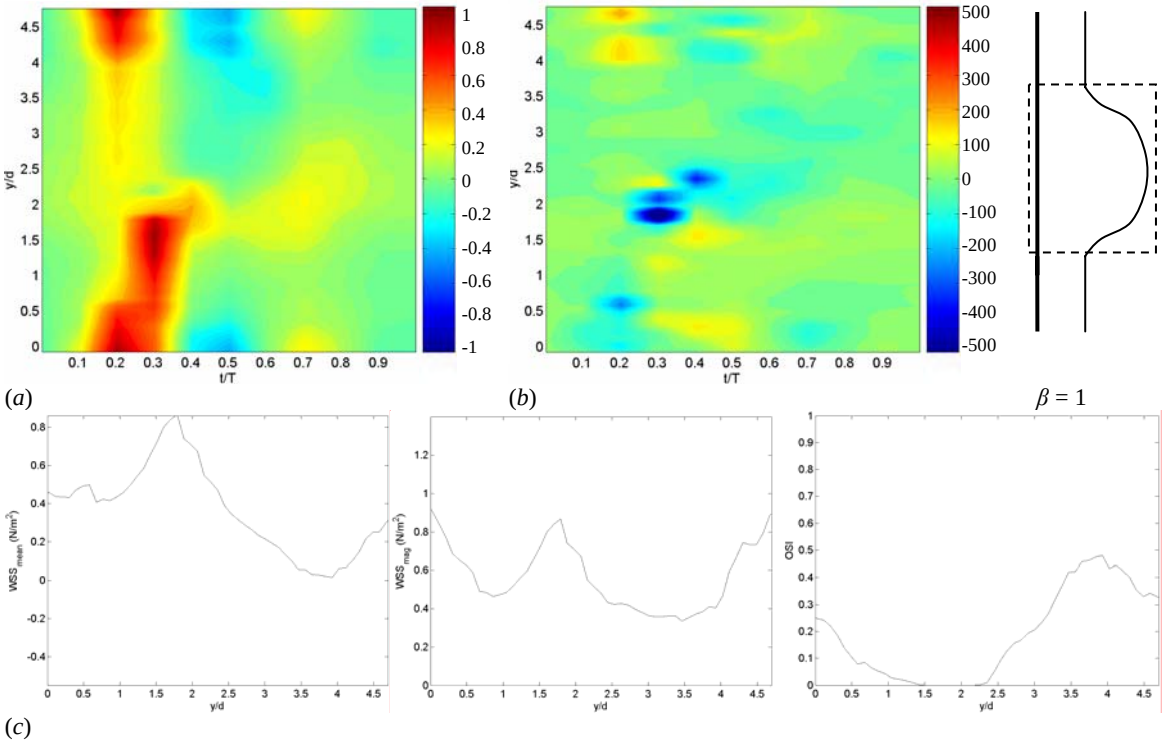

Figure 4.13: (*a*) Phase-averaged WSS measured in the non-symmetric plane in model 18 (β = 1) along the posterior wall, non-dimensionalized by the peak WSS of the healthy vessel. (*b*) Gradient of the phase-averaged WSS in N/m^3. (*c*) Mean WSS, magnitude of the WSS and oscillating shear index.

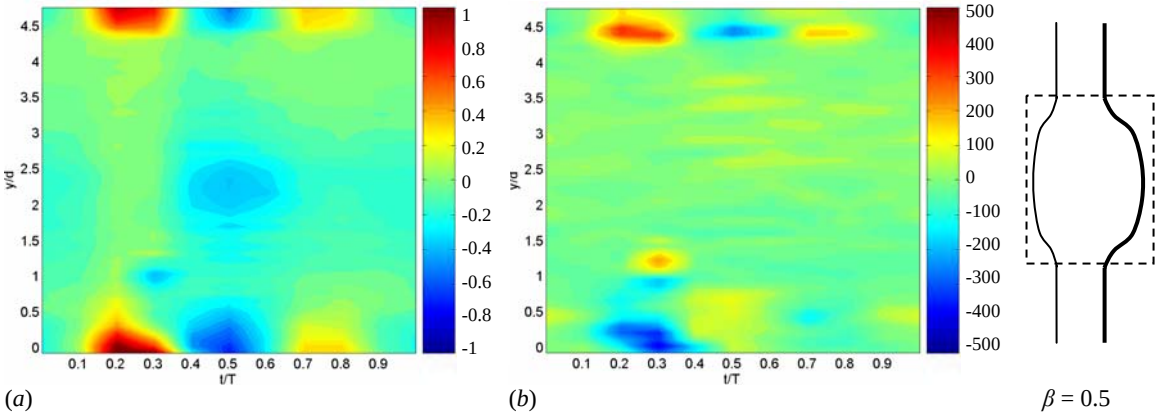

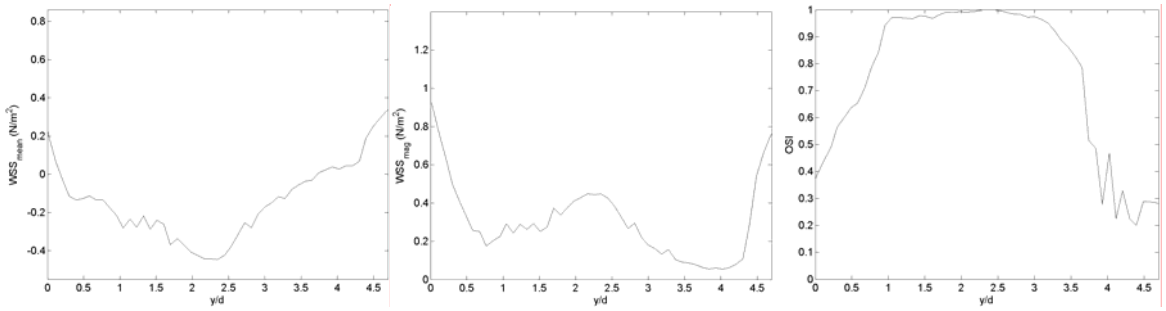

(*c*)

Figure 4.14: (*a*) Phase-averaged WSS measured in the non-symmetric plane in model 17 (β = 0.5) along the anterior wall, non-dimensionalized by the peak WSS of the healthy vessel. (*b*) Gradient of the phase-averaged WSS in N/m^3. (*c*) Mean WSS, magnitude of the WSS and oscillating shear index.

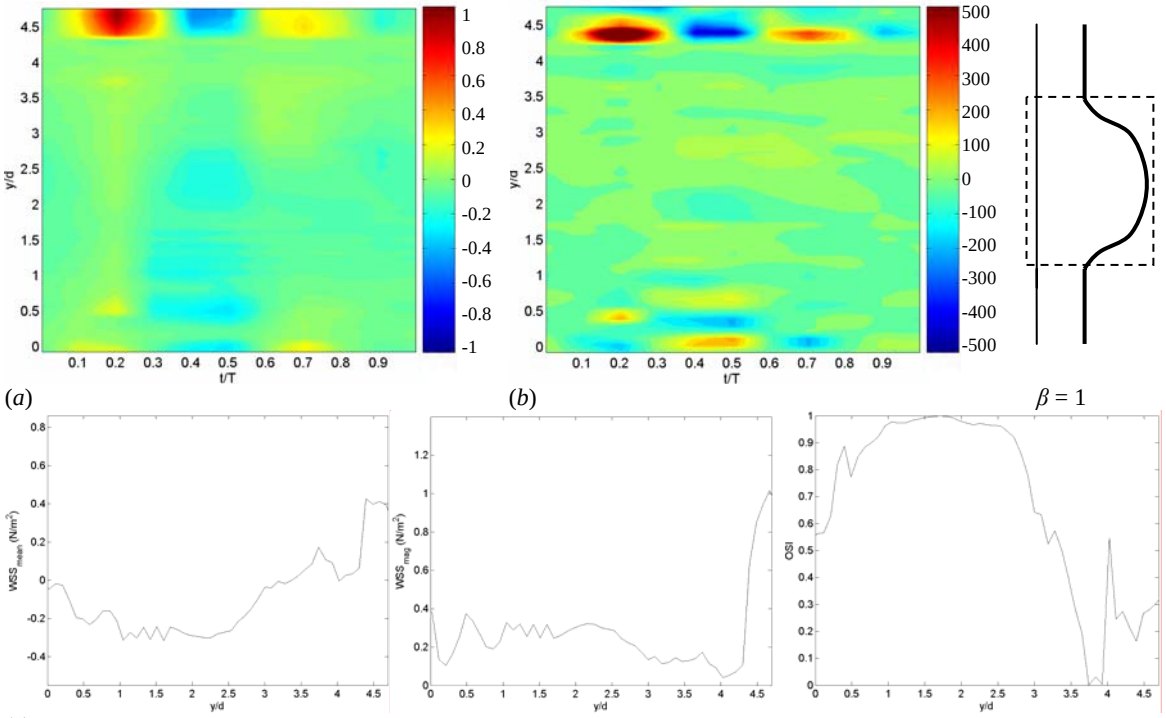

(*a*) (*b*) β = 1

(*c*)

Figure 4.15: (*a*) Phase-averaged WSS measured in the non-symmetric plane in model 18 (β = 1) along the anterior wall, non-dimensionalized by the peak WSS of the healthy vessel. (*b*) Gradient of the phase-averaged WSS in N/m^3. (*c*) Mean WSS, magnitude of the WSS and oscillating shear index.

B 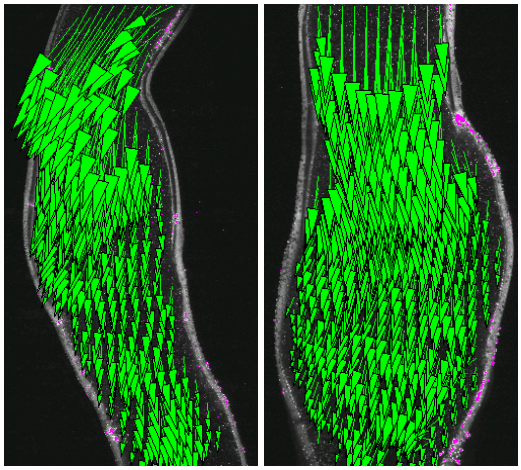

Figure 4.16: Phase-averaged velocity field measured in the left and posterior planes in the anatomically correct model at time B.

3. Extension to anatomically correct geometries

In order to relate these results measured in non-realistic models of AAA to anatomically correct aneurysms, we reconstructed a real shape aneurysm from CT scan images and tested it in vitro – see method in Appendix C. The present aneurysm is fusiform and it is large enough to have evolved into a non-symmetric shape (D/d = 2.7, L/d = 5.7). One can notice that this patient presents a larger curvature of the infrarenal aorta and a kink upstream of the aneurysm. PIV measurements of the velocity field were taken in two perpendicular planes. Figure 4.16 shows the velocity measured at time B in the left and posterior views. Similarly to what was observed in the experiments in the straight rigid models, the flow remains attached to the walls until the peak systole. In the decelerating portion of the cardiac cycle, the flow separates from the posterior and lateral walls (Figure 4.17 C). A large recirculating region is formed along the posterior wall downstream of the kink and along part of the lateral walls, subjecting them to low WSS. The anterior wall is simultaneously subjected to high WSS due to the large curvature of the vessel wall. Circumferential GWSS are therefore created, which may affect the

endothelial cells in the intermediate regions. The flow then reverses in the diastole, as shown in Figure 4.17 E. A transition to a weak turbulent state can be observed at that time.

C 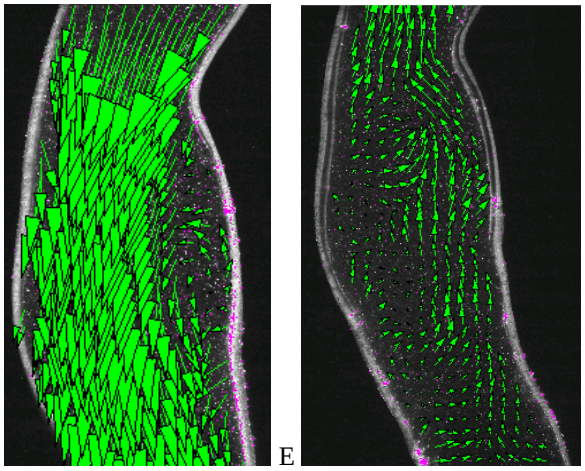 E

Figure 4.17: Phase-averaged velocity field measured in the left plane in the anatomically correct model at times C and E.

The measurements taken in the anatomically correct AAA model reinforce the likelihood of a correlation between architectural changes in the arterial trunk and the abdominal aortic aneurysm disease. In the case of the aneurysm reconstructed, the patient presents an increased bending of the infrarenal aorta and a kink below the bifurcation to the renal arteries. It is interesting to notice that the aneurysm has developed downstream of the kink. It is quite improbable that the aneurysm developed because of an increase in the static pressure, since it would have otherwise developed upstream of the constriction. It is more likely that the aneurysm developed due to the disturbed flow conditions induced by the abnormal anatomy.

D. Discussion

We have measured the spatial and temporal distribution of the wall shear stresses in idealized models of AAAs of increasing asymmetry parameter. It has been shown that most of the flow characteristics found in symmetric aneurysms persist in non-symmetric models of AAA. Up to large asymmetry parameters, the flow remains likewise attached to the walls in the accelerating portion of the systole. This engenders a decrease in the WSS inside the aneurysm as compared to the healthy vessel and therefore large GWSS at both necks. In an experiment conducted in model 16 (D/d = 2.4, L/d = 4.5, β = 0) with a sinusoidal flow waveform ($\langle \overline{Re} \rangle$ = 1700, $\overline{Re}_p$ = 2200), we have found that the flow does not reattach to the walls during systole, because of the too small systolic acceleration. Instead, a jet forms at the proximal neck in the early systole and discharges into the bulging cavity, preceded by a start-up vortex ring (Figure 4.18). An array of vortices forms in the shear layer, as the jet meanders through the aneurysm. In the case of large aspect ratios, such as in model 16, a helical instability may develop, as indicated by the staggered configuration of the counter-rotating vortices (Figure 4.18 (*b*)). This example shows the importance of reproducing adequately the flow waveform, the key events being the strong acceleration and deceleration generated *in vivo* in the systole.

In the case of the physiological flow waveform (Figure 2.5), a non-uniform separation occurs from the proximal neck as the flow decelerates. The geometric asymmetry affects flow separation and prevents the formation of a closed vortex ring as measured in axisymmetric models. Instead, a helical flow pattern develops in the AAA. The strongest vortex that is shed from the proximal anterior wall, where the wall curvature is maximal takes the shape of a hairpin vortex. As it progresses inside the aneurysm, it rotates in the cavity. The stretching of the vortex in the axial direction is much more important than in a symmetric aneurysm model. The strength of the vortex shed from the anterior wall also increases with the asymmetry parameter. In the case of

very large β, it is so strong that the hairpin vortex already impinges on the posterior wall in the early diastole. The increase in the vortex strength and stretching as β increases is likely to generate a stronger transition to turbulence in the diastole, although the turbulent intensity still remains weak.

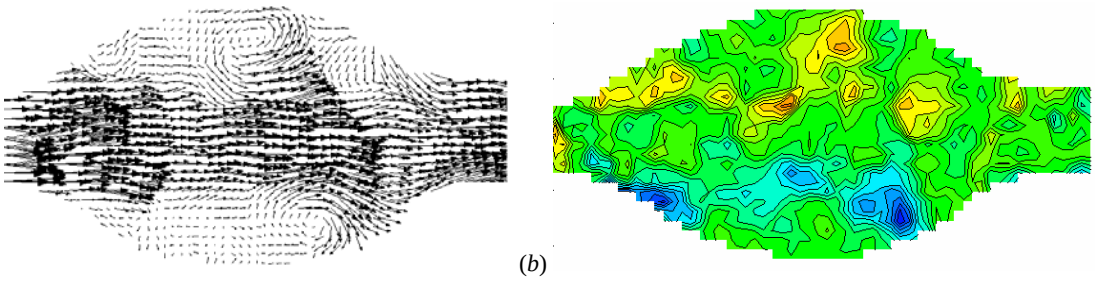

(*a*) (*b*)

Figure 4.18: Instantaneous velocity (*a*) and vorticity fields (*b*) measured at peak systole in the symmetric model (model 16) under a sinusoidal flow waveform.

Associated with this vortex are opposite patterns of WSS for the posterior and anterior walls. Because of the formation of a large recirculation zone, the endothelial cells along the anterior wall are subjected to very low and reversed WSS. Averaged over the length of the aneurysm and one cardiac cycle, the magnitude of the WSS is less than 20% of the value in a healthy aorta. Such a low level of stimulation is likely to greatly impair the endothelium, as discussed in the introduction. At stake is also the uni-directional quasi-steady stress pattern (in this case negative WSS) (Figure 4.19 (*a*)). In a healthy vessel, the VEC are exposed to pulsatile WSS that become negative only during diastole. Steady low shear stresses have been extensively studied in the literature and have been reported to lead to an increase in the rate of cell proliferation and apoptosis. In regions of quasi-stasis, the residence times increase drastically, enhancing all the diffusion processes through the walls. The flow conditions found along the anterior wall are therefore likely to promote the local accumulation of molecules such as low-density lipoproteins in the intima and media layers, leading to an inflammation of the vessel wall (Caro, Fitz-Gerald & Schroter 1971). Platelets and debris are also likely to deposit along

the wall. We can thus hypothesize that an endoluminal thrombus may form in these large regions of slowly recirculating flows.

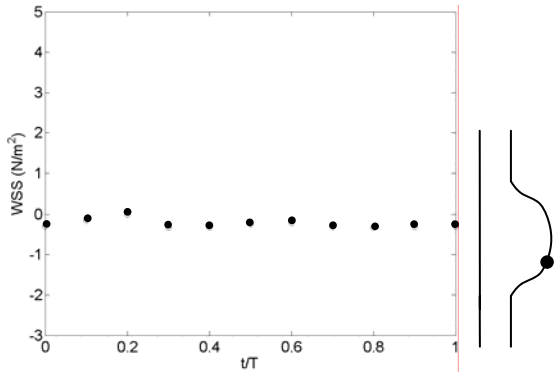

(*a*) *y/d* = 1.7

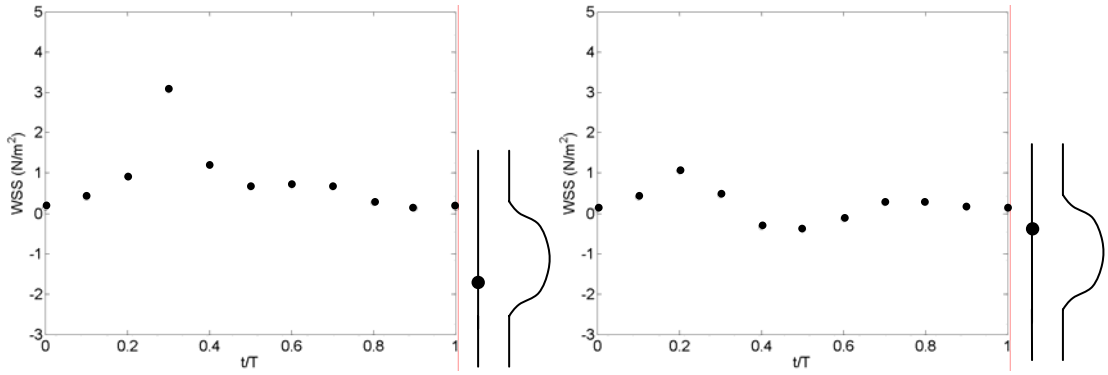

(*b*) *y/d* = 1.7 *y/d* = 3

Figure 4.19: Phase-averaged profiles of WSS measured in model 18 (β = 1) at *y/d* = 1.7 along the anterior wall (*a*) and at *y/d* = 1.7 and 3 along the posterior wall (*b*).

On the opposite wall, the endothelial cells of the proximal half are subjected to only positive WSS (forward flow) of much higher amplitude (Figure 4.19 (*b*)). Still the average magnitude is lower than in a healthy vessel (~ 60%), because of the influence of the bulging. A peak in WSS occurs in the region, where the vortex impinges the wall around *y/d* = 1.5-1.7. The distal half of the posterior wall, however, experiences oscillating WSS of about 1 N/m^2-amplitude (Figure 4.19 (*b*)). The difference in WSS patterns along the posterior wall generates GWSS in the medial section. Furthermore,

with the posterior and anterior walls subjected to radically opposite patterns of WSS, strong circumferential gradients of WSS are likely to be generated along the lateral walls.

E. Conclusion

We have quantified the effects of the loss of symmetry on the spatial and temporal distribution of wall shear stresses in abdominal aortic aneurysms. The measurements conducted in rigid non-symmetric models of AAA have indicated that some of the typical flow features measured in symmetric models persist. The flow remains attached during the systolic acceleration, although a limiting dilatation ratio exists above which the acceleration is not sufficient to guarantee it. Similarly to symmetric models, it has been observed that flow separation from the proximal neck occurs earlier when the dilatation ratio increases, which corresponds in this study to an increase in the asymmetry parameter β. However, the geometrical asymmetry leads to a situation, where the flow remains attached to the posterior wall, which prevents the shedding of a closed vortex ring. The largest vortex is shed from the anterior wall, where the local dilatation ratio is the highest. Its strength increases with the asymmetry parameter.

The massive detachment from the anterior wall and the shedding of this prominent vortex dictate the major changes in the WSS patterns. On the one hand, the anterior wall is subjected to very low shear stresses ($\overline{WSS}_{mean}$ = -0.20 N/m^2) that are not only fully reversed (OSI = 1) but also quasi-steady. Associated with this very slowly recirculating flow are long resident times that will promote the formation of an endoluminal thrombus. While the endothelial cells experience practically no shear stresses, the proximal and distal necks are weakened by very strong gradients of WSS.

On the other end, the proximal half of the posterior wall, up to the point of impact of the vortex, is subjected to forward flow (OSI = 0), with higher magnitude wall shear stresses. Without the influence of the vortex, the peak WSS naturally decreases in the

distal half generating high gradients of WSS downstream of the impact point. High gradients are also expected in the longitudinal direction along the lateral wall, since the anterior and posterior walls experience WSS in two opposite directions.

Chapter 5

Physiological relevance of the changes in hemodynamics for circulating blood cells in Abdominal Aortic Aneurysms

A. Introduction

It has been observed that 75% of AAAs with a maximum diameter of 4.5 cm develop an intraluminal thrombus (ILT). A few steady-flow studies have suggested that the build up of the thrombus may be associated with the altered hemodynamic patterns that arise inside the AAA when compared to the flow in a healthy abdominal aorta (Bluestein *et al.* 1996; Peattie *et al.* 1996).

In the previous two chapters, we have shown that the leading event caused by the formation of an aneurysm is the detachment of the flow from the wall around peak systole. The flow separation leads to the formation of recirculating regions along the walls and of a large vortex that traverses the aneurysm. Shear layers develop at the rear of the vortex leading to the presence of high shear stresses in the bulk of the flow. Excluding very long aspect-ratio aneurysms, the vortex impinges on the distal wall in the late systole, inducing high negative WSS and large gradients of WSS in the distal half of the aneurysm, while the proximal half is dominated by low and oscillating WSS. The

effects that these changes in the mechanical stimuli might have on the activation state of circulating blood cells have never been studied in abdominal aortic aneurysms.

As discussed in the introduction, hemodynamic forces have an important effect on the functions of platelets and leukocytes. The purpose of this study is to measure both the magnitude and duration of the shear stresses acting on blood cells circulating inside AAAs, and to characterize their changes as the AAA enlarges. Although several studies have reported on platelet–wall interaction in arterial anastomoses (Longest & Kleinsteuer 2003), stenosis (Einav & Bleustein 2004) and mechanical heart valves (Bluestein, Rambod & Gharib 2000; Yin *et al.* 2004), to the best of our knowledge, this is the first study to systematically quantify the effects of the aneurysmal dilatation on the time history of shear stress acting on individual blood cells, residence time, platelet activation level and possible deposition along the wall.

Precise measurements of the velocity field have been conducted in models of AAA using Particle Image Velocimetry (PIV). The trajectories of blood cells have been calculated from the measured velocity fields using a Lagrangian approach. The evolution of the shear-stress history on platelets and of platelet activation parameters are presented in section 3. The physiological consequences on the mechanisms of thrombosis are discussed in section 4.

B. Material and methods

Cell trajectories and total stress time history. A post-processing code was developed to calculate the trajectories of a few blood cells released at time t_0 at the entrance of the aneurysm with a zero initial velocity. Markers, representing the individual cells, were tracked both spatially and temporally inside the aneurysm, in a Lagrangian manner. In each symmetric aneurysm, ten cells have been continuously released during

one cardiac cycle from ten equally spaced locations along the entrance radius of the aneurysm. In the non-symmetric models, twenty cells had to be introduced spread along the vessel diameter, since the flow is no longer symmetric. The shape of the cells has not been reproduced in this study.

At each time step, the location to which the cells have traveled is calculated based on the phase-average of the velocity field measurements obtained with the PIV system (see Chapter 2 for the method and Chapter 3 and 4 for the results). Although the symmetry of the flow was shown to break down briefly in the systolic deceleration in symmetric models (section 2.D.1), the use of the phase-averaged velocity fields, which does not include the weak transition to turbulence, should limit the loss of symmetry. Therefore, we assume presently that the three-dimensional effects are small enough to guarantee that most of the cells remain in the symmetry plane of the aneurysm. This assumption may be challenged inside non-symmetric aneurysm, where 3-D effects are stronger. However, conducting the particle tracking in the plane of symmetry of the model should still provide a good approximation of the residence time and cell shear stress history. The fact that the flow in the perpendicular plane remains almost symmetric with respect to the plane of symmetry (Chapter 4) supports this assumption.

In order to smooth out the large time lag (0.084 s) between two PIV measurements, the velocity profiles are interpolated linearly at 25 intermediate time steps. This method of interpolation reduces the maximum distance traveled between two time steps (distance < 0.6 mm). Although the linearly interpolated field is not the exact velocity field, it prevents the large discontinuities in the trajectories that form otherwise. At each step, the cell is localized with respect to the grid, by finding the four closest grid points. The velocity of the cell is computed by interpolating the phase-averaged velocities at the 4 grid points, each velocity being weighted by a weight function proportional to the distance of the point to the cell. The new location of the cell is then calculated with a

second order accuracy (leap-frog method), knowing the cell velocity and the time step. Every 15 steps, an Euler scheme of first order accuracy has been used in order to avoid the divergence of the solution into 2 distinct trajectories. If the new position is located behind the aneurysm wall boundary, the cell is projected onto the aneurysm wall. This method prevents the cells from being artificially trapped inside the large wall steps that result from the coarse measurement grid. The code ensures that the cells are convected parallel to the wall, without crossing the boundary. The calculation of the cell trajectory ceases when the cell has left the aneurysm distally. However, in the case of large dilatation ratios, it may happen that a few cells become lodged along the walls in areas of reduced convection. An upper time limit had therefore to be introduced, set at 8 cardiac cycles, which was found to be sufficient for all the cells remaining in circulation to exit the aneurysm. The total-stress history is calculated for each cell along its trajectory, based on the total stress fields obtained from the space- and time- interpolation of the velocity fields measured with the PIV technique (see Appendix B for the definition of the total stress).

Cell activation parameter (CAP). As mentioned in the introduction, the activation of blood cells depends on the cell stress time history and on the time the cells are exposed to the stress. It is therefore assumed that the cell activation parameter (CAP) is directly proportional to the total stress and exposure time. Similarly to Yin *et al.* (2004) and Einav & Bluestein (2004), we calculated the CAP as the integral over time of the local total stress $\tau(t)$ acting on a particular cell

$$CAP = \frac{1}{\tau_{mean,H} \cdot L / \overline{U}} \int_{t_0}^{t_1} \tau(t')dt', \qquad (5.1)$$

where t_1 is the time the cells left the aneurysm. The stress integral is non-dimensionalized by the mean total stress measured in the healthy parent vessel, $\tau_{mean,H}$, multiplied by the mean convective time $L/\overline{U}$.

Furthermore, we considered the case where the shear effects on the cells are not purely cumulative as assumed previously. We calculated the CAP incorporating a relaxation time-scale Σ, after which activation processes decay exponentially

$$\frac{d(CAP)}{dt} = \tau - \frac{CAP}{\Sigma}, \tag{5.2}$$

the solution of which is

$$CAP = e^{-t/\Sigma} \int_{t_0}^{t_1} \tau(t') e^{-t'/\Sigma} dt' . \tag{5.3}$$

The introduction of a relaxation time-scale is in agreement with the experiments, which show that the state of activation is suppressed, when the high stress stimulus is stopped.

In both cases, blood cells are initialized with a zero activation parameter. *In vivo*, activation could occur upstream of the aneurysm, but the current calculation concentrates on the sole effect of the presence of an aneurysm on the circulating cells.

Near-wall residence time (NWRT). Besides activation, bringing platelets and leukocytes in the vicinity to the wall is crucial for thrombosis to occur. This is one of the mechanisms through which convective flow patterns may greatly affect thrombosis. To quantify this effect, we measured the near-wall residence time (NWRT), first introduced by Longest & Kleinsteuer (2003). It is the integral of the average residence time weighted by the square of the distance, *h*, of the blood cell to the wall, calculated along the trajectory of each cell:

$$\mathrm{NWRT} = \frac{\overline{U}L}{T} \int_{t_0}^{t_1} \frac{1}{h^2} \left(\frac{\Delta x^2 + \Delta y^2}{u^2 + v^2} \right)^{1/2} dt', \tag{5.4}$$

where Δx and Δy are the distances traveled in the x- and y-directions in between two time steps. The time- and space- averaged characteristic velocity in the parent vessel $\overline{U}$ has been incorporated with the length of the aneurysm L and the period T to non-dimensionalize the residence time.

C. Results

1. Influence of the AAA on the cell trajectories, residence time and stress history

The trajectories of ten blood cells have been calculated in all the models indicated in Table 5.I, when released at the ten different instants of times that compose one cardiac cycle. Figure 5.1 (*a*) shows the trajectories of the cells in the case of a medium dilatation ratio D/d = 2.1 (model 5). The cells have been released at y/d = -0.8 at time C. The cells are first confined inside the large jet that discharges into the aneurysm. But in the diastole, as their velocity decreases, they are entrained into the vortex structures and recirculating flow regions. Most of the cells recirculate in the distal half of the aneurysm, remaining in the region where most of the vortex structures are present.

One common pattern is the convection of cells towards the wall. As the cells recirculate, they are periodically led to travel very close to the wall. The time history of total stress experienced by these cells is plotted in Figure 5.1 (*b*). One can notice that all the cells experience highly fluctuating stresses, with high peak values occurring when the cells are present close to the wall at peak systole. Some of the cells exit the vortical flow after one cardiac cycle, while others stay for longer periods of time (up to five cardiac cycles, in this particular case). This entrainment of the cells into the vortical structures and recirculating flow regions persists throughout the cycle. Very few cells travel inside the aneurysm without being disturbed by its presence.

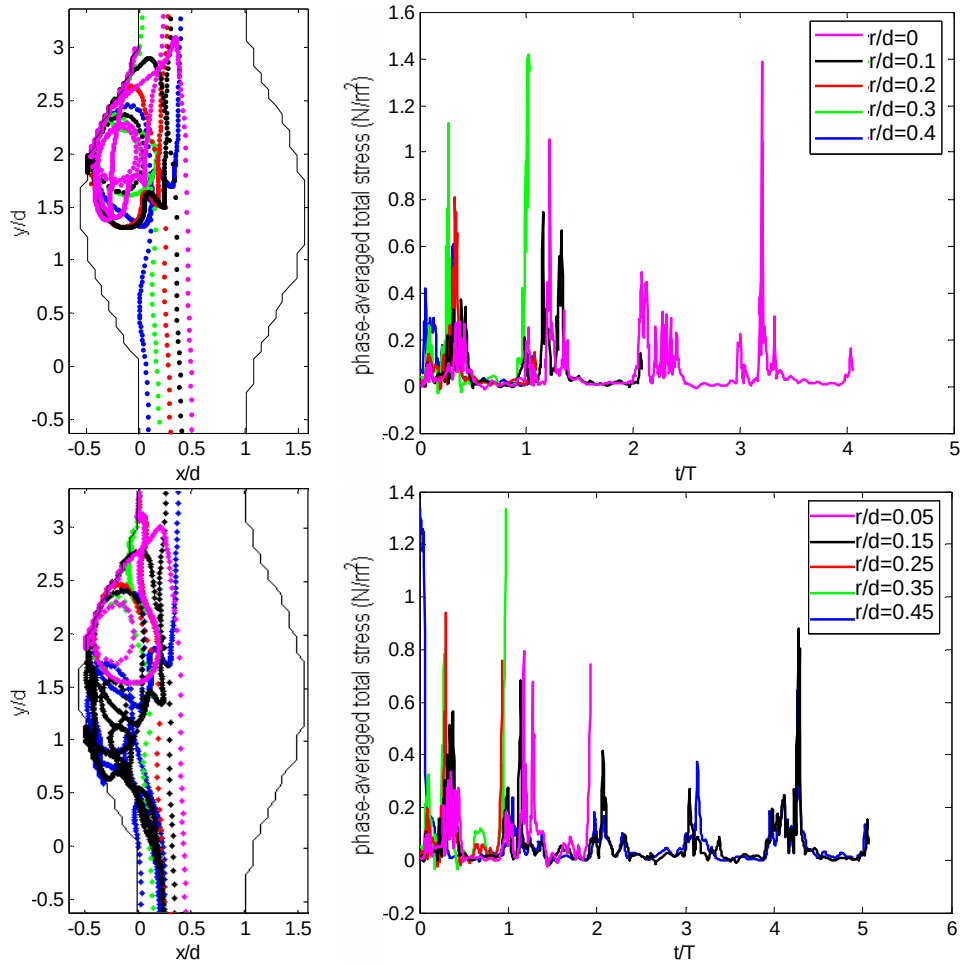

Figure 5.1: Trajectories and stress history for the 10 cells released in model 5 (D/d = 2.1, L/d = 2.9) at y/d = -0.8 at time C.

Abdominal aortic aneurysms therefore have a very strong effect on the trajectories and stress history on blood cells. The flow in the healthy aorta has been detailed in Chapter 3. From the velocity profiles, shown in Figure 5.2 (*a*), one can deduce that the trajectories of the cells are rectilinear (u = 0) and that a large number of cells experience minimal stress stimulation during their transit. The blunt velocity profiles give rise to a zero-stress condition in the bulk of the vessel throughout the cardiac cycle (Figure 5.2 (*b*)). Contrary to the case observed in an aneurysm, only the cells confined between the wall (y/d = 0) and y/d ~ 0.2 are exposed to some level of stress in a healthy vessel. The typical residence time of a cell inside an aneurysm of length L is $L/\overline{U}$. In the case of

model 5 (D/d = 2.1), characterized by an aspect ratio of L/d = 2.9, $L/\overline{U}$ = 0.45T when the actual average residence time is 3.44T. This shows that the presence of the aneurysm largely increases the residence time. The average stress the cells are subjected to across the vessel also increases in the aneurysm, the average stress being 63% higher than in the healthy vessel.

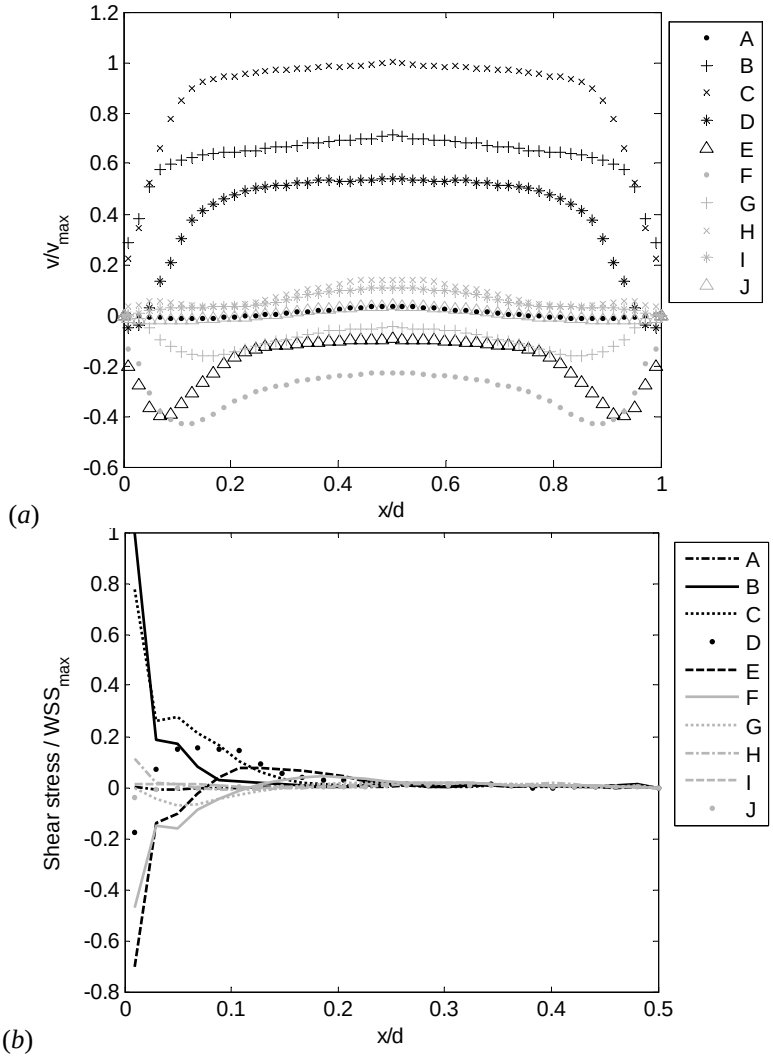

Figure 5.2: (*a*) Velocity and (*b*) stress profiles across a healthy vessel at the 10 instants of time that compose one cardiac cycle. The stress profiles are only shown for half the vessel.

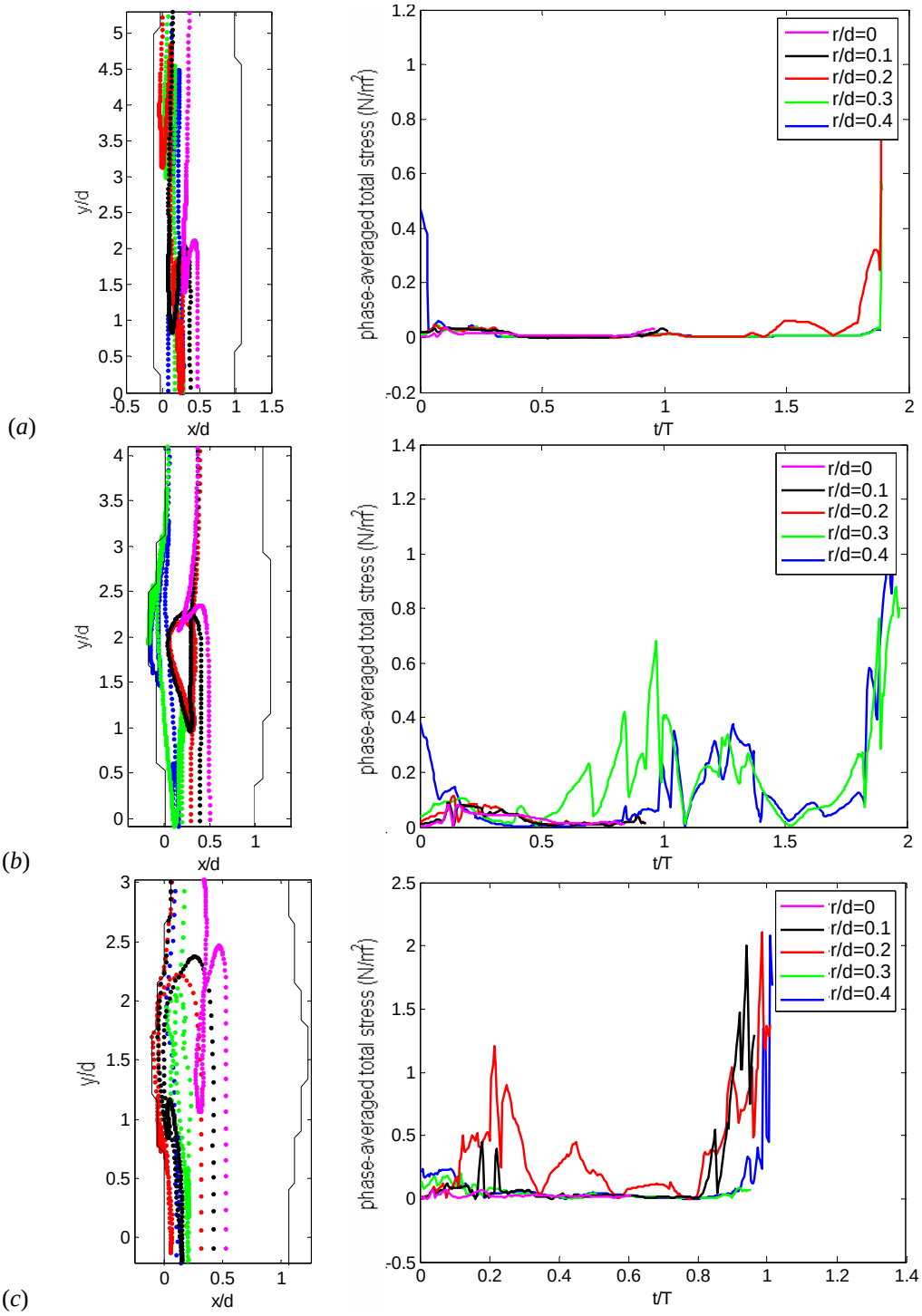

Figure 5.3: Effect of the decrease in the aspect ratio on the trajectories and stress history of cells. The cells were respectively released in model 11 – L/d = 5.2 (*a*), model 6 – L/d = 3.9 (*b*) and model 1 – L/d = 2.9 (*c*) during systole (time C) at y/d = -0.8.

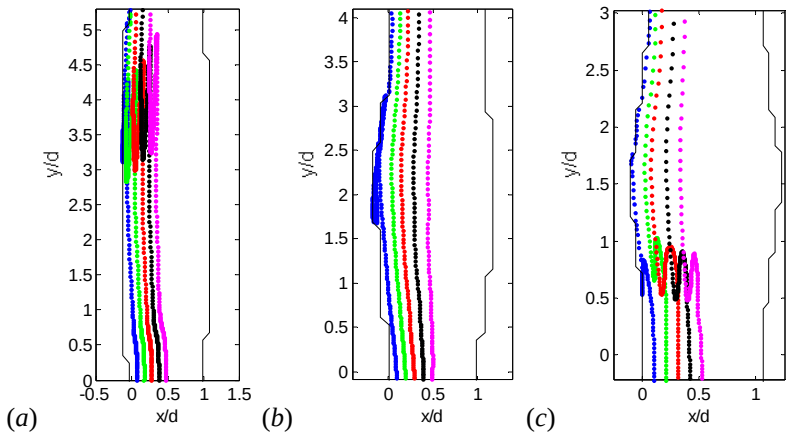

Figure 5.4: Trajectories of cells released in model 11 – L/d = 5.2 (*a*), model 6 – L/d = 3.9 (*b*) and model 1 – L/d = 2.9 (*c*) during diastole (time G) at y/d = -0.8.

2. Effects of the aspect ratio

The velocity measurements have shown that the wall shear stresses depend on the geometric parameters of the aneurysm, L/d, D/d and β. We report here how the blood cells are conjointly affected by the enlargement of the aneurysm. It was chosen to show the effects of the aspect ratio (L/d) in incipient aneurysms, in order to gain some insight on the possible mechanisms responsible for the formation of AAAs. The three models, models 11, 6 and 1, have the same dilatation ratio (D/d = 1.3), which is below the critical ratio of 1.5 used clinically to define an AAA. The length of the models has been decreased from an aspect ratio of 5.2 to 3.9 and finally 2.9. The pathlines and stress history are shown in Figure 5.3 for five cells introduced after the peak systole (time C). In the model with the largest aspect ratio (model 11), only the cells released at time C experience the effects of the very weak vortex shed between time C and D from the proximal neck. The trajectories are slightly skewed towards the centerline, when they follow the aneurysm shape at any other time (see Figure 5.4 (*a*)). However, the mean stress averaged over all the cells remains identical to the healthy vessel case. As the aspect ratio decreases, the vortex ring strengthens and a recirculating zone is formed.

Thus, the mechanism of active transport of the cells towards the wall already takes place at dilatation ratios as small as 1.3 and aspect ratios smaller than 4.

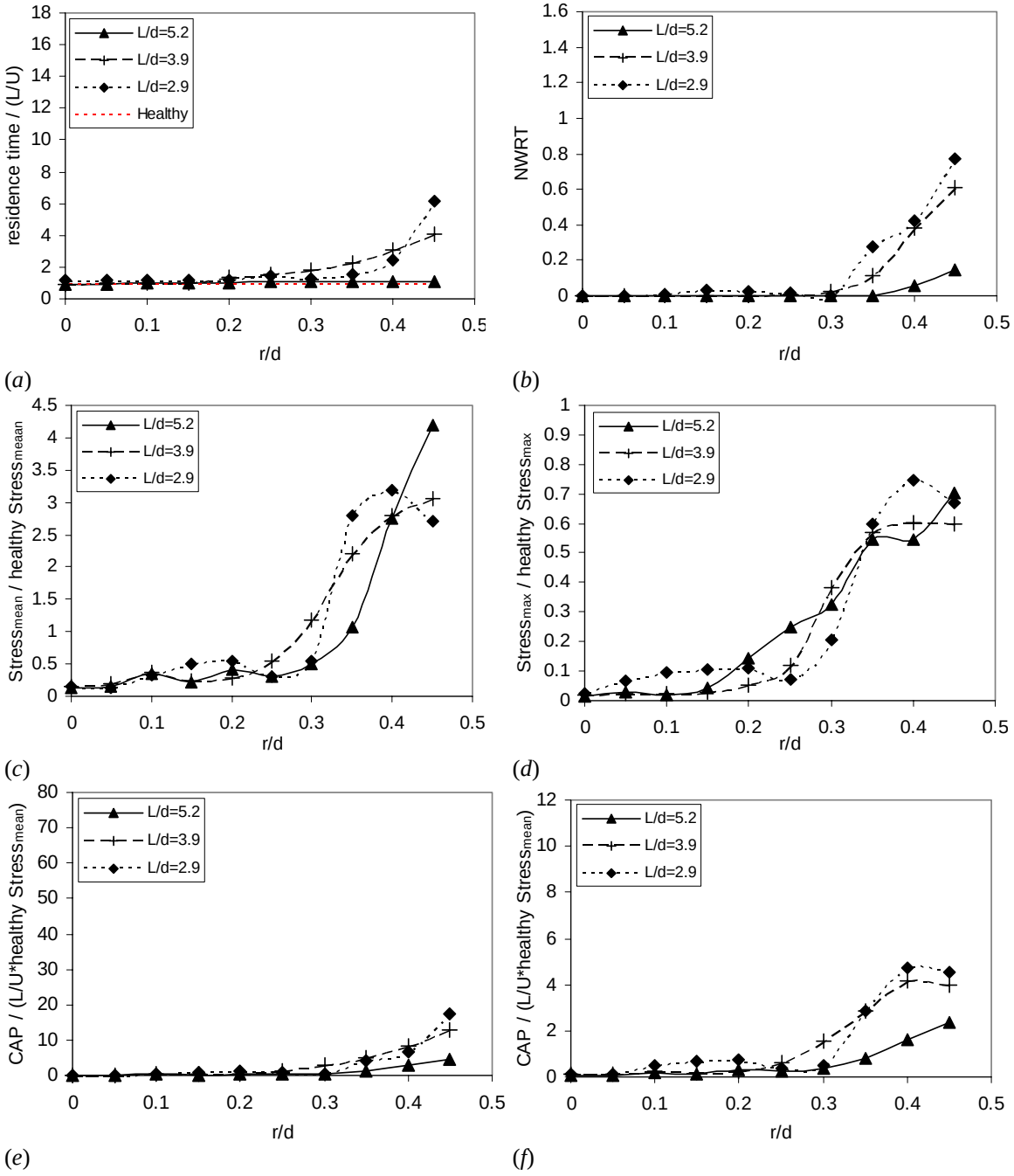

Figure 5.5: Comparison of the residence time (*a*), near wall residence time (*b*), mean (*c*) and peak (*d*) values of the stress and platelet activation parameters with (*e*) and without (*f*) the input of a relaxation time in models with decreasing aspect ratio. The dilatation ratio and asymmetry parameter are kept constant. *r/d* indicates the location where the

cells have been released in the parent vessel. The calculated quantities represent the averaged value over all the cells released at a specific location at 10 instants of time in one cardiac cycle.

Figure 5.5 compares the time-averages of the different parameters introduced in section B, when decreasing the aspect ratio: the residence time non-dimensionalized by the typical residence time in a healthy vessel ($L/\overline{U}$), the near wall residence time (NWRT), the mean/peak stress non-dimensionalized by the corresponding value in the healthy vessel and finally the cell activation parameter (CAP) calculated with and without a relaxation time. There is a consistent increase of all these parameters when the aspect ratio of the aneurysm is decreased. One can also observe that all these parameters decrease as the position of cell release gets further from the wall. Similarly to a healthy aorta, it is the cells closest to the wall that experience longer residence time and higher stress values, which results in a higher cell activation parameter for these cells. The cells located between r/d = 0 and 0.3 experience almost identical residence times (~ $L/\overline{U}$) and stress as in the healthy vessel. Still, a small increase in the residence time is noticeable in the model with the smallest aspect ratio (model 1), in which the blood cells from the center of the vessel start to be entrained in the incipient recirculating flow regions.

3. Effect of the dilatation ratio

The dilatation ratio has been linearly increased from 1.3 to 2.1 to study the effects that the aneurismal enlargement might have on the cells. The results are shown in models 1 to 5 that are characterized by the smallest aspect ratio (L/d = 2.9), since increasing the aspect ratio has been shown to attenuate the effects of the dilatation parameter. The trajectory and stress time history of a few cells introduced at time C for D/d = 1.5 (model 2) and D/d = 1.9 (model 4) are shown in Figure 5.6. They can be considered in conjuncture to Figures 5.1 and 5.3 (*c*), which show the results for D/d = 2.1 (model 5)

and *D/d* = 1.3 (model 1) respectively. The size and strength of the vortex ring increases as *D/d* increases, which leads to a larger recirculating region. The likelihood for the cells to be entrained into the recirculating region therefore increases with the dilatation ratio. As *D/d* increases, more cells might be enclosed in a slow transitional motion along the vessel wall, in which cells remain for long residence times (longer than eight time the healthy residence time) as observed in Figure 5.6 for the cells introduced at *y/d* =0.1. This phenomenon of rampant motion along the wall leads to an increase in the near wall residence time.

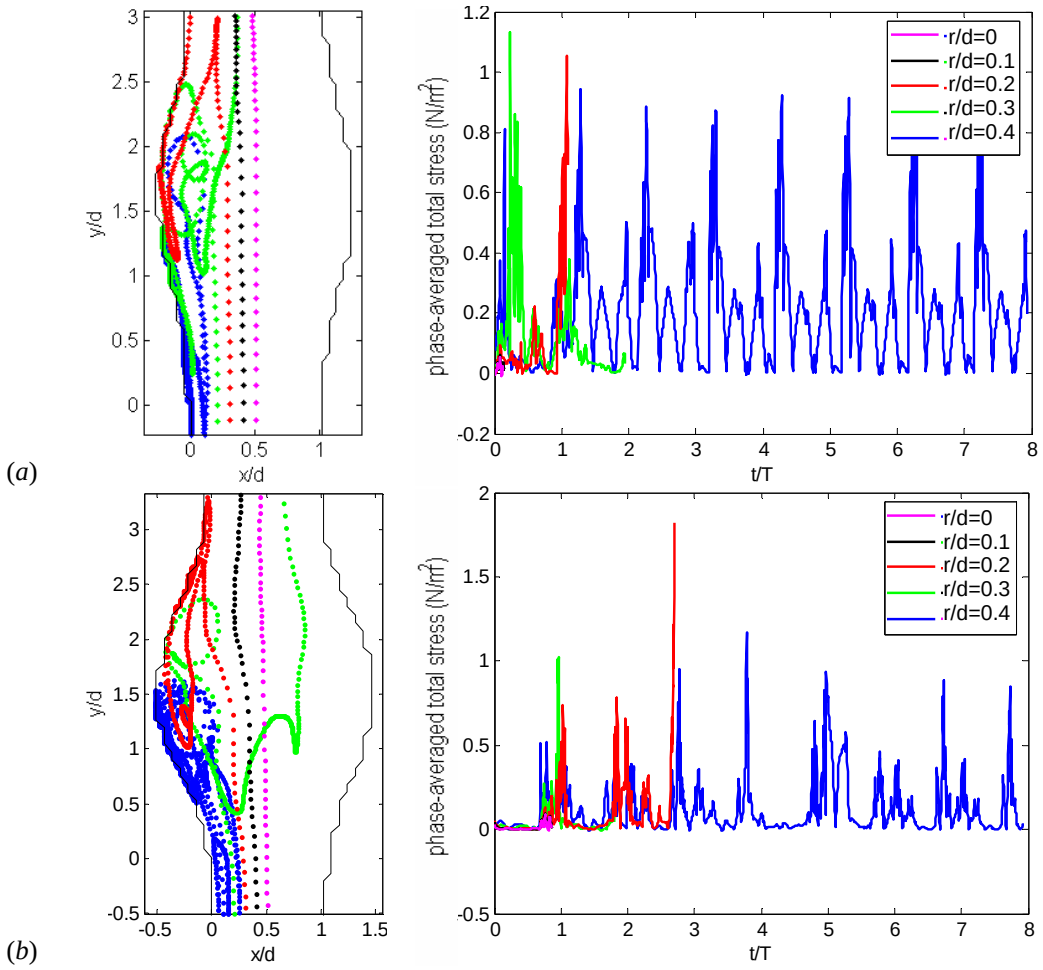

Figure 5.6: Trajectories and stress history of cells released in models 2 – *D/d* = 1.5 (*a*) and model 4 – *D/d* = 1.9 (*b*) during systole (time C) at *y/d* = -0.8.

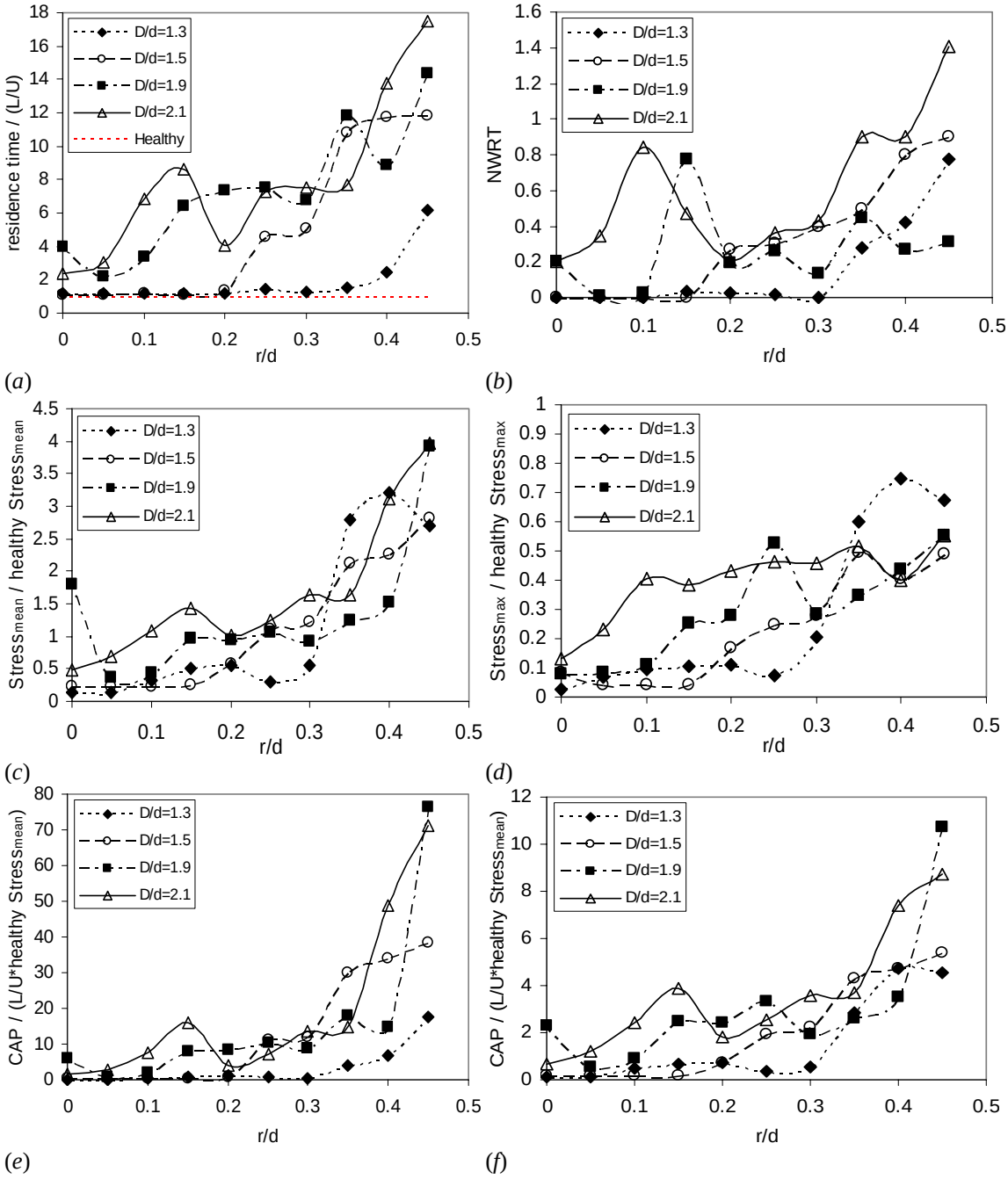

Figure 5.7: Comparison of the residence time (*a*), near wall residence time (*b*), mean (*c*) and peak (*d*) values of the stress and platelet activation parameters with (*e*) and without (*f*) the input of a relaxation time, when increasing the dilatation ratio. The aspect ratio and asymmetry parameter are kept constant. *r/d* indicates the location where the cells have been released in the parent vessel. The calculated quantities represent the averaged value over all the cells released at a specific location at 10 instants of time in one cardiac cycle.

The evolution of the cell activation parameters are plotted in Figure 5.7. As far as the cell response are concerned, one can make a clear cut at D/d = 1.5. Up to this aneurysm size (models 1 and 2), the cells in the bulk of the aneurysm maintain a normal residence time and low stress exposure, similar to the values in a healthy vessel. However, when the dilatation ratio exceeds 1.5, the residence times and mean and total stresses markedly increase for all the cells regardless of their position across the vessel. The activation parameter therefore increases to a non-zero value throughout the vessel, all the cells being susceptible to activate.

4. Effects of the asymmetry parameter

As we have seen in Chapter 4, mid-size aneurysms tend to further grow non-symmetrically. The effect of the increase in the model asymmetry was therefore studied in larger size aneurysms, although the maximum diameter was kept under the critical size of 4.5 cm, above which an intraluminal thrombus is more likely to form. The trajectories and stress history are represented in Figure 5.8 inside models 17 (*a*) and 18 (*b*), which are respectively characterized by an asymmetry parameter of 0.5 and 1.

The cells are first convected towards the posterior wall, their trajectories being influenced by the shedding of a strong vortex from the proximal anterior wall. The vortex then impinges on the posterior wall entraining the cells into the recirculating region, where they remain for a few cardiac cycles. The calculation of the cells' pathlines shows how the recirculating region extends over the entire aneurismal cavity in the case of non-symmetric aneurysms. Surprisingly, the residence time is found to decrease as the asymmetry parameter is increased. In the model of medium eccentricity (β = 0.5), the vortical flow structure traps cells for residence times 30% higher than in the model of maximum eccentricity (β = 1) (Figure 5.9 (*a*)). Contrary to the symmetric models, the residence times, stress intensity and activation parameter no longer depend on r/d (Figure

5.9). The large recirculation induces a very strong mixing inside the aneurysm, which suppresses the radial dependency. Although no cell experiences the very high values of the parameters measured in symmetric aneurysms for cells introduced close to the wall, all the parameters maintain much higher values than in a healthy vessel, the mean stress being for example 40% higher.

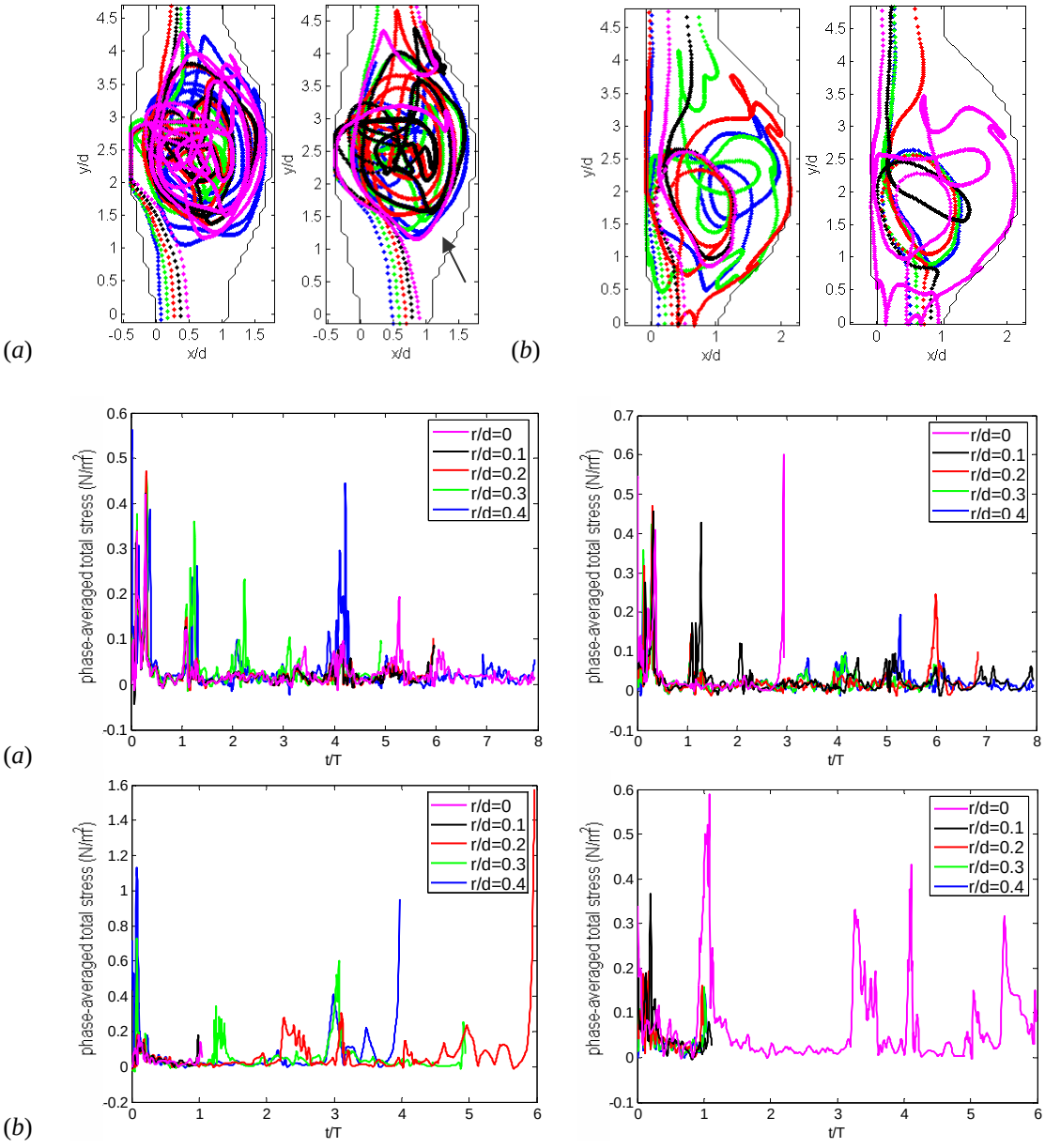

Figure 5.8: Trajectories and stress history of cells released in models 17 – β = 0.5 (*a*) and 18 – β = 1 (*b*) during systole (time C) at *y/d* = -0.8.

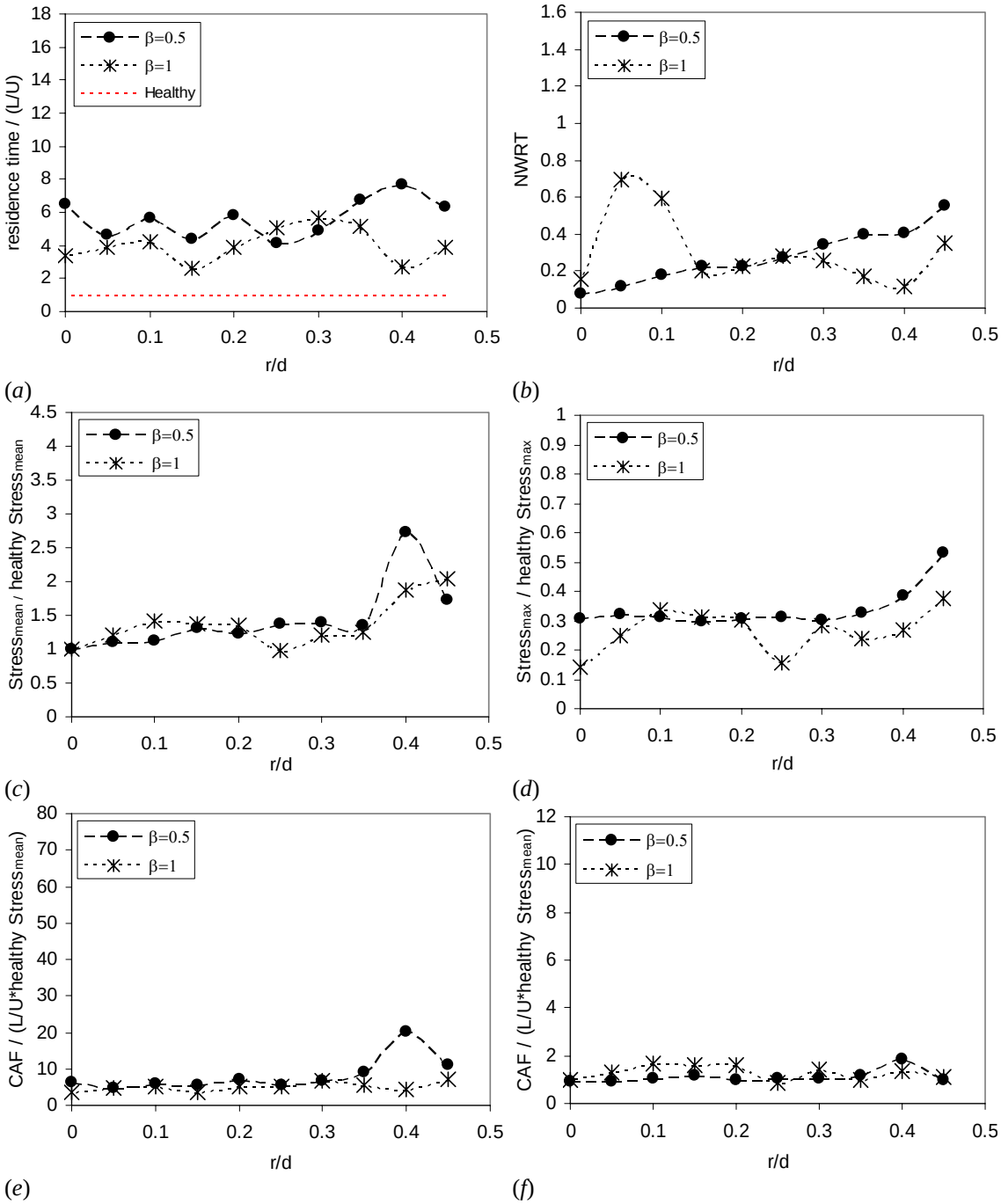

Figure 5.9: Comparison of the residence time (*a*), near wall residence time (*b*), mean (*c*) and peak (*d*) values of the stress and platelet activation parameters with (*e*) and without (*f*) the input of a relaxation time when increasing the asymmetry parameter. *r/d* indicates the location where the cells have been released in the parent vessel. The calculated quantities represent the averaged value over all the cells released at a specific location at 10 instants of time in one cardiac cycle.

D. Discussion

The purpose of this study is to analyze the mechanisms that might account for the formation of an intraluminal thrombus. The important question to be elucidated is the role that the “disturbed” flow and stress conditions might play on the thrombus formation in AAAs. In order to measure how blood cells are affected by the growth of the aneurysm, a code has been developed to follow blood cells inside the aneurysm in a Lagrangian way and quantify their individual residence time and time history of stress. The cells’ trajectories are calculated using the PIV measurements of the velocity field, interpolated both in space and time. Special care has been taken to compute appropriately the transport close to the wall.

As the AAA enlarges, the platelets, leukocytes and red blood cells are locally subjected to higher levels of shear stresses. High shear stresses are formed inside the aneurysm as a result of the flow separation and formation of a large vortex. They occur inside the internal shear layers and to a larger extent at the walls, at the points of impact of the vortices. The peculiarity of the aneurismal flow topology is to transport the cells towards the wall, right into these regions of higher shear stresses. In these regions, the cells may become moderately activated, which may lead to a weak aggregation of the cells to one another. It has been shown by Wurzinger et al. (1985) that only such an active transport of the cells towards the wall can lead to the adhesion of activated platelet to the walls and to their aggregation. But without any further stimulation, the aggregates are known to dissolve very quickly. The moderate state of activation and aggregation can however be reinforced by the entrainment of the cells into regions of low stresses. When the translational motion of the cells is hindered by the presence of the wall, the cells are forced into the recirculating flow region, being entrained by the nearby vortex. The cells thus enter a region of very low shear stresses, which is known to foster aggregation (Alveriadou *et al.* 1993). The crucial parameter is the time the cells remain inside the

recirculating regions. Based on steady-flow experiments, Huang & Hellum (1993) have found that residence time of the order of at least 10 s is required for significant shear-induced aggregation. Although the pulsatile nature of the flow might influence their conclusion, our results show that such long residence times occur inside the aneurysm, if large enough. Moreover, we showed that, when recirculating, the cells are periodically exposed to higher stresses, since they are regularly brought in contact with the walls. This alternate high/very low stress stimulation along with long residence times might be responsible for cell activation and the convective patterns might then foster deposition along the wall.

All these phenomena are strongly dependent on the size of the aneurysm. Since the mechanisms for cell activation and aggregation depend on the presence of a strong vortex, regions of high wall shear stresses and moderately large regions of slowly recirculating flow, they may only occur in developed aneurysms. The calculation of the different activation parameters has shown the build-up of activation processes as the aneurysm grows. The time- and space-averaged values of all these parameters are represented in Figure 5.10. Figure 5.10 (*a*) indicates that decreasing the aneurysm aspect ratio may increase the residence time by a factor of 2, when the increase in dilatation ratio may lead to a 4.2-fold increase in both the residence time and near-wall residence time (Figure 5.10 (*b*)). The dilatation ratio influences similarly the mean value of the stresses acting on the cells and cell activation parameter (Figure 5.10 (*c*-*e*)), giving rise to a 20-fold increase of the CAP in the case of a medium-size aneurysm (D/d = 2.1) as compared to a healthy vessel. Figures 5.10 (*e*) and (*f*) show that, although more physical, incorporating a relaxation time in the calculation of the cell activation parameter provides similar results to the simple integration of the stress simulation over time.

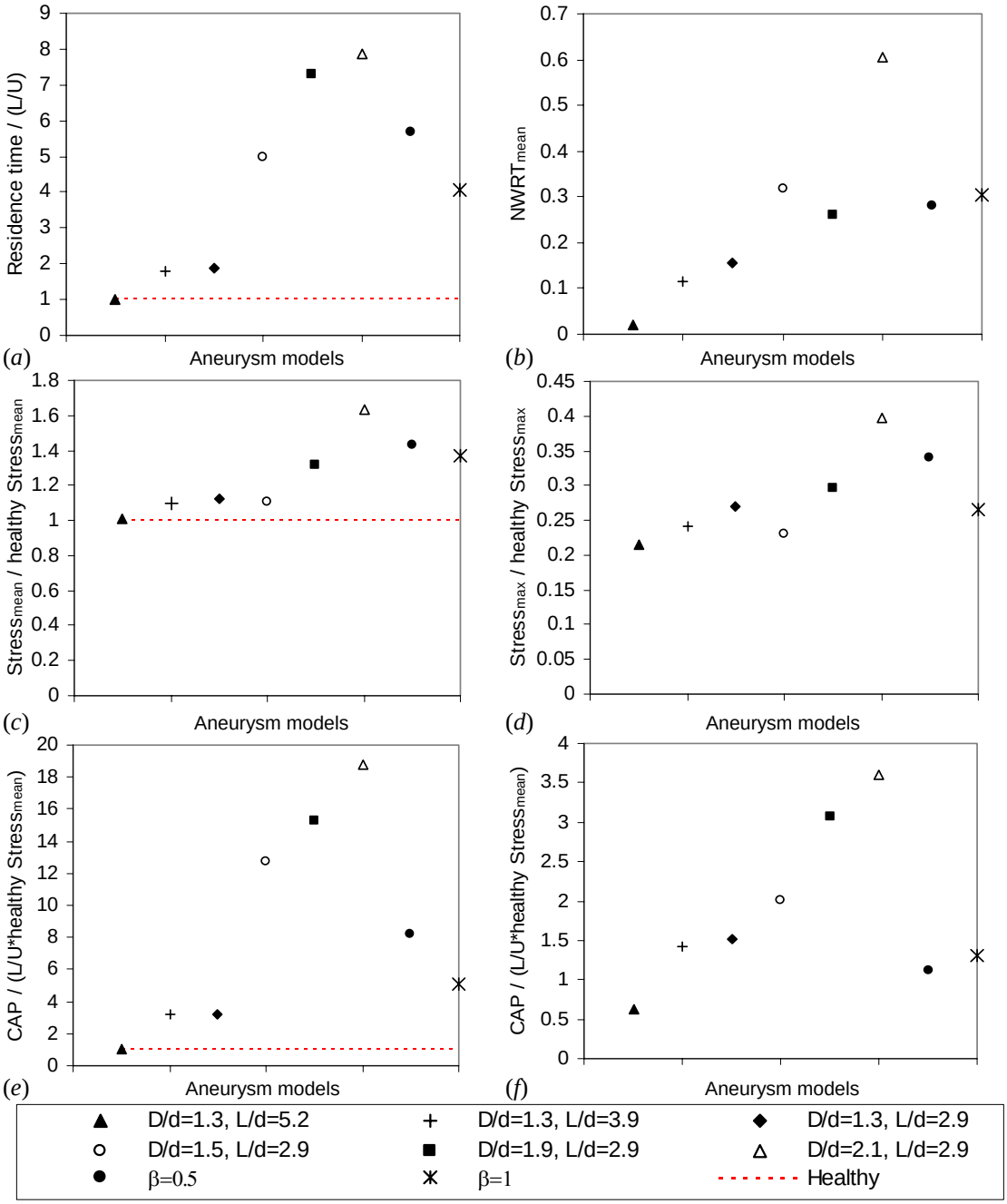

Figure 5.10: Effects of respectively the aspect ratio, dilatation ratio and asymmetry parameter on the mean values of the residence time, near wall residence time, mean and peak values of the stress and platelet activation parameters with or without the input of a relaxation time. These quantities, time- and space-averaged over all the cells released inside the models, are plotted for each model (abscissa).

An important phenomenon is the increase in the number of blood cells enclosed in the recirculating zone as the aneurysm grows. Small size aneurysms preserve an intact bulk region. But as the aneurysm reaches larger sizes, all the cells become likely to be exposed to the alternate pattern of high/low stresses for long residence times. Moreover, the persistence of the cell recirculation inside the aneurysm throughout the cardiac cycle only occurs when $D/d > 1.9$. In small size aneurysm, the recirculating structures are rapidly broken down in the diastole, when they persist in larger size aneurysms. These structures are the strongest in the non-symmetric models, especially in medium eccentricity models ($\beta \sim 0.5$). The recirculating zone takes over the whole aneurismal cavity, where cells move steadily at low velocities.

The activation and aggregation states of circulating cells are also highly affected by the activation state of the endothelial cells. The endothelial cells lining the vessels react to the changes in mechanical stimuli in the AAA. They have been shown to get activated both in regions of large gradients of wall shear stresses (as in the distal half of the AAA) (DePaolo et al. 1992; Tardy *et al.* 1997; Nagel *et al.* 1999) and in regions of low and oscillating wall shear stresses (as in the proximal half of the AAA) (Helmlinger, Berk & Nerem 1995; Moore *et al.* 1994). The cell tracking showed that the blood cells preferentially come very close to the wall in these 2 distinct regions: the cells are transported into the distal wall and then entrained upstream into the recirculating zone. The activated state of the endothelial cells fosters wall adhesion of the already partially aggregated blood cells and the release of chemical signals that potentiate the activation of platelets and leukocytes. Inflammation of the endothelium will therefore provide the optimal cell-adhesive conditions that may contribute to the pathogenesis of an intraluminal thrombus.

The thrombus is likely to develop in the detached flow region (Reininger *et al.* 1995) until the endoluminal channel is of the same diameter as the parent vessel. The infrarenal

abdominal thrombus is the only case of a thrombus that does not occlude the entire cavity and through which flow is maintained. The thrombus may provide some support to the weakened wall. However, this gain in structural strength is at the cost of a drastic reduction in oxygen diffusion to the medial layer, the disappearance of all endothelium-derived regulatory processes and the onset of inflammatory-mediated degenerative conditions throughout the arterial wall and within the thrombus itself. All these factors are known to contribute to the further deterioration of the medial layer, which is key to the structural strength of the wall and to the continued or even accelerated enlargement of the AAA (Kazi *et al.* 2003).

E. Conclusion

In this study, we have shown that cell activation processes are likely to occur inside abdominal aortic aneurysms and that they may account for the formation of an intraluminal thrombus inside the aneurysm. A post-processing code was developed to track individual blood cells both spatially and temporally using the PIV measurements of the velocity and stress field inside the aneurysm. In order to quantify the levels of cell activation, we have calculated the trajectories of circulating cell as well as the magnitude and duration of the stresses acting on them. The effects of the aneurysm enlargement have been considered by changing systematically the geometric parameters of the models.

The parametric study shows that cell activation may be the result of the formation of regions of larger shear stresses in the internal shear layers and along the walls, at the locations of impact of the vortices. High shear stresses may activate cells and lead to their weak aggregation. The size and strength of the vortices have been shown to increase as the aneurysm grows, which accounts for the increase in the mean shear stresses acting on the cells (up to 60% higher in a medium size aneurysm) and in the number of cells being

entrained into the recirculating regions. As the aneurysm grows in size, a larger number of cells are subjected to low stress conditions, recirculating at low speed for several cardiac cycles. These cells are periodically subjected to higher shear stresses when brought in the vicinity of the wall at peak systole. Furthermore, as the dilatation ratio increases, the separated flow regions become larger in size, which leads to an increase in the cell residence times. An 8-fold increase of the residence time has been measured in a medium size symmetric aneurysm. On the contrary, increasing the aspect ratio reduces the pathological effects induced by the aneurismal dilatation.

From the results of this study, we hypothesize that the transition towards a non-axisymmetric shape is necessary for an intraluminal thrombus to form. In symmetric aneurysms, the flow reattaches to the walls at every systolic push, so that patterns of constantly recirculating cells hardly arise. The amount of cell deposition along the walls is also likely to be considerably reduced, since cell aggregates may be entrained from the wall at every cycle. In the case of non-symmetric aneurysms, however, all the thrombotic flow conditions are met. The blood cells have been shown to recirculate into the aneurysm cavity in a quasi-steady slow circular motion for long residence times. Since flow reattachment does not occur for large asymmetry parameters, a thrombus may form along the anterior wall, in regions such as the one indicated by an arrow on Figure 5.8 (*a*). Furthermore, inflammation processes are very likely to occur in the anterior wall, since the endothelial cells are subjected to almost zero wall shear stresses. Quasi-static flow conditions are known to activate the endothelial cells and possibly lead to their apoptosis and later exposure of submatrix collagen. They also lead to the increase of the wall porosity, possibly resulting in cholesterol deposit inside the walls. These injured and inflamed wall regions send signals to recruit platelets and leukocytes, which fosters thrombus formation.

This study was the first one to analyze possible cell activation processes inside AAAs. The changes in the mechanical stimuli acting on the cells and in their residence time have been quantified during the aneurysm enlargement. The results of this study could help choose physiologically relevant patterns of shear stresses and residence times for new studies on circulating cells under pulsatile flow conditions. These studies would provide the much-needed information that would validate or invalidate our postulates.

Chapter 6

General conclusion and perspectives

A. General conclusion

For the last few decades, it has been recognized that abdominal aortic aneurysms result from a complex interplay between mechanical stimuli and biochemical reactions occurring inside the arterial wall. Hemodynamic stresses (pressure and wall shear stresses) are thought to affect the mechanisms responsible for the formation, growth and rupture of AAAs, via their effects on the endothelial cells, smooth muscle cells and blood cells. Endothelial and smooth muscle cells act as sensors of the hemodynamic forces and actuators, transducing the signals into vasomotor responses. Experiments have shown that the cells react not only to the magnitude of the shear stresses, but also to their spatial and temporal variations. Perturbations from the baseline stress conditions alter the mechanisms of mechanotransduction for both types of cells. Circulating blood cells also respond to the fluid stresses and may become activated in case of exposure to high or very low stresses. The main objective of the dissertation was to characterize the changes in the hemodynamic forces resulting from the enlargement of the abdominal aorta, in order to provide some insights on the role that the hemodynamic forces play in the

etiology and progression of the disease. We have measured the spatial and temporal distribution of internal and wall shear stresses in idealized models of AAAs, using Particle Image Velocimetry. The use of a well-controlled geometry for the models enabled us to quantify systematically the effects that an increase in aneurysm diameter, length or asymmetry might have on the stress field, which would not have been possible in physiologically-correct models.

We have shown that, even in the case of dilatation ratios as small as $D/d = 1.3$ (for $L/d < 4$), the flow separates from the wall after the peak systole, which leads to the formation of a vortex structure and of a separated flow region along the walls. These changes in the flow topology modify the hemodynamic forces acting on the endothelial cells and on circulating blood cells, since distinct regions of higher shear stresses (in the shear layer and point of vortex impingement), very low shear stresses (in the separated zone) and large spatial and temporal gradients of shear stresses (around the point of flow reattachment) form inside the aneurysm. The study of very incipient aneurysms proved that even a small change in the vessel geometry drastically changes the flow structures and stresses. An abdominal aortic aneurysm may therefore be initiated by a change in the vessel morphology, such as an increased bending or contraction, known to cause flow separation. We can hypothesize that a healthy wall would readjust its shape to avoid the presence of flow separation, but the changes in the wall properties due to aging, hypertension or any other risk factor discussed in the introduction might prevent the natural healing processes.

We have found that most of the flow patterns that form in symmetric aneurysms persist in non-symmetric AAAs. Up to very large dilatation ratios, the flow remains attached to the walls in the systolic acceleration. This engenders a decrease in the WSS inside the aneurysm and therefore large GWSS at both necks. The flow only detaches from the proximal neck during the systolic deceleration. In the case of symmetric

aneurysms, a large start-up vortex ring forms and, as it propagates through the aneurysm, secondary vortex rings develop in the associated internal shear layers. When non-symmetric, the geometric configuration prevents the formation of a closed vortex ring and the strongest vortex is shed from the proximal anterior wall. The vortex structure has the shape of a hairpin. In the case of moderate aspect ratios, the shed vortices impinge on the opposite (section of the) wall, causing locally large WSS. Large gradients of WSS consequently form along the vessel wall, since, outside the small area affected by the vortex, the wall is exposed to very low and oscillating wall shear stresses. During the diastole, the flow reversal causes a transition to a state of weak turbulence, which is subsequently dissipated over the resting period of the cardiac cycle. The transition to turbulence is stronger in non-symmetric models, since the hairpin vortex is exposed to a more intense stretching, which increases its strength.

These changes in the flow characteristics result in very large changes in the spatial and temporal distribution of the WSS acting on the endothelial cells as compared to those acting in the healthy aorta. Our measurements show the existence of two regions with distinct patterns of WSS and GWSS. The detached region is dominated by oscillatory wall shear stresses with a very low and negative average value. The reattachment region is characterized by large sustained GWSS and large negative WSS. In symmetric aneurysms, the detached region extends over the proximal half of the aneurysm and the reattachment region over the distal half. In non-symmetric aneurysms, the detached region is along the anterior wall and the reattachment region along the posterior wall.

In the shear layer and in the wall reattachment region, circulating blood cells are subjected to higher levels of shear stresses, which may cause the cells to activate and weakly aggregate. The peculiarity of aneurismal flow is indeed to transport some of the cells into the wall, right into the regions of high WSS and large gradients of WSS. This transport mechanism increases the probability of adherence of the cells to the wall at

these locations. Migration of the endothelial cells and possibly endothelial desquamation have been shown to occur along the reattachment wall, which is likely to lead to the inflammation of the vessel wall and enhance the activation processes in the circulating blood cells impinging on the wall. After their impact on the wall, the non-adhering cells are entrained into the recirculating flow regions, where they are subjected to low stresses. The cells recirculate at low speed for several cardiac cycles, being periodically subjected to higher shear stresses, each time they are brought in the vicinity of the wall at peak systole. The size and strength of the vortices shed from the proximal neck have been shown to increase as the aneurysm grows, which explains the increase in the mean shear stresses acting on the cells, as well as in the number of cells being potentially entrained into the recirculating regions. As the dilatation ratio increases, the separated flow regions also grow in size, which leads to an increase in the cell residence time. An 8-fold increase of the residence time has been measured in a medium-size symmetric aneurysm. On the contrary, increasing the aspect ratio reduces the pathological effects induced by the aneurismal dilatation. Furthermore, the persistence of the cell recirculation in the cavity throughout the cardiac cycle only occurs for dilatation ratio > 1.9. In small size aneurysms, the recirculating structures are rapidly broken down in the diastole, but they persist in larger size aneurysms. These structures are the strongest in the non-symmetric models, in which the cells move steadily at low speed for long durations inside the large recirculating zone. This exposure to low shear stresses for very long residence time is a very potent stimulus for cell activation. This activation state is reinforced by the extensive disruption of the endothelial cells caused by the very low and oscillatory wall shear stresses that rein in these detached regions. Upon activation, the mean volume of the platelets is multiplied by a factor of 8, which renders cell deposition very likely when associated with the convective flow patterns that bring the platelets in contact with the wall. However, these deposits along the walls can only be stable, if the convective forces

acting on them are weak. Thrombus formation is therefore less likely in symmetric aneurysms, where the flow reattaches to the wall during the systolic acceleration. However, we can expect thrombus to form along the anterior wall of non-symmetric aneurysm, along which the flow has been measured to be almost stagnant.

B. Perspectives

Studies of the effects of the measured stimuli on endothelial cells and circulating blood cells: In this dissertation, the changes in the shear stresses and gradients of shear stresses have been fully characterized during the progressive enlargement of abdominal aortic aneurysms. The large body of experiments of the literature that were conducted on endothelial cells, platelets and leukocytes exposed to different stress conditions was useful to postulate possible mechanisms responsible for the growth of AAAs. However, the results of these biological studies may be questionable when applied to the abdominal aortic aneurysm, since the vast majority of the experiments have been conducted in steady flow conditions. There is therefore a need for new experiments designed under pulsatile flow conditions. The flow conditions should be varied in order to simulate the specific spatial and temporal distribution of WSS and GWSS reported here. These experiments would monitor the effects of the different patterns of hemodynamic stimuli on the cell morphology, secretions and gene expression. They should provide the much-needed information necessary to elucidate the exact role that the measured patterns of WSS have on the etiology and progression of AAAs.

Field of platelet activation parameter: In the dissertation, we have computed the activation parameter along the trajectory of a few blood cells. In order to get a more global picture of the locations where activation is more likely, an activation field could

be computed inside the AAA. Similarly to the cell activation parameter calculated with a relaxation time Σ, the activation field is transported by the following equation:

$$\frac{dA}{dt} = \tau - \frac{A}{\Sigma}, \tag{6.1}$$

where *A* is the activation field. The equation can also be written in the convective form:

$$\frac{\partial A}{\partial t} + u\frac{\partial A}{\partial x} + v\frac{\partial A}{\partial y} = \tau - \frac{A}{\Sigma}. \tag{6.2}$$

We have attempted to solve this equation, using an implicit scheme, based on the leap-frog method (2^{nd} order accuracy), alternating with an Euler scheme every 15 time-steps. The initial condition at each point (*i*,*j*) inside the aneurysm, is the cell activation parameter that a particle would have after traveling through a straight tube during a certain time T

$$A_0 = \frac{\Sigma}{\mathrm{T}}\int_{t_0}^{\mathrm{T}} \tau(i, j, t')e^{-t'/\Sigma}dt'. \tag{6.3}$$

Outside the aneurysm, the activation is kept equal to zero. We apply a zero flux through the sidewall, as the boundary condition and a constant flux through the exit of the aneurysm at each time steps.

Although the code is implicit, 2^{nd} order accurate and satisfies the CFL condition, the code is unstable and diverges after a few time steps. The same equation is extensively used in research on polymers and it has been shown to be numerically stiff. It would be interesting to use some of the methods that researchers, such as Brasseur J. G. from Pennsylvania State University, developed to solve this type of equations.

Kinetic models of activation: The previous study would correspond to a kinetic model of activation of order zero. Kinetic models of order one could be derived in order to better understand the mechanisms of activation in AAAs. The simulation could

integrate a model of the coupling between endothelial cells, platelets and leukocytes and include the adhesive state of the walls depending on the values of the WSS and GWSS. This model could be a closer of this dissertation, since it would include all the mechanisms discussed here.

Numerical simulations of the flow and wall shear stresses in abdominal aortic aneurysms: It would be interesting to use the large body of experimental results in conjunction with numerical simulations of the flow in different models of AAA. The present database would help tune up the parameters of the numerical codes.

Appendix A

Calculations involved in post-processing of experimental data

A. Calculation of the strain rates

From the PIV measurements of the velocity field, one can calculate the shear strain field. The derivatives of the velocity field with respect to *y* (parallel to the main flow direction) and *x* (perpendicular to the main flow direction) are discretized using centered differences, with a second order accuracy

$$\left.\frac{\partial v}{\partial x}\right|_i = \frac{v_{i+1} - v_{i-1}}{2\Delta x}, \qquad \text{(A.1}a\text{)}$$

$$\left.\frac{\partial u}{\partial x}\right|_i = \frac{u_{i+1} - u_{i-1}}{2\Delta x}, \qquad \text{(A.1}b\text{)}$$

$$\left.\frac{\partial v}{\partial y}\right|_j = \frac{v_{j+1} - v_{j-1}}{2\Delta y}, \qquad \text{(A.1}c\text{)}$$

$$\left.\frac{\partial u}{\partial y}\right|_j = \frac{u_{j+1} - u_{j-1}}{2\Delta y}, \qquad \text{(A.1}d\text{)}$$

where (u,v) are the *x*- and *y*-components of the velocity field and (*i*, *j*) the *x*- and *y*-grid position indices. The wall is placed at $\Delta x/2$ away from the first or last grid points and the velocity at the wall is assumed to be null. The strain rates at the wall therefore read

$$\left.\frac{\partial v}{\partial x}\right|_{i\mp\Delta x/2} = \pm 2v_i / \Delta x, \qquad \text{(A.2}a\text{)}$$

$$\left.\frac{\partial u}{\partial x}\right|_{i\mp\Delta x/2} = \pm 2u_i / \Delta x. \qquad \text{(A.2}b\text{)}$$

(u_i,v_i) being the velocity vector measured at the first or last grid point inside the aneurysm.

B. Calculation of the vorticity and stress fields

From the velocity field, one can then calculate the vorticity and stress fields in the plane of measurement. The stress tensor for a Newtonian fluid can be written as

$$\sigma = \frac{1}{2}\mu[\nabla\vec{u} + \nabla\vec{u}^T]. \qquad \text{(A.3)}$$

In the plane of measurement, the shear stress

$$\sigma_{xy} = \frac{1}{2}\mu\left[\frac{\partial u}{\partial y} + \frac{\partial v}{\partial x}\right] \qquad \text{(A.4)}$$

and vorticity

$$\omega_z = \frac{1}{2}\mu\left[\frac{\partial v}{\partial x} - \frac{\partial u}{\partial y}\right] \qquad \text{(A.5)}$$

can be calculated using the previously derived expressions for the strain rates. The total stress field, as described in Appendix B, can be expressed as

$$\tau_1 = \frac{1}{2}\mu\left(\frac{\partial u}{\partial x} + \frac{\partial v}{\partial y}\right) + \frac{1}{2}\mu\left[\left(\frac{\partial u}{\partial x} - \frac{\partial v}{\partial y}\right)^2 + \left(\frac{\partial u}{\partial y} + \frac{\partial v}{\partial x}\right)^2\right]^{0.5}. \qquad \text{(A.6)}$$

C. Calculation of the wall shear stresses

The wall shear stress is defined as

$$WSS = 2\mu(\sigma.\vec{n}).\vec{t}, \tag{A.7}$$

$\vec{n}$ and $\vec{t}$ being respectively the normal and tangential unit vectors. In Cartesian two-dimensional coordinates, the WSS takes the form

$$WSS = 2\mu[\sigma_{xy}(n_x^2 - n_y^2) + (\sigma_{yy} - \sigma_{xx})n_x n_y]. \tag{A.8}$$

In order to calculate the wall shear stresses, one needs to estimate the local normal unit vector $\vec{n}$. In the case of the healthy abdominal aorta, modeled in this study as a straight tube, it is equal to $\vec{n} = (1,0)$. Inside the abdominal aortic aneurysm, the shape of the aneurysm was approximated by a cosine function

$$a(y) = a_0 + \frac{1}{2}\left(\frac{D}{2} - a_0\right)\left[1 + \cos\left(\frac{2\pi(y - L/2)}{L}\right)\right]. \tag{A.9}$$

The unit normal vector therefore reads

$$n_x = \pm\frac{1}{\sqrt{1 + (da/dy)^2}}, \tag{A.10a}$$

$$n_y = \mp\frac{da/dy}{\sqrt{1 + (da/dy)^2}}. \tag{A.10b}$$

Appendix B

Calculation of the total stress

The total stress, as referred to in this paper, is defined as the maximum eigenvalue of the stress tensor (A.3), which admits the following eigenvalues

$$\tau_1 = \frac{1}{2}\mu\left(\frac{\partial u_r}{\partial r} + \frac{\partial u_z}{\partial z}\right) + \frac{1}{2}\mu\left[\left(\frac{\partial u_r}{\partial r} - \frac{\partial u_z}{\partial z}\right)^2 + \left(\frac{\partial u_r}{\partial z} + \frac{\partial u_z}{\partial r}\right)^2\right]^{0.5}, \tag{B.1a}$$

$$\tau_2 = \frac{1}{2}\mu\left(\frac{\partial u_r}{\partial r} + \frac{\partial u_z}{\partial z}\right) - \frac{1}{2}\mu\left[\left(\frac{\partial u_r}{\partial r} - \frac{\partial u_z}{\partial z}\right)^2 + \left(\frac{\partial u_r}{\partial z} + \frac{\partial u_z}{\partial r}\right)^2\right]^{0.5}, \tag{B.1b}$$

$$\tau_3 = \mu\frac{u_r}{r}, \tag{B.1c}$$

when expressed in the (r, θ, z) coordinate system. The total stress is set equal to τ_1. Upon changing the variables from a cylindrical to a Cartesian coordinate system, the stress in the symmetry plane of the aneurysm model can be expressed by equation (A.6). This measurement of the stresses has the advantage upon the shear stresses to be invariant with respect to an arbitrary rotation of the coordinate axes.

Appendix C

Manufacture of silicone models of anatomically correct abdominal aortic aneurysms

The flow characteristics inside an anatomically correct AAA are shown at the end of the results in chapter 4. The model is reconstructed from a set of high-resolution images obtained with a GE helical CT scanner (Figure C.1). A three-dimensional reconstruction of the geometry of the lumen is first generated from the CT scan images using a volume rendering technique (Figure C.2 (*a*)). A model of the in vivo aneurysm is then manufactured through rapid-prototyping (Figure C.2 (*b*)). The mold, made out of plaster of Paris, is an exact replica of the whole arterial trunk spanning from 10 cm upstream of the renal arteries to 5 cm downstream of the iliac bifurcation. An elastic model, made of optically clear silicone, is created using a lost wax technique (Figure C.2 (*c*)). The mold is first coated with a very thin layer of wax in order to make the mold impermeable and then with silicone. The thickness of the silicone layer is kept as uniform as possible. The dissolution of the mold leaves an anatomically correct model of the whole arterial system that includes all the major arterial bifurcations (bifurcations to the renal, mesenteric and iliac arteries).

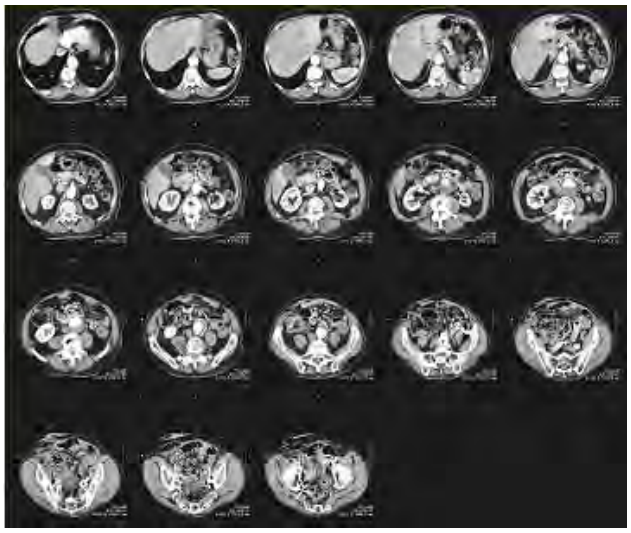

Figure C.1: CT scan images of the abdominal trunk of a patient with an AAA.

(*a*)  (*b*)  (*c*) 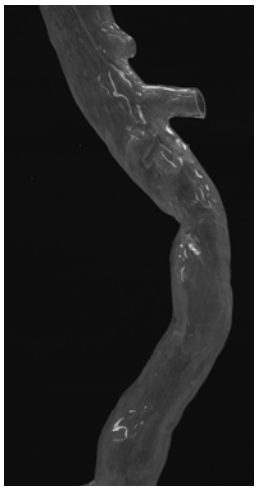

Figure C.2: (*a*) Three-dimensional reconstruction of an AAA from CT scan images, (*b*) mold generated in plaster of Paris with a rapid prototyping technique, (*c*) silicone model built from the mold using a lost wax technique.

REFERENCES

The UK Small Aneurysm Trial Participants. “Smoking, lung function and the prognosis of abdominal aortic aneurysm.” *Eur. J. Vasc. Endovasc. Surg.* **19**, 636–642 (2000).

Adolph R., Vorp D. A., Steed D. L., Webster M. W., Kameneva M. V. & Watkins S. C. “Cellular content and permeability of intraluminal thrombus in abdominal aortic aneurysm.” *J. Vasc. Surg.* **25**, 916–926 (1997).

Alveriadou B. R., Moake J. L., Turner N. A., Ruggeri Z. M., Folie B. J., Phillips M. D., Schreiber A. B., Hrinda M. E. & McIntire L. V. Real-time analysis of shear dependent thombus formation and its blockade by inhibitors of Van Willebrand factors binding to platelets. *Blood*. **81**, 1263-1276 (1993).

Andrews R. K., Shen Y., Gardiner E. E. & Berndt M. C. “Platelet adhesion receptors and (patho)physiological thrombus formation.” *Histol. Histopathol.* **16**, 969–980 (2001).

Armon M. P., Wenham P. W., Whitaker S. C., Gregson R. H. S. & Hopkinson B. R. “Common iliac artery aneurysms in patients with abdominal aortic aneurysms.” *Eur. J. Vasc. Endovasc. Surg.* **15**, 255–257 (1998).

Asbury C. L., Ruberti J. W., Bluth E. I. & Peattie R. A. “Experimental investigation of steady flow in rigid models of abdominal aortic aneurysms.” *Ann. Biomed. Eng.* **23**, 23–39 (1995).

Auerbach O. & Garfinkel L. “Atherosclerosis and aneurysm of the aorta in relation to smoking habits and age.” *Chest*. **78**, 805–809 (1980).

Bao X., Lu C. & Frangos J. a. “Temporal gradient in shear but not steady shear stress induces PDGF-A and MCP-1 expression in endothelial cells; Role of NO, NFκB and *egr*-1.” *Arteriosclr. Thromb. Vasc. Biol.* **19**, 996–1003 (1999)

Basnyat P. S., Biffin A. H. B., Moseley L. G., Hedges A. R. & Lewis M. E. “Mortality from ruptured abdominal aortic aneurysm in Wales.” *Br. J. Surg.* **86**, 765–770 (1999).

Bassiouny H. S., Song R. H., Kocharyan H., Kins E. & Glagov S. “Low flow enhances platelet activation after acute experimental arterial injury.” *J. Vasc. Surg.* **27**, 910–918 (1998).

Baumgartner H. R., Tschopp T. B. & Meyer D. “Shear rate dependent inhibition of platelet adhesion and aggregation on collagenous surfaces by antibodies to human facto VIII/von Willebrand factor.” *Br. J. Haematol.* **44**, 127–139 (1980).

Baumgartner H. R., Turitto V. & Weiss H. J. “Effects of shear rate on platelet interaction with subendothelium in citrated and native blood. II. Relationships among platelet adhesion, thrombus dimensions, and fibrin formation.” *J. Lab. Clin. Med.* **95**, 208–221 (1980).

Ben Driss A., Benessiano J., Poitevin P., Levy B. I. & Michel J. B. “Arterial expansive remodeling induced by high flow rates.” *Am. J. Physiol.* **272**, H851–H858 (1997).

Bengtsson H., Sonesson B. & Bergqvist D. “Incidence and prevalence of abdominal aortic aneurysms, estimated by necropsy studies and population screening by ultrasound.” In *The abdominal aortic aneurysm: genetics, pathophysiology, and molecular biology* (ed. Tilson M. D. & Boyd C. D.) New York, N. Y. New York Academy of Sciences (1996).

Best A., Price J. F. & Fowkes F. G. R., “Persistent increase in the incidence of abdominal aortic aneurysm in Scotland, 1981-2000.” *Brit. J. Surg*. **90**, 1510–1515 (2003).

Blackman B. R., Thibault L. E. & Barbee K. A. “Selective modulation of endothelial cell $[Ca^{2+}]_i$ response to flow by the onset rate of shear stress.” *J. Biomech. Eng.* **122**, 274–282 (2000).

Blackman B. R., García-Cardeña G. & Gimbrone M. A. Jr. “A new in vitro model to evaluate differential responses of endothelial cells to simulated arterial shear stress waveforms.” *J. Biomech. Eng.* **124**, 397–407 (2002).

Bluestein D., Niu L., Schoephoerster R. T. & Dewanjee M. K. “Steady flow in an aneurysm model: correlation between fluid dynamics and blood platelet deposition.” *J. Biomech. Eng.* **118**, 280–286 (1996).

Bluestein D., Rambod E. & Gharib M. “Vortex shedding as a mechanism for free emboli formation in mechanical heart valves.” *J. Biomech. Eng.* **122**, 125-134 (2000).

Bluestein D., Yin W., Affeld K. & Jesty J. “Flow-induced platelet activation in mechanical heart valves.” *J. Heart Valve Dis.* **13**, 501–508 (2004).

Bonamigo T. P. & Siqueira I. “Screening for abdominal aortic aneurysms.” *Rev. Hosp. Clin. Fac. Med. Sao Paulo.* **58**, 63–68 (2003).

Budwig R., Elger D., Hooper H. & Slippy J. “Steady flow in abdominal aortic aneurysm models.” *J. Biomech. Eng.* **115**, 418–423 (1993).

Busuttil R. W., Abou-Zamzam A. M. & Machkeder H. L. “Collagenase activity of the human aorta: comparison of patients with and without abdominal aortic aneurysms.” *Arch. Surg.* **115**, 1373–1378 (1980).

Busuttil R. W., Rinderbriecht J., Flesher A. & Carmack C. “Elastase activity: the role of elastase in aneurysm formation.” *Surg. Res.* **32**, 214–217 (1982).

Carmo M., Columbo L., Bruno A., Corsi F. R., Roncoroni L., Cuttin M. S., Radice F., Mussini E. & Settembrini P. G. “Alteration of elastin, collagen and their cross-links in abdominal aortic aneurysms.” *Eur. J. Vasc. Endovasc. Surg.* **23**, 543–549 (2002).

Caro C. G. *et al. The Mechanics of the Circulation*. Oxford, Oxford University Press (1978).

Caro C. G., Fitz-Gerald J. M. & Schroter R. C. “Atheroma and arterial wall shear: observation, correlation and proposal of a shear dependent mass transfer mechanism for atherogenesis.” *Proc. R Soc. Lond. B Biol. Sci.* **177**, 109-159 (1971).

Chappell D. C., Varner S. E., Nerem R. M., Medford R. M. & Alexander R. W. “Oscillatory shear stress stimulates adhesion molecule expression in cultured human endothelium.” *Circ. Res.* **82**, 532–539 (1998).

Chaudhuri A., Ansdell L. E., Grass A. J. & Adiseshiah M. “Aneurysmal hypertension and its relationship to sac thrombus: a semi-qualitative analysis by experimental fluid mechanics.” *Eur. J. Vasc. Endovasc. Surg.* **27**, 305–310 (2004).

Cheng C. P., Parker D. & Taylor C. A. “Quantification of wall shear stress in large blood vessels using Lagrangian interpolation functions with cine phase-contrast magnetic resonance imaging.” *Ann. Biomed. Eng.* **30**, 1020–1032 (2002).

Chiu J. J., Chen L. J., Chen C. N., Lee P. L. & Lee C. I. “A model for studying the effect of shear stress on interactions between vascular endothelial cells and smooth muscle cells.” *J. Biomech.* **37**, 531–539 (2004).

Chiu J. J., Chen L. J., Lee P. L., Lee C. I., Lo L.W., Usami S. & Chien S. “Shear stress inhibits adhesion molecule expression in vascular endothelial cells induced by coculture with smooth muscle cells.” *Blood.* **101**, 2667–2674 (2003).

Chow T. W., Hellums J. D., Moake J. L. & Kroll M. H. “Shear stress-induced von Willebrand factor binding to platelet glycoprotein Ib initiates calcium influx associated with aggregation.” *Blood*. **1**, 113–120 (1992).

Collin, J. & Radcliffe, J., “The epidemiology of abdominal aortic aneuysms.” *Br. J. Hosp. Med.* **7**, 64–67 (1988).

Cucina A., Sterpetti A. V., di Carlo A., Randone B., Aromatario C., Proietti P., Giustiniani Q., Cavallaro A. & Santoro-D'Angelo L. "Hemodynamic forces modulate simultaneously the release of growth factors and the organization of cytoskeleton of aortic smooth muscle cells." *Minerva Cardioangiol.* **44**, 637–643 (1996).

Darling R. C. "Ruptured arteriosclerotic abdominal aortic aneurysms." *Am. J. Surg.* **119**, 397–401 (1970).

David T., Thomas S. & Walker P. G. "Platelet deposition in stagnation point flow: an analytical and computational simulation." *Med. Eng. Phys.* **23**, 299-312 (2001).

Davies P. F., Dewey C. F., Bussolari S., Gordon E. & Gibrone M. A. "Influence of hemodynamic forces on vascular endothelial function." *J. Clin. Invest.* **73**, 1121–1129 (1984).

Davies P. F., Mundel T. & Barbee K. A. "A mechanism for heterogeneous endothelial responses to flow *in vivo* and *in vitro*." *J. Biomech.* **28**, 1553–1560 (1995).

Davies P. F., Remuzzi A., Gordon E. J., Dewey C. F. Jr & Gibrone M. A. Jr. "Turbulent fluid shear stress induces vascular endothelial turnover in vitro." *Proc. Natl. Acad. Sci. USA.* **83**, 2114–2117 (1986).

DePaola N., Gimbrone M., Davies P. & Dewey C. "Vascular endothelium responds to fluid shear stress gradients." *Arterioscl. Thromb.* **12**, 1254–1257 (1992).

Dewey C., Bussolari S., Gimbrone M. & Davies P. "The dynamic response of vascular endothelial cells to fluid shear stress." *J. Biomech. Eng.* **103**, 177–185 (1981).

Di Martino E., Mantero S., Inzoli F., Melissano G., Astore D., Chiesa R. & Fumero R. "Biomechanics of abdominal aortic aneurysm in the presence of endoluminal thrombus: experimental characterization and structure static computational analysis." *Eur. J. Vasc. Endovasc. Surg.* **15**, 290–299 (1998).

Di Martino E. S., Guadagni G., Fumero A., Ballerini G., Spirito R., Biglioli P. & Redaelli A. "Fluid-structure interaction within realistic three-dimensional models of the aneurysmatic aorta as a guidance to assess the risk of rupture of the aneurysm." *Med. Eng. Phys.* **23**, 647–655 (2001)

Dintenfass L. "Rheological approach to thrombosis and atherosclerosis." *Angiology.* **15**, 333–343 (1964).

Dobrin P. B. "Pathophysiology and pathogenesis of aortic aneurysms." In *Abdominal aortic aneurysms* (ed. Pierce G. E.) Philadelphia: Saunders, 687–703 (1989).

Egelhoff C. J., Budwig R. S., Elger D. F., Khraishi T. A. & Johansen K. H. “Model studies of the flow in abdominal aortic aneurysms during resting and exercise conditions.” *J. Biomech.* **32**, 1319–1329 (1999).

Einav S. & Bluestein D. “Dynamics of blood flow and platelet transport in pathological vessels.” *Ann. N. Y. Acad. Sci.* **1015**, 351-366 (2004).

Emerson M., Momi S., Paul W., Alberti P. F., Page C. & Gresele P. “Endogenous nitric oxide acts as a natural antithrombotic agent in vivo by inhibiting platelet aggregation in the pulmonary vasculature.” *Thromb. Haemost.* **81**, 961-966 (1999).

Englund R., Hudson P., Hanel K. & Stanton A. “Expansion rates of small abdominal aortic aneurysms.” *Aust. N. Z. J. Surg.* **123**, 474–484 (1998).

Eriksson E. E., Zerr J., Guo Y., Thoren P. & Lindbom L. “Direct observations in vivo on the role of endothelial selectins and α_4 integrin in cytokine-induced leukocyte-endothelium interactions in the mouse aorta.” *Circ. Res.* **86**, 526-533 (2000).

Finol E. A. & Amon C. H. “Blood flow in abdominal aortic aneurysms: pulsatile flow hemodynamics.” J. Biom. Eng. 123, 474–484 (2001).

Finol[1] E. A. & Amon C. H. “Flow-induced Wall Shear Stress in Abdominal Aortic Aneurysms: Part I – Steady Flow Hemodynamics.” *Comput. Methods Biomech. Biomed. Engin.* **5**, 309–318 (2002).

Finol[2] E. A. & Amon C. H. “Flow-induced Wall Shear Stress in Abdominal Aortic Aneurysms: Part II - Pulsatile Flow Hemodynamics.” *Comput. Methods Biomech. Biomed. Engin.* **5**, 319–328 (2002).

Finol E. A. & Amon C. H. “Flow dynamics in abdominal aortic aneurysms.” *Acta Cient. Venez.* **54**, 43–49 (2003).

Fisher A. B., Chien S., Barakat A. I. & Nerem R. M., “Endothelial cellular response to altered shear stress.” *Am. J. Physiol. Lung Cell Mol. Physiol.* **281**, L529-L533 (2001).

Folie B. J. & McIntire L. V. “Mathematical analysis of mural thrombogenesis. Concentration profiles of platelet-activating agents and effects of viscous shear flow.” *Biophys. J.* **56**, 1121–1141 (1989).

Fontaine V., Jacob M.-P., Rossignol P., Plissonnier D., Angles-Cano E. & Michel J.-B. “Involvement of the mural thrombus as a site of protease release and activation in human aortic aneurysms.” *Am. J. Pathol.* **161**, 1701–1710 (2002).

Forlow S. B., McEver R. P. & Nollert M. U. “Leukocyte-leukocyte interactions mediated by platelet microparticles under flow.” *Blood*. **95**, 1317-1323 (2000).

Fox J. A. & Hugh A. E. “Localization of atheroma: a theory based on boundary layer separation.” *Br. Heart J.* **26**, 388–399 (1966).

Fukuda S., Yasu T., Predescu D. N. & Schmid-Schoenbein G. W. “Mechanisms for regulation of fluid shear stress response in circulating leukocytes.” *Circ. Res.* **86**, e13-e18, 2000.

Fukushima T., Matsuzawa T. & Homma T. “Visualization and finite element analysis of pulsatile flow in models of the abdominal aortic aneurysm.” *Biorheology* **26**, 109–130 (1989).

Gacko M. & Głowiński S. “Activities of proteases in parietal thrombus of aortic aneurysm.” *Clin. Chim. Acta.* **271**, 171–177 (1998).

García-Cardeña[1] G., Comander J. I., Anderson K. R., Blackman B. R. & Gimbrone M. A. Jr. “Biomechanical activation of vascular endothelium as a determinant of its functional phenotype.” *Proc. Natl. Acad. Sci. USA.* **10**, 4478–4485 (2001).

García-Cardeña[2] G., Comander J. I., Blackman B. R., Anderson K. R. & Gimbrone M. A. “Mechanosensitive endothelial gene expression profiles: scripts for the role of hemodynamics in atherogenesis?” *Ann. N. Y. Acad. Sci.* **947**, 1–6 (2001).

Gharib M., Rambod E. & Shariff K. “A universal time scale for vortex ring formation.” *J. Fluid Mech.* **360**, 121–140 (1998).

Ghorpade A. & Baxter B. T. “Biochemistry and molecular regulation of matrix macromolecules in abdominal aortic aneurysms.” In *The abdominal aortic aneurysm: genetics, pathophysiology, and molecular biology* (ed. Tilson M. D. & Boyd C. D.) New York, N. Y. New York Academy of Sciences (1996).

Glagov S., Zarins C. K., Giddens D. G. & Ku D. N. “Hemodynamics and atherosclerosis, insights and perspectives gained from studies of human arteries.” *Arch. Pathol. Lab. Med.* **112**, 1018–1031 (1988).

Goldsmith H. L. “Blood flow and thrombosis.” *Thromb. Diath Haemorrh.* **32**, 35–48 (1974).

Gosgnach W., Messika-Zeitoun D., Gonzalez W., Philipe M. & Michel J.-B. “Shear stress induces iNOS expression in cultured smooth muscle cells: role of oxidative stress.” *Am. J. Physiol. Cell Physiol.* **279**, C1880-C1888 (2000).

Grabowski E. F. “Thrombolysis, flow, and vessel wall interactions.” *J. Vasc. Interv. Radiol.* **6**, 25S-29S (1995).

Green R. M. “Patient selection for endovascular AAA repair.” *Endovascular Today*. **6**, 31-33 (2002).

Greenwald S. E., Carter A. C. & Berry C. L. “Effect of age on the in vitro reflection coefficient of the aortoiliac bifurcation in humans.” *Circulation.* **82**, 114–123 (1990).

Hardy-Stashin J., Meyer W. W. & Kauffman S. L. “Branching coefficient (“area ratio”) of the human aortic bifurcation determined in distended specimens.” *Atherosclerosis*. **37**, 399–402 (1980).

Harter L. P., Gross B. H., Callen P. W. & Barth R. A. “Ultrasonic evaluation of abdominal aortic thrombus.” *J. Ultrasound Med.* **1**, 315–318 (1982).

Hatakeyama T., Shigematsu H. & Muto T. “Risk factors for rupture of abdominal aortic aneurysm based on three-dimensional study.” *J. Vasc. Surg.* **33**, 453–461 (2001).

He C. M. & Roach M. R. “The composition and mechanical properties of abdominal aortic aneurysms.” *J. Vasc. Surg.* **20**, 6–13 (1994).

Heldin C. H. & Westermark B. “Mechanism of action and in vivo role of platelet-derived growth factor,” *Physiol. Rev.* **79**, 1283–1316 (1999).

Hellums J. D. & Hardwick R. A. “Response of platelets to shear stress – a review.” *The Rheology of blood, blood vessels and associated tissues* (ed. Hwang N. H. C. & Gross D. R.) Sijthoff and Noorhoff, Amsterdam. 160–183 (1981).

Helmlinger G., Geiger R. V., Schreck S. & Nerem R. M. “Effects of pulsatile flow on cultured vascular endothelial cell morphology.” *J. Biomech. Eng.* **113**, 123–131 (1991).

Helmlinger G., Berk B. C. & Nerem R. M. “Calcium responses of endothelial cell monolayers subjected to pulsatile and steady laminar flow differ.” *Am. J. Physiol.* **269**, C367–C375 (1995).

Helps E. P. & McDonald D. A. “Arterial blood flow calculated from pressure gradients.” *J. Physiol.* **124**, 30–1P (1954).

Hernandez M. R., Bozzo J., Tonda R., Galan A. M., Ordinas A. & Escolar G. “Effect of anticoagulants on activation of polymorphonuclear leukocytes induced by shear stress.” *Int. J. Immunopathol. Pharmacol.* **14**, 139 (2001).

Holenstein R. & Ku D. N. “Reverse flow in the major infrarenal vessels – a capacitive phenomenon.” *Biorheology*. **25**, 835–842 (1988).

Hsiai T. K., Cho S. K., Honda H. M., Hama S., Navab M., Demer L. L. & Ho C.-M. “Endothelial cell dynamics under pulsating flows: significance of high versus low shear stress slew rates ($\partial\tau/\partial t$).” *Ann. Biomed. Eng.* **30**, 646–656 (2002).

Huang P. Y. & Hellums J. D. “Aggregation and disaggregation kinetics of human blood platelets: Part I, II and III.” *Biophys. J.* **65**, 334–343 (1993).

Hughes M. L. & Fontenelle L. J. “A 5-year review of abdominal aortic aneurysms at a VA medical center.” *Curr. Surg.* **57**, 343–345 (2000).

Ikeda Y., Handa M., Kawano K., Kamata T., Murata M., Araki Y., Anbo H., Kawai Y., Watanabe K., Itagaki I., Sakai K. & Ruggeri Z. M. “The role of von Willebrand factor and fibrinogen in platelet aggregation under varying shear stress.” *J. Clin. Invest.* **87**, 1234–1240 (1991).

Ikeda Y., Handa M., Kamata T., Kawano K., Kawai Y., Watanabe K., Kawakami K., Sakai K., Fukuyama M., Itagaki I., Yoshioka A. & Ruggeri Z. M. “Transmembrane calcium influx associated with von Willebrand factor binding to GP Ib in the initiation of shear-induced platelet aggregation.” *Thromb. Haemost.* 69, 496–502 (1993).

Ingoldby C. J. H., Wujanto R. & Mitchell J. E. “Impact of vascular surgery on community mortality from ruptured aortic aneurysms.” *Br. J. Surg.* **73**, 551–553 (1986).

Inzoli F., Boschetti F., Zappa M., Longo T. & Fumero R. “Biomechanical factors in abdominal aortic aneurysm rupture.” *Eur. J. Vasc. Surg*. **7**, 667–674 (1993).

Izzo J. L. & Shykoff B. E. “Arterial stiffness: clinical relevance, measurement and treatment.” *Rev. Cardiovasc. Med.* **2**, 29–40 (2001).

Jesty J., Yin W., Perrotta P. & Bluestein D. “Platelet activation in a circulating flow loop: combined effects of shear stress and exposure time.” *Platelets.* **14**, 143-149 (2003).

Johansen K., “Aneurysm.” *Sci. Am.* **247**, 110–125 (1982).

Johnston K. W., Rutherford R. B., Tilson M. D. Shah D. M. Hollier L., Stanley J. C. “Suggested standards for reporting on arterial aneurysms. Subcommittee on reporting standards for arterial aneurysms, ad hoc committee on reporting standards, Society for Vascular Surgery and North American Chapter, International Society for Cardiovascular Surgery.” *J. Vasc. Surg.* **13**, 452–458 (1991).

Kamiya A. & Togawa T. “Adaptative regulation of wall shear stress to flow change in the canine carotid artery.” *Am. J. Physiol.* **239**, H14–21 (1980).

Karino T. & Goldsmith H. L. “Role of blood cell-wall interactions in thrombogenesis and atherogenesis: a microrheological study.” *Biorheology*. **21**, 587-601 (1984).

Kazi M., Thyberg J., Religa P., Roy J., Eriksson P., Hedin U. & Swedenborg J. “Influence of intraluminal thrombus on structural and cellular composition of abdominal aortic aneurysm wall.” *J. Vasc. Surg.* **38**, 1283–1292 (2003).

Kraiss L. W., Geary R. L., Mattsson E. J., Vergel S., Au A. Y., Clowes A. W. “Acute reductions in blood flow and shear stress induce platelet-derived growth factor-A expression in baboon prosthetic grafts.” *Circ. Res.* **79**, 45–53 (1996).

Kroll M. H., Hellums J. D., McIntire L. V., Schafer A. L. & Moake J. L. “Platelets and shear stress.” *Blood* **88**, 1525–1541 (1996).

Ku D. N. & Zhu C. “The mechanical environment of the artery.” In *Hemodynamic forces and vascular cell biology* (ed. Sumpio B.) Austin, Landes Co. (1997).

Ku D. N., Giddens D. P., Zarins C. K. & Glagov S. “Pulsatile flow and atherosclerosis in the human carotid bifurcation. Positive correlation between plaque location and low oscillating shear stress.” *Arteriosclerosis*. **5**, 293–302 (1985).

Kunov M. J., Steinman D. A. & Ethier C. R. “Particle volumetric residence time calculations in arterial geometries.” *J. Biomech. Eng.* **118**, 158-164 (1996).

Law M. R., Morris J. & Wald N. J. “Screening for abdominal aortic aneurysms.” *J. Med. Screen.* **1**, 110–116 (1994).

Lawrence M. B., Kansas G. S., Kundel E. J. & Ley K. “Threshold levels of fluid shear promote leukocyte adhesion through selectins (CD62L,P,E).” *J. Cell Biol.* **136**, 717-727 (1997).

Lee A. A., Graham D. A., Dela Cruz S., Ratcliffe A., Karlon W. J. “Fluid shear stress-induced alignment of cultured vascular smooth muscle cells.” *J. Biomech. Eng.* **124**, 37–43 (2002).

Lee A. J., Flowkes F. G., Carson M. N., Leng G. C. & Allan P. L. “Smoking, atherosclerosis and risk of abdominal aortic aneurysm.” *Eur. Heart. J.* **18**, 545–546 (1997).

Lee D., Chiu Y. L. & Jen C. Y. “Wall stresses and platelet adhesion in a T-junction.” *Proc. Natl. Sci. Counc. ROC(A).* **23**, 303–310 (1999).

Lee R. T., Yamamoto C., Feng Y., Potter-Perigo S., Briggs W. H., Landschulz K. T., Turi T. G., Thompson J. F., Libby P. & Wight T. N. “Mechanical strain induces specific changes in the synthesis and organization of proteoglycans by vascular smooth muscle cells.” *J. Biol. Chem.* **276**, 13847–13851 (2001).

Lei M., Kleinsteuer C. & Truskey G. A. “Numerical investigation and prediction of atherogenic sites in branching arteries.” *J. Biomech. Eng.* **117**, 350–357 (1995).

Levesque M. J. & Nerem R. M., "The elongation and orientation of cultured endothelial cells in response to shear stress." *J. Biomech. Eng.* **107**, 341–347 (1985).

Liao S., Curci J. A., Kelley B. J., Sicard G. A. & Thompson R. W., "Accelerated replicative senescence of medial smooth muscle cells derived from abdominal aortic aneurysms compared to the adjacent inferior mesenteric artery." *J. Surg. Res.* **92**, 85–95 (2000).

Limas C., Westrum B. & Limas C. J. "The evolution of vascular changes in the spontaneously hypertensive rat." *Am. J. Pathol.* **98**, 357–384 (1980).

Long Q., Xu X. Y., Bourne M. & Griffith T. M. "Numerical study of blood flow in an anatomically realistic aorto-iliac bifurcation generated from MRI data." *Magn. Reson. Med.* **43**, 565-576 (2000),

Longest P. W. & Kleinsteuer C. "Numerical simulation of wall shear stress conditions and platelet localization in realistic end-to-side arterial anastomoses." *J. Biomech. Eng*. **125**, 671-681 (2003).

López-Candales A., Holmes D. R., Liao S., Scott M. J., Wickline S. A. & Thompson R. W. "Decreased vascular smooth muscle cell density in medial degeneration of human abdominal aortic aneurysms." *Am. J. Pathol.* **150**, 993–1007 (1997).

MacSweeney S. T., Young G., Greenhalgh R. M. & Powell J. T. "Mechanical properties of the aneurysmal aorta." *Br. J. Surg.* **79**, 1281–1284 (1992).

MacSweeney, S. T. R. "Abdominal aortic aneurysms." In *Pathophysiology of aneurysm disease – Report of a meeting of physicians and scientists*. London: University College London Medical School. Lancet. **341**, 215–220 (1993).

MacSweeney, S. T. R., Ellis M., Worrell P. C., Greenhalgh R. M. & Powell J. T. "Smoking and growth rate of small abdominal aortic aneurysms." *Lancet*. 344, 651–652 (1994).

Maier S. E., Meier D., Boesinger P., Moser U. T. & Vieli A. "Human abdominal aorta: comparative measurements of blood flow with MR imaging and multigated Doppler US." *Radiology* **171**, 487–492 (1989)

Mailhac A., Badimon J. J., Fallon J. T., Fernandez-Ortiz A., Meyer B., Chesebro J. H., Fuster V. & Badimon L. "Effect of an eccentric severe stenosis on fibrin(ogen) deposition on severely damaged vessel wall in arterial thrombosis. Relative contribution of fibrin(ogen) and platelets." *Circulation.* **90**, 988-996 (1994).

Malek M., Alper S. L. & Izumo S. "Hemodynamic shear stress and its role in atherosclerosis." *JAMA.* 282, 2035–2042 (1999).

Marschel P. & Schmid-Schoenbein G. W. “Control of fluid shear response in circulating leukocytes by integrins.” *Ann. Biomed. Eng.* **30**, 333-343 (2002).

Matsushita M., Nishikimi N., Sakurai T., Nimura Y. “Relationship between aortic calcification and atherosclerotic disease in patients with abdominal aortic aneurysm.” *Int. Angiol.* **19**, 276–279 (2000).

McDonald D. A. *Blood flow in arteries*. Baltimore, Williams & Wilkens (1974).

Mills C. J., Gabe I. T., Gault J. H., Mason D. T., Ross J., Braunwald E. & Shillingford J. P. “Pressure-flow relationships and vascular impedance in man.” *Cardiovasc. Res.* **4**, 405-417 (1970)

Moake J. L., Turner N. A., Stathopoulos N. A., Nolasco L. H. & Hellums J. D. “Involvement of large plasma von Willebrand factor (vWF) multimers and unusually large vWF forms derived from endothelial cells in shear stress-induced platelet aggregation.” *J. Clin. Invest.* **78**, 1456–1461 (1986).

Moazzam F., DeLano F. A., Zweifach B. W. & Schmid-Schoenbein G. W. “The leukocyte response to fluid stress.” *Proc. Natl. Acad. Sci. USA.* **94**, 5338-5343 (1997).

Moore J. E., Ku K. D., Zarins C. K. & Glagov S. “Pulsatile flow visualization in the abdominal aorta under differing physiologic conditions: implications for increased susceptibility to atherosclerosis.” *J. Biomech. Eng.* **114**, 391–397 (1992).

Moore J. E., Xu C., Glagov S., Zarins C. K. & Ku D. N. Fluid wall shear stress measurements in a model of the human abdominal aorta: oscillatory behavior and relationship to atherosclerosis. *Atherosclerosis.* **110**, 225-240 (1994).

Mower W. R., Quinones W. J. & Gambhir S. S. “Effect of intraluminal thrombus on abdominal aortic aneurysm wall stress.” *J. Vasc. Surg.* **26**, 602–608 (1997).

Mower W. R. & Quinones W. J. “Regarding “thrombus within an aortic aneurysm does not reduce the pressure on the aneurysm wall.”” *J. Vasc. Surg.* **33**, 660–661 (2001).

Nagel T., Resnick N., Dewey C. F. & Gimbrone M. A. “Vascular endothelial cells respond to spatial gradients in fluid shear stress by enhanced activation of transcription factors.” *Arterioscl. Thromb. Vasc. Biol.* **19**, 1825–1834 (1999).

Nichols W. W. *McDonald’s blood flow in arteries: theoretic, experimental and clinical principles* (ed. Nichols W.W. & O’Rourke M. F.) London, Arnold (1998).

Nomura S., Tandon N. N., Nakamura T., Cone J., Fukuhara S. & Kambayashi J. “High-shear-stress-induced activation of platelets and microparticles enhances

expression of cell adhesion molecules in THP-1 and endothelial cells." *Atherosclerosis*. **158**, 277-287 (2001).

Noorgard O., Rais O. & Angquist K. A. "Familial occurrence of abdominal aortic aneurysms." *Surgery*. **95**, 650–656 (1984).

Noris M., Morigi M., Donadelli R., Aiello S., Foppolo M., Todeschini M., Orisio S., Remuzzi G. & Remuzzi A. "Nitric oxide synthesis by cultured endothelial cells is modulated by flow conditions." *Circ. Res.* **76**, 536–543 (1995).

O'Brien J. R. "Shear-induced platelet aggregation." *Lancet.* **335**, 711–713 (1990).

Okuyama M. Ohta Y., Kambayashi J. & Monden M. "Fluid shear stress induces actin polymerization in human neutrophils." *J. Cell Biochem.* **63**, 434-441 (1996).

O'Rourke M., Arterial stiffness, systolic blood pressure and logical treatment of arterial hypertension." *Hypertension*. **15**, 339–347 (1990).

Oyre S., Pedersen E. M., Ringgaard S., Boesiger P. & Paaske W. P. "*In vivo* wall shear stress measured by magnetic resonance velocity mapping in the normal human abdominal aorta." *Eur. J. Vasc. Endovasc. Surg.* **13**, 263–271 (1997).

Paivansalo M. J., Merikanto J., Jerkkola T., Savolainen M. J., Rantala A. O., Kauma H., Lilja M., Reunanen Y. A., Kesaniemi A. & Suramo I. "Effect of hypertension and risk factors on diameters of abdominal aorta and coomon iliac and femoral arteries in middle-aged hypertensive and control subjects: a cross-sectional systematic study with duplex ultrasound." *Atherosclerosis.* 153, 99–106 (2000).

Papadaki[1] M., Ruef J., Nguyen K. T., Li F., Patterson C., Eskin S. G., McIntire L. V. & Runge M. S. "Differential regulation of protease activated receptor-1 and tissue plasminogen activator expression by shear stress in vascular smooth muscle cells." *Circ. Res.* **83**, 1027–1034 (1998).

Papadaki[2] M., Tilton R. G., Eskin S. G. & McIntire L. V. "Nitric oxide production by cultured human aortic smooth muscle cells: stimulation by fluid flow." *Am. J. Physiol.* **274**, H616–H626 (1998).

Peattie R. A., Schrader T., Bluth E. I. & Comstock C. E. "Development of turbulence in steady flow through models of abdominal aortic aneurysms." *J. Ultrasound Med.* **13**, 467–472 (1994).

Peattie R.A, Asbury C. L., Bluth E. I. & Ruberti J. W. "Steady flow in models of abdominal aortic aneurysms. Part I: Investigation of the velocity patterns." *J. Ultrasound Med.* **15**, 679-688 (1996).

Pedersen E. M., Agerbaek M., Kristensen I. B. & Yoganathan A. P. “Wall shear stress and early atherosclerotic lesions in the abdominal aorta in young adults.” *Eur. J. Vasc. Endovasc. Surg.* **13**, 443–451 (1997).

Pedersen E., Sung H., Burlson A. & Yoganathan A. “Two-dimensional velocity measurements in a pulsatile flow model of the normal abdominal aortic simulating different hemodynamic conditions.” *J. Biomech.* **26**, 1237-1247 (1993)

Pedersen E. M., Yoganathan A. P. & Lefebvre X. P. “Pulsatile flow visualization in a model of the human abdominal aorta and aortic bifurcation.” *J. Biomech.* **25**, 935–944 (1992).

Pedley T. J. *The Fluid Mechanics of Large Blood Vessels*. Cambridge, Cambridge University Press (1979).

Pokrovskii A. V., Dan V. N., Zlatovchen A. M. & Il’in S. A. “The impact of cardiac status and arterial hypertension on the results of surgical treatment of patients over 70 years with abdominal aortic aneurysms.” *Angiol. Sosud. Khir*. **9**, 71–76 (2003).

Prisant L. M. & Mondy J. S. “Images in hypertension: abdominal aortic aneurysms.” *J. Clin. Hypertens.* **6**, 85–89 (2004).

Purvis N. B. & Giorgio T. D. “The effects of elongational stress exposure on the activation and aggregation of blood platelets.” *Biorheology*. **28**, 355–367 (1991).

Raghavan M. L., Vorp D. A., Federle M. P., Makaroun M.S. & Webster M. W. “Wall stress distribution on three-dimensionally reconstructed models of human abdominal aortic aneurysm.” *J. Vasc. Surg.* **31**, 760–769 (2001).

Raghavan M. L. & Vorp D. A. “Toward a biomechanical tool to evaluate rupture potential of abdominal aortic aneurysm: identification of a finite strain constitutive model and evaluation of its applicability.” *J. Biomech.* **33**, 475–482 (2000).

Reilly J. M. & Tilson M. D., “Incidence and etiology of abdominal aortic aneurysms.” In *Abdominal aortic aneurysms* (ed. Pierce G. E.) Philadelphia: Saunders, 689–898 (1989).

Reininger A. J., Korndorfer M. A. & Wurzinger L. J. “Adhesion of ADP-activated platelets to intact endothelium under stagnation point flow in vitro is mediated by the integrin αIIbβ3. *Thromb. Haemost.* **79**, 998–1003 (1998).

Reininger A. J., Reininger C. B., Heinzmann U. & Wurzinger L. J. “Residence time in niches of stagnant flow determines fibrin clot formation in an arterial branching model – detailed flow analysis and experimental results.” *Thromb. Haemost.* **74**, 916-922 (1995).

Rhoads D. N., Eskin S. G. & McIntire L. V. “Fluid flow releases fibroblast growth factor-2 from human aortic smooth muscle cells.” *Arterioscler. Thromb. Vasc. Biol.* **20**, 416-421 (2000).

Richardson E. G. & Tyler W. “The transverse velocity gradient near the mouths of pipes in which an alternating or continuous flow of air is established.” *Proc. Phys. Soc. Lond.* **42**, 1–15 (1929).

Rosenson-Schloss R. S., Vitolo J. L. & Moghe P. V. “Flow-mediated cell stress induction in adherent leukocytes is accompanied by modulation of morphology and phagocytic function.” *Med. Biol. Eng. Comput.* **37**, 257-263 (1999).

Salo J. A., Soisalon-Soininen S., Bondestam S. & Mattila P. S. “Familial occurrence of abdominal aortic aneurysm.” *Ann. Intern. Med.* **130**, 637–642 (1999).

Samy, A. K., Whyte B. & MacBain, G., “Abdominal aortic aneurysm in Scotland.” *Br J. Surg.* **81**, 1104–1106 (1994).

Satta J., Laara E. & Juvonen T. Intraluminal thrombus predicts rupture of an abdominal aortic aneurysm. *J. Vasc. Surg.* **23**, 737-739 (1996).

Schowalter D. G., Van Atta C. W. & Lasheras J. C. “A study of streamwise vortex structure in a stratified shear layer.” *J. Fluid Mech.* **281**, 247–291 (1994).

Schrader T., Peattie R. A., Bluth E. I. & Comstock C. E. “A qualitative investigation of turbulence in flow through a model abdominal aortic aneurysm.” *Invest. Radiol*. **27**, 515–519 (1992).

Schurink G. W., van Baalen J. M., Visser M. J. & van Bockel J. H., “Thrombus within an aortic aneurysm does not reduce pressure on the aneurysmal wall.” *J. Vasc. Surg.* **31**, 501–506 (2000).

Shah P. M., Scarton H. A. & Tsapogas M. J. “Geometric anatomy of the aortic-common iliac bifurcation.” *J. Anat.* **126**, 451–458 (1978).

Shankaran H., Alexandridis P. & Neelamegham S. “Aspects of hydrodynamic shear regulating shear-induced platelet activation and self-association of von Willebrand factor in suspension.” *Blood.* **101**, 2637–2645 (2003).

Singh K., Bønaa K. H., Jacobson B. K., Bjørk L. & Solberg S. “Prevalence of and risk factors for abdominal aortic aneurysms in a population-based study.” *Am. J. Epidemiol.* **154**, 236–244 (2001).

Spagnoli L. G., Villaschi S., Neri L. & Palmieri G., “Gap junctions in myoendothelial bridges of rabbit carotid arteries.” *Experientia.* **38**, 124–125 (1982).

Stefanadis C., Tsiamis E., Vlachopoulos C., Stratos C., Toutouzas K., Pitsavos C., Marakas S., Boudoulas H. & Toutouzas P. “Unfavorable effects of smoking on the elastic properties of the human aorta.” *Circulation.* **95**, 31–384 (1997).

Stefanadis C., Vlachopoulos C., Tsiamis E., Diamantopoulos L., Toutouzas K., Giatrakos N., Vaina S., Tsekoura D. & Toutouzas P. “Unfavorable effects of passive smoking on aortic function in men.” *Ann. Intern. Med.* **128**, 426–434 (1998).

Sterpetti A. V., Feldhaus R. J., Schultz R. D. & Blair E. A. “Identification of abdominal aortic aneurysm patients with different clinical features and clinical outcomes.” *Am. J. Surg.* **156**, 466–469 (1988).

Sterpetti[1] A. V., Cucina A., D’Angelo L. S., Cardillo B. & Cavallaro A. “Response of arterial smooth muscle cells to laminar flow.” *J. Cardiovasc. Surg. (Torino).* **33**, 619–624 (1992).

Sterpetti[2] A. V., Cucina A., Napoli F. Shafer H., Cavallaro A. & D’Angelo L. S. “Growth factor release by smooth muscle cells is dependent on haemodynamic factors.” *Eur. J. Vasc. Surg.* **6**, 636–638 (1992).

Stringfellow M. M., Lawrence P. F. & Stringfellow R. G., “The influence of aorta-aneurysm geometry upon stress in the aneurysm wall.” *J. Surg. Res.* **42**, 425–433 (1987).

Stroud J. S., Berger S. A. & Saloner D. “Influence of stenosis morphology on flow through severely stenotic vessels: implications for plaque rupture.” *J. Biomech.* **33**, 443–455 (2000).

Sumner D. S., Hokanson D. E. & Strandness D. E., Jr. “Stress-strain characteristics and collagen-elastin content of abdominal aortic aneurysms.” *Surg. Gynecol. Obstet.* **130**, 459–466 (1970).

Sutera S. P., Nowak M. D., Joist J. H., Zeffren D. J. & Bauman J. E. “A programmable, computer-controlled cone-plate viscosimeter for the application of pulsatile shear stress to platelet suspensions.” *Biorheology*. **25**, 449–459 (1988).

Szilagyi D. E. “Clinical diagnosis of intact and ruptured abdominal aortic aneurysms.” In *Aneurysms, diagnosis and treatment* (ed. Bergan J. J. & Yao J. S.). New York: Grune & Stratton. 205–215 (1982).

Tardy Y., Resnick N., Nagel T., Gimbrone M. & Dewey C. “Shear stress gradients remodel endothelial monolayer in vitro via a cell proliferation-migration-loss cycle.” *Arterioscl. Thromb. Vasc. Biol.* **17**, 3102–3106 (1997).

Taylor C. A., Cheng C. P., Espinosa L. A., Tang B. T., Parker D. & Herfkens R. J. “*In vivo* quantification of blood flow and wall shear stress in the human

abdominal aorta during lower limb exercise." *Ann. Biomed. Eng.* **30**, 402–408 (2002).

Taylor L. M., Jr & Porter J. M. "Basic data related to clinical decision-making in abdominal aortic aneurysms." *Ann. Vasc. Surg.* **1**, 502–504 (1987).

Taylor T. W. & Yamaguchi T. "Three-dimensional simulation of blood flow in an abdominal aortic aneurysm – steady and unsteady flow cases." *J. Biomech. Eng.* **116**, 89–97 (1994).

Thompson R. W., Liao S. & Curci J. A. "Vascular smooth muscle cell apoptosis in abdominal aortic aneurysms." *Coron. Artery Dis.* **8**, 623- (1997).

Thubrikar M. J., al-Soudi J. & Robicsek F. "Wall stress studies of abdominal aortic aneurysm in a clinical model." *Ann. Vasc. Surg.* **15**, 355–366 (2001).

Thubrikar M. J., Labrosse M., Robicsek F., Al-Soudi J. & Fowler B., "Mechanical properties of abdominal aortic aneurysm wall." *J. Med. Eng. Technol.* **25**, 133–142 (2001).

Thubrikar M. J., Robicsek F., Labrosse M., Chervenkoff V. & Fowler B. L. "Effect of thrombus on abdominal aortic aneurysm wall dilation and stress." *J. Cardiovasc. Surg.* **44**, 67–77 (2003).

Topper J. N., Cai J., Falb D. & Gimbrone M. A. "Identification of vascular endothelial genes differentially responsive to fluid mechanical stimuli: cyclooxygenase-2 manganese superoxide dismutase, and endothelial cell nitric oxide synthase are selectively up-regulated by steady laminar shear stress." *Proc. Natl. Acad. Sci. USA.* **93**, 10417–10422, (1996).

Traub O. & Berk B. C. "Laminar shear stress: mechanisms by which endothelial cells transduce an atheroprotective force." *Arterioscler. Thromb. Vasc. Biol.* **18**, 677-685 (1998).

Treska V. & Certik B. "Small aneurysms of the abdominal aorta." *Rozhl. Chir.* **78**, 613–617 (1999).

Tsao R., Jones S. A., Giddens D. P., Zarins C. K. & Glagov S. "An automated three-dimensional particle tracking technique for the study of modeled arterial flow fields." *J. Biomech. Eng.* **117**, 211-218 (1995).

Tzima E., Del Pozo M. A., Kiosses W. B., Mohamed S. A., Li S., Chien S. & Schwarz M. A. "Activation of Rac1 by shear stress in endothelial cells mediates both cytoskeletal reorganization and effects on gene expression." *EMBO J.* **21**, 6791–6800 (2002).

Viswanath N., Rodkiewicz C. M. & Zajac S. “On the abdominal aortic aneurysms: pulsatile state considerations.” *Med. Eng. Phys.* **19**, 343–351 (1997).

Vorp D. A., Wang D. H. J., Webster M .W. & Federspiel W. J. “Effect of intraluminal thrombus thickness and bulge diameter on the oxygen diffusion in abdominal aortic aneurysm.” *J. Biomech. Eng.* **120**, 579–583 (1998).

Vorp D. A., Lee P. C., Wang D. H., Makaroun M. S., Nemoto E. M., Ogawa S. & Webster M. W. “Association of intraluminal thrombus in abdominal aortic aneurysm with local hypoxia and wall weakening.” *J. Vasc. Surg.* **34**, 291–299 (2001).

Walpola P. L., Gotlieb A. I. & Langille B. L. “Monocyte adhesion and changes in endothelial cell number, morphology and F-actin distribution elicited by low shear stress in vivo.” *Am. J. Pathol.* **142**, 1392–1400 (1993).

Wang D. H., Makaroun M. S., Webster M. W. & Vorp D. A. “Mechanical properties and microstructure of intraluminal thrombus from abdominal aortic aneurysms.” *J. Biomech. Eng.* **123**, 536–539 (2001).

Wang D. H., Makaroun M. S., Webster M. W. & Vorp D. A. “Effect of intraluminal thrombus on wall stress in patient-specific models of abdominal aortic aneurysms.” *J. Vasc. Surg.* **36**, 598–604 (2002).

Wang D. M. & Tarbell J. M. “Modeling interstitial flow in an artery wall allows estimation of wall shear stress on smooth muscle cells.” *J. Biomech Eng.* **117**, 358–363 (1995).

Warabi E., Wada Y., Kajiwara H., Kobayashi M., Koshiba N., Hisada T., Shibata M., Ando J., Tsuchiya M., Kodama T. & Noguchi N. “Effect on endothelial cell gene expression of shear stress, oxygen concentration, and low-density lipoprotein as studied by a novel flow cell culture system.” *Free Radic. Biol. Med.* **37**, 682–694 (2004).

Wilmink A. B. M., Quick C. R. G., Hubbard C. Sf. & Day N. E. “The association between connective tissue laxity and the risk of an abdominal aortic aneurysm.” *Eur. J. Vasc. Endovasc. Surg.* **20**, 290–295 (2000).

White J. V. & Mazzocco S. L. “Formation and growth of aortic aneurysms induced by adventitial elastolysis.” In *The abdominal aortic aneurysm: genetics, pathophysiology, and molecular biology* (ed. Tilson M. D. & Boyd C. D.) New York, N. Y. New York Academy of Sciences (1996).

Womersley J. R. “Flow in the larger arteries and its relation to the oscillating pressure.” *J. Physiol.* **124**, 31–2P (1954).

Wootton D. M., Markou C. P., Hanson S. R. & Ku D. N. “A mechanistic model of acute platelet accumulation in thrombogenic stenoses.” *Ann. Biomed. Eng.* **29**, 321-329 (2001).

Wurzinger L. J., Opitz R., Blasberg P. & Schmid-Schoenbein H. “Platelet and coagulation parameters following millisecond exposure to laminar shear stress.” *Thromb. Haemost.* **54**, 381–386 (1985).

Yin W., Alemu Y., Affeld K., Jesty J. & Bluestein D. “Flow-induced platelet activation in bileaflet and monoleaflet mechanical heart valves.” *Ann. Biomed. Eng.* **32**, 1058-1066 (2004).

Yip T. H. & Yu S. C. M. “Cyclic transition to turbulence in rigid abdominal aortic aneurysms models.” *Fluid Dyn. Res.* **29**, 81–113 (2001).

Yip T. H. & Yu S. C. M. “Oscillatory flows in straight tubes with an axisymmetric bulge.” *Exp. Thermal Fluid Sc.* **26**, 947–961 (2002).

Yoshida Y., Yamaguchi T., Caro C. G., Glagov S. & Nerem R. M. “Role of blood flow in atherogenesis.” *Proceedings of the International Symposium, Hyogo,* October 1987, Springer-Verlag (1987).

Yu S. C. M., Chan W. K., Ng B. T. H. & Chua L. P. “A numerical investigation on the steady and pulsatile flow characteristics in axi-symmetric abdominal aortic aneurysm models with some experimental evaluation.” *J. Med. Eng. Tech.* **23**, 228–239 (1999).

Yu S. C. M. “Steady and pulsatile flow characteristics in Abdominal Aortic Aneurysm models using Particle Image Velocimetry.” *Int. J. Heat Fluid Flow* **21**, 74–83 (2000).

Yu S. C. M. & Zhao J. B. “A particle image velocimetry study on the pulsatile flow characteristics in straight tubes with an asymmetric bulge.” *Proc. Inst. Mech. Eng. C.* **214**, 655–671 (2002).

Zarins C. K. & Glagov S. “Aneurysms and obstructive plaques: differing local responses to atherosclerosis.” In *Aneurysms, diagnosis and treatment* (ed. Bergan J. J. & Yao J. S.) New York: Grune & Stratton, 61–82 (1982).

Zarins C. K., Xu C. & Glagov S. “Atherosclerotic enlargement of the human abdominal aorta.” *Atherosclerosis.* **155**, 157–164 (2001).

Zarins C. K., Zatina M. A. Giddens D. P., Ku D. N. & Glagov S. “Shear stress regulation of artery lumen diameter in experimental atherogenesis.” *J. Vasc. Surg.* **5**, 413–420 (1987).

Zhang J. N., Bergeron A. L., Yu Q., Sun C., McIntire L. V., Lopez J. A. & Dong J. F. "Platelet aggregation and activation under complex patterns of shear stress." *Thromb. Haemost.* **88**, 817–821 (2002).

Zhang J. N., Bergeron A. L., Yu Q., Sun C., McBride L., Bray P. F. & Dong J. F. "Duration of exposure to high fluid shear stress is critical in shear-induced platelet activation-aggregation." *Thromb. Haemost.* **90**, 672–678 (2003).

Zhao Y., Chen B. P., Miao H., Yuan S., Li Y. S., Hu Y., Rocke D. M. & Chien S. "Improved significance test for DNA microarray data: temporal effects of shear stress on endothelial genes." *Physiol Genomics.* **12**, 1–11 (2002).